ADDITIVE MANUFACTURING OF VISCOUS MATERIALS: DEVELOPMENT AND CHARACTERIZATION OF 3D PRINTED ENERGETIC STRUCTURES

by

Monique S. McClain

A Dissertation

Submitted to the Faculty of Purdue University

In Partial Fulfillment of the Requirements for the degree of

Doctor of Philosophy

School of Aeronautics and Astronautics

West Lafayette, Indiana

August 2020

THE PURDUE UNIVERSITY GRADUATE SCHOOL

STATEMENT OF COMMITTEE APPROVAL

Dr. Steven F. Son, Chair

School of Mechanical Engineering

Dr. Jeffrey F. Rhoads

School of Mechanical Engineering

Dr. Timothée L. Pourpoint

School of Aeronautics and Astronautics

Dr. Stephen Beaudoin

Davidson School of Chemical Engineering

Approved by:

Dr. Gregory A. Blaisdell

I would like to dedicate this work to my grandparents, who have overcome miles of adversity, yet have proved to me that progress is possible. I would also like to thank the rest of my family and my friends along the way for supporting me so that I could grow into the person that I am today. Every step that I take comes from opportunity that was selflessly given to me by those who made hard sacrifices.

ACKNOWLEDGMENTS

I would like to acknowledge funding from NSTRF grant 80NSSC17K0176 for providing me the opportunity and the freedom to explore impactful, leading edge research. I would like to thank my advisor Dr. Steven Son and committee member Dr. Jeffrey Rhoads for their guidance on the work in this thesis. I thank committee members Dr. Timothée Pourpoint for guidance on additional research projects and Dr. Stephen Beaudoin for his time. In addition, I want to thank Dr. Rodney Trice for access to equipment that was helpful for completing the research in this dissertation. A special thanks goes to Dr. Emre Gunduz for developing the VAP technology that was critical to this research.

I would also like to thank my lab mates for their guidance and comradery, and my coffee maker for the extra motivation. In particular, Aaron Afriat helped to develop a modified hybrid VAP/FFF printer and created a parsing code to allow controlled activation of an incorporated UV-light. Trevor Fleck produced Al/PVDF filaments for high pressure reactive wire experiments, assisted with flexural strength tests of ceramic matrix composites, and improved the VAP system. Andrew Schlup assisted with use of the Flacktek mixer and operated the tube furnace for ceramic matrix composites research. Simon Ray was instrumental in making improvements to the VAP system, investigating dissimilar material adhesion for the purpose of VAP/FFF printing, and troubleshooting a version of Rocfire at Purdue. Tim Manship and Michael Baier often provided helpful suggestions on how to improve the propellant manufacturing process. Brandon Montano assisted with the testing and construction of layered AP propellants. Lastly, Daniel Inman assisted with viscosity measurements involving the Brookfield viscometer.

In addition, I would like to thank external researchers for their role in the presented research. Dr. Jonathan E. Jones and Phillip Franklin from NASA Marshall Space Flight Center provided the scope for the ceramic matrix composite research project as well as resources and guidance. I would like to thank Drs. Brian Bojko, Clare Dennis, and Ephraim Washburn at NAWCWD China Lake for their collaboration and for allowing me to expand my portfolio in energetics research by providing the resources to investigate computational combustion of layered propellant and the melt layer of ammonium perchlorate single crystals.

TABLE OF CONTENTS

LIST OF TABLES

LIST OF FIGURES

ABSTRACT

The performance of solid rocket motors (SRMs) is extremely dependent on propellant formulation, operating pressure, and initial grain geometry. Traditionally, propellant grains are cast into molds, but it is difficult to remove the grains without damage if the geometry is too complex. Cracks or voids in propellant can lead to erratic burning that can break the grain apart and/or potentially overpressurize the motor. Not only is this dangerous, but the payload could be destroyed or lost. Some geometries (i.e. internal voids or intricate structures) cannot be cast and there is no consistent nor economical way to functionally grade grains made of multiple propellant formulations at fines scales (~ mm) without the risk of delamination between layers or the use of adhesives, which significantly lower performance. If one could manufacture grains in such a way, then one would have more control and flexibility over the design and performance of a SRM. However, new manufacturing techniques are required to enable innovation of new propellant grains and new analysis techniques are necessary to understand the driving forces behind the combustion of non-traditionally manufactured propellant.

Additive manufacturing (AM) has been used in many industries to enable rapid prototyping and the construction of complex hierarchal structures. AM of propellant is an emerging research area, but it is still in its infancy since there are some large challenges to overcome. Namely, high performance propellant requires a minimum solids loading in order to combust properly and this translates into mixtures with high viscosities that are difficult to 3D print. In addition, it is important to be able to manufacture realistic propellant formulations into grains that do not deform and can be precisely functionally graded without the presence of defects from the printing process. The research presented in this dissertation identifies the effect of a specific AM process called Vibration Assisted Printing (VAP) on the combustion of propellant, as well as the development of binders that enable UV-curing to improve the final resolution of 3D printed structures. In addition, the combustion dynamics of additively manufactured layered propellant is studied with computational and experimental methods. The work presented in this dissertation lays the foundation for progress in the developing research area of additively manufactured energetic materials.

The appendices of this dissertation presents some additional data that could also be useful for researchers. A more detailed description of the methods necessary to support the VAP process,

additional viscosity measurements and micro-CT images of propellant, the combustion of Al/PVDF filament in windowed propellant at pressure, and microexplosions of propellant with an Al/Zr additive are all provided in this section.

1. INTRODUCTION

1.1 Motivation

In many industries, the design of an object is limited by the manufacturing process. Even though complex geometries or functionally graded materials can be used to optimize a design with respect to a specific performance requirement (i.e. heat resistance, mechanical strength, weight minimization, etc.), that design cannot be realized if it is impossible to manufacture. Optimization is extremely important in the aerospace industry, where costs scale up dramatically with weight and where advanced materials are necessary to overcome extreme environmental conditions. In order for research to expand beyond current limitations, disruptive manufacturing technologies and techniques must be introduced. One such disruptive technology that has gained traction in recent years is additive manufacturing (AM), or the process of joining materials to make objects from 3D model data, usually layer by layer (ASTM F2792-12a).

Many different AM, or 3D printing, techniques are commercially available depending on the type of material that is being processed and the desired properties of the finished product. However, the ability of AM to expand the feasible design space is still in its infancy. The first patented technique was granted to Charles Hull for stereolithography (SLA) in 1986 [1]. Even Fused Deposition Modeling (FDM), which is arguably the most commonly available commercial 3D printing technique, was patented only in 1992 to Scott Crump [2]. More recently, the cost of FDM has decreased significantly due to patent expiration in 2009. Therefore, it has only been about a decade that older 3D printing techniques have become commercially viable options for research and have been used to demonstrate various advantages over traditional manufacturing methods, such as machining or casting.

Several significant advancements in the design of components such as rocket engines, composite structures, and other materials have been made through the use of AM. However, the development of new 3D printing techniques will expand the list of materials that can be manufactured, therefore transforming the design of more components. One area that has been particularly lacking is the ability to additively manufacture extremely viscous materials, although the applications are extensive. A wide variety of viscous mixtures are fabricated with various traditional manufacturing methods, such as casting, injection molding, or others. Although these

methods have produced functional parts, there are many limitations that could potentially be overcome with additive manufacturing. For example, composite materials could benefit from enhanced control over fiber alignment within a structure, which is limited by the layup, winding, and injection molding methods that are typically used. The geometric design of particulate/binder systems with high solids loadings, such solid propellant and ceramics, are limited by the design of molds. In addition, the ability to manufacture a component out of two different types of materials that are intimately combined is sorely lacking, yet there is a strong interest from industry and government agencies to resolve those problems in order to exploit the potential advantages.

The purpose of this work is to demonstrate the ability of a modified direct write AM system called Vibration Assisted Printing (VAP) to manufacture viscous materials in ways that cannot be achieved with traditional manufacturing methods. VAP has previously been demonstrated to be capable of printing a variety of viscous mixtures for food, pharmaceutical, and aerospace applications. However, there is a strong desire to more thoroughly exploit new geometric and/or anisotropic designs with this AM process. This document outlines the method and approach for achieving the objectives of 1) additively manufacturing reliable, high quality propellant, 2) identifying and characterizing photopolymers that are compatible with opaque energetics and VAP, and 3) developing models and experiments to understand the combustion dynamics of additively manufactured propellants that are layered at fine scales (~1 mm). The scope of this research will be focused specifically on composite solid propellant with application to SRMs, although this research can more broadly inform the additive manufacturing, energetic materials, ceramics, and composites communities about new advances in 3D printing and the benefits that can be reaped from them.

2. BACKGROUND

2.1 Solid Rocket Propellant Performance

Solid rocket motors (SRMs) are used for a variety of applications, such as space shuttle boosters and missiles. They are convenient due to their simplicity and fast launch times. A typical design of a SRM can be seen in Figure 2-1. The most important component of a SRM is the solid propellant grain, because that is what generates a time-dependent thrust profile that is mission specific (i.e. optimized for speed or range). The combustion of the propellant grain is initiated with an igniter and the pressurized combustion gases are contained by the thermal insulation and motor casing. Those gases are then expanded through a converging diverging nozzle to generate supersonic flow. The nozzle is a key component for a SRM because it is highly related to the thrust efficiency and is responsible for generating supersonic flow. However, the nozzle experiences the high temperatures of solid propellant combustion (~3000 K), as well as chemical reactions from toxic hydrochloric acid (HCl) and condensed phases (i.e. alumina, water, or unreacted propellant) that impinges on the inner surface of the nozzle. In addition, the casing of the motor must be strong enough to withstand the pressurization of the propellant grain, or the motor will catastrophically fail.

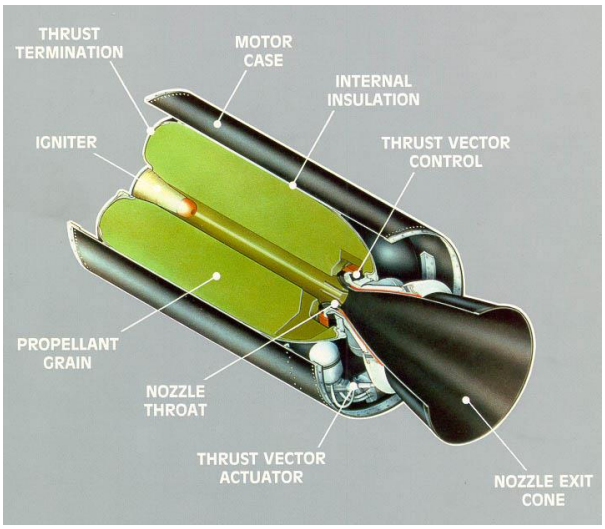

Figure 2-1. Schematic of a solid rocket motor [3].

Geometry has a significant effect on the burning rate of a propellant. The instantaneous burning of a propellant grain can be represented by

$$\dot{m}=A_b\rho_s r_b, \quad (1)$$

where $\dot{m}$ is the mass consumption rate, A_b is the burning surface area, ρ_s is the propellant density, and r_b is the linear burning rate [4]. The burning rate is also related to the chamber pressure as represented by

$$r_b=aP_c^n, \quad (2)$$

where a and n are parameters fitted from experimental data (pressure coefficient and pressure exponent respectively) and P_c is the chamber pressure [4].

There are many different types of thrust profiles, but the simplest types are progressive, neutral, and regressive. A progressive profile indicates that the thrust increases over time (accelerates), a neutral profile indicates that the thrust is relatively constant over time, and a regressive profile means that the thrust decreases over time (decelerates) [4]. A few well known core geometries and their corresponding thrust profiles can be seen in Figure 2-2. It is important to be able to have tight control over the geometry of a propellant so that the thrust profile is reliable and predictable.

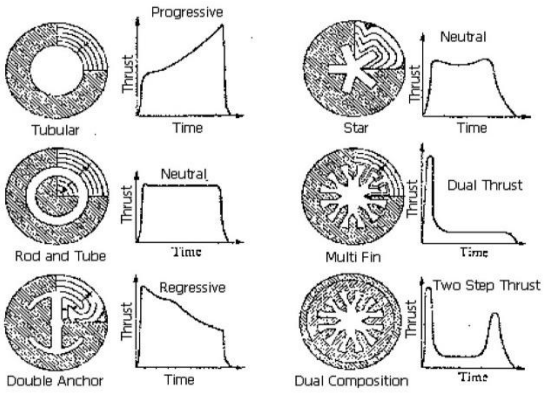

Figure 2-2. Propellant core configurations and associated thrust-time curves [4].

There are several types of solid propellant that can be used for a SRM, although for the focus of this work, we will only discuss composite propellant rather than double base propellants. If the propellant is composite, a high solids loading of particles are mixed with a small amount of binder as seen in Figure 2-3. Typically, ammonium perchlorate (AP) is used as the oxidizer and, for increased performance, 10-15 wt.% aluminum (Al) can be added. The solids loading of

particles in propellant is typically in the 80-90 wt.% range. If the solids loading is too low, the propellant will burn extremely slowly, could quench, or may not even combust. In order to improve propellant combustion and therefore increase the burning rate, is important to optimize parameters such particle size, coarse to fine ratio (ratio by weight of large particles to small particles in a bimodal formulation), and binder selection to increase the solids loading [4].

In general, propellants with high solids loadings have high viscosities, which can be problematic for casting. A smaller particle size distribution and a high solids loading have been shown to increase the viscosity of composite propellants [5-7]. Without proper processing parameters, cast propellant will have voids (due to air entrainment) that will lead to unpredictable burning. Therefore, binders are typically mixed with additives, such as plasticizers, to lower the viscosity, which makes propellants easier to cast into molds. In addition, the propellant can be heated slightly (40 - 60° C) to make it easier to pour into a mold and the use of a vacuum system to remove air can reduce porosity even further. Hydroxyl terminated polybutadiene (HTPB) is a common and often preferred binder for composite propellants because of its ability to bind together a high solids loading of particles and its desirable mechanical properties. In addition, HTPB can be thermally crosslinked with an isocyanate. The speed of crosslinking and the resulting mechanical properties are dependent on the type of curative used and the curing temperature. Essentially, a fresh propellant mixture constitutes a slurry with the consistency of wet sand and is transformed into a cured rubbery state with the consistency of a pencil eraser.

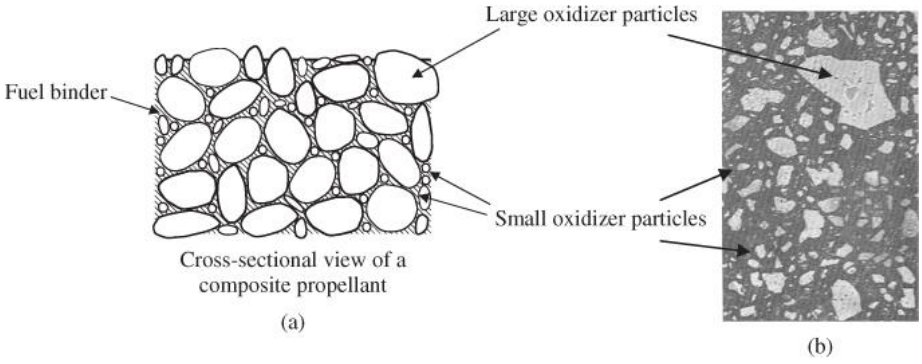

Figure 2-3. View of composite solid propellant with bimodal distributions [8].

However, there is a limitation on the complexity of the grain that can be constructed with traditional manufacturing methods. Typically, the core geometry of a grain is set by the design of a mandrel, which fresh propellant is poured around during the casting process. Ultimately, the

mandrel must be removed after the propellant has cured. Although many cross-sectional areas are manufacturable with this method, the grain geometry is still constrained even when tapering and coatings are used to facilitate mandrel removal. Machining of the grain [9] and melt out mandrels have been used to manufacture complex central port designs [10], but post-processing grains increases cost and production time and lowers reproducibility. Additive manufacturing has been used in many fields to improve the ability to fabricate parts with complex hierarchal designs with great success. Given that geometry affects the combustion of energetic materials, AM is being explored as a method to tailor the performance of propellants, pyrotechnics, and explosives.

2.2 Commercial Additive Manufacturing Methods

The choice of AM method for a particular application is mostly dependent on the material of interest. Fused Filament Fabrication (FFF), Stereolithography (SLA)/Multi-jet Printing (MJP), Electro-Spray Deposition (ESD), Binder Jet Printing (BJP), Selective Laser Sintering (SLS)/Selective Laser Melting (SLM), and Direct Ink Write (DIW) are the relevant AM methods for review in this section. A discussion of the uses and disadvantages of these methods will provide further insight on why new additive techniques are needed to produce high performance propellants.

FFF (also known as Fused Deposition Modeling) is an extremely common AM method that has be monumental in enabling advancements in academia and industry due to its low cost. It involves feeding a thermoplastic filament into a nozzle, heating the filament to its melting temperature (200 - 250 °C), and depositing the material into thin layers, which then cool into a fixed form as seen in Figure 2-4. Some particulate additives, such as Al or carbon fiber, can be included in the filament through custom filament manufacturing processes. However, there is a limitation on the solids loading of additives (~40 wt.%) that can be achieved before the viscosity of the filament is too high to extrude through 0.4 mm nozzles. In addition, heating the filament can be a point of concern for some energetic materials or additives that can decompose in the 200 - 300 °C range.

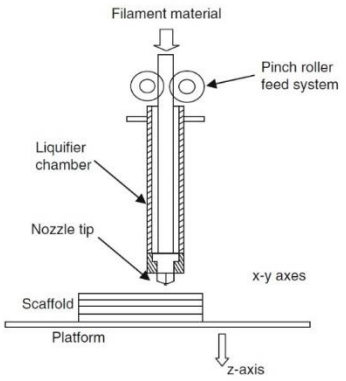

Figure 2-4. Schematic of Fused Filament Fabrication (FFF) [11].

SLA is an older AM method, but it is still commonly used in research to produce high resolution structures and is the basis for other faster AM methods such as Digital Light Processing (DLP). The method involves curing layers of photopolymer with UV-lasers. SLA is typically a high precision method compared to other AM techniques, but it is more expensive and it requires a large amount of photopolymer to fill a vat. MJP is a type of inkjet AM process. Photocurable resins and waxes can be deposited onto a printed surface through the use of piezoelectric printheads. Although this a cost friendlier method than SLA, it relies on the use of low viscosity polymers which can limit the range of materials used. MJP has been used previously to deposit thermites, but the mixtures had a low solids loading of fine particles [12]. Schematics of both methods can be seen in Figure 2-5. Both SLA and MJP are restricted to low viscosity photopolymers and are compatible with fine particulate inclusion, although to a limited degree (10-20 wt.%), since it is difficult to suspend particles in a vat or to prevent the nozzle from clogging. In addition, certain photopolymers do not have the best mechanical properties and may even lower the burning rate of the propellant.

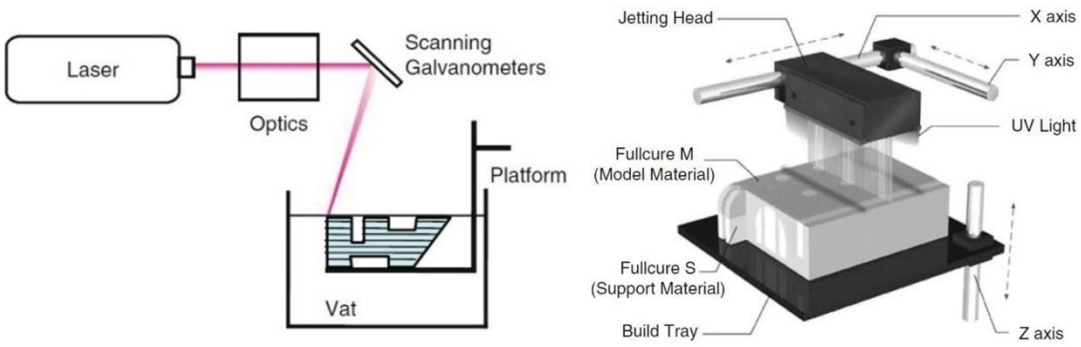

Figure 2-5. Schematics of (left) Stereolithography (SLA) and (right) Multi-jet printing (MJP) [11].

ESD is used to 3D print composite materials on the micro or nano scale (typically films). The process involves using a voltage to manipulate a charged liquid solution that flows through a nozzle into fine droplets. Particles can be included into the solution so that after each layer is printed, the liquid evaporates to form a solid film as seen in Figure 2-6. Some advantages of ESD are that film thickness, morphology, and uniformity can be controlled. Studies using ESD have produced reactive films with significantly higher solids loadings than other AM methods (50-60 wt.%), but beyond that point, there were issues with rheological properties [13, 14]. In addition, the film thickness was on the order of 100 μm, meaning that this process is more suited to the construction of thin films rather than larger structures. Lastly, geometric complexity is not particularly conducive to this method.

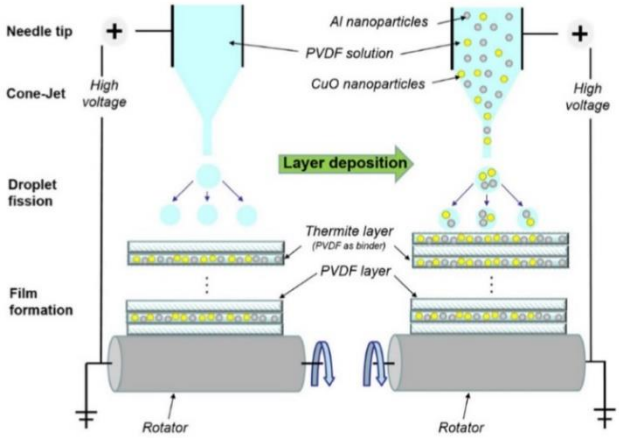

Figure 2-6. Demonstration of the Electro-Spray Deposition (ESD) of Al/PVDF [14].

BJP is similar to MJP in that an inkjet print head is used to deposit liquid droplets. Instead of depositing the droplets onto a cured photopolymer structure, the droplets are deposited onto a layer of powder held in a bed as seen in Figure 2-7. Low viscosity photopolymers are required to infiltrate the bed of particles. There is a limitation on how effectively the liquid can infiltrate a collection of particles while holding them together, so the solids loading of the final structure is inherently restricted. Although BJP might be able to 3D print ceramic parts with a mid-range solids loading (~ 50 vol.%), propellants typically use high viscosity binders, so this method would not work for that application. Even if a low viscosity polymer was used, the solids loading would still not be high enough to produce a realistic propellant formulation and it is likely that the mechanical properties of the final structure would not be satisfactory. Lastly, this method would require a significant amount of dry energetic particles to sit in a bed. This would not be possible for producing metallized formulations, since it is dangerous to mix dry Al and AP.

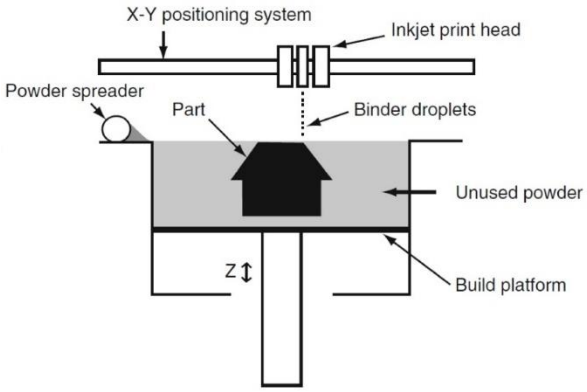

Figure 2-7. Schematic of Binder Jet Printing (BJP) [11].

Ceramic and metal parts can be fabricated with SLS or SLM respectively. The main difference between the processes is whether the laser energy is used to sinter or melt materials, but there are many similarities between them. Both processes involve a bed of powder which is then sintered or melted together with a laser to fabricate a part as seen in Figure 2-8. Although relatively dense structures can be fabricated this way, SLS and SLM are typically associated with poor surface finish and if the laser settings are not optimized, there will be pockets of porosity which will negatively affect mechanical properties. Ultimately, the use of lasers to combine energetic materials is not particularly safe.

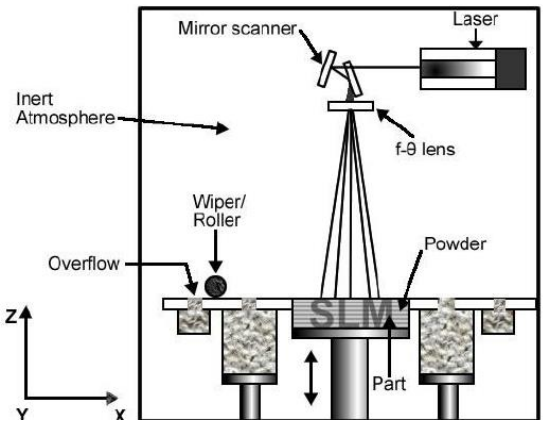

Figure 2-8. Schematic of Selective Laser Melting (SLM) [15].

DIW is a relatively common 3D printing method in academia because mixtures can be easily customized and deposited. However, there is an ultimate limitation on the maximum viscosity that can be extruded at a nozzle tip diameter of 1.5 – 2 mm. Typically, this issue has been combatted by using shear thinning agents or increasing temperature to artificially lower the material viscosity if one is printing with small nozzle tip diameters (<1 mm). However, high pressures, which are exerted by either pneumatic means, pistons, or screws as seen in Figure 2-9, can lead to material dewetting. While shear thinning agents may improve rheological properties, they decrease combustion performance since they are not energetic. In addition, DIW has issues printing discontinuous structures because the flow cannot be easily started or stopped.

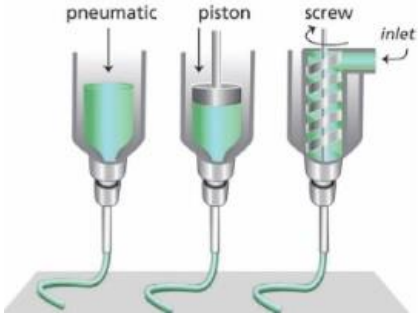

Figure 2-9. Various methods of Direct Ink Writing (DIW) [16].

The merits of AM have been demonstrated through the production of rocket hybrid fuels. Grains of acrylonitrile butadiene styrene (ABS) plastic have been 3D printed into well resolved designs using FFF and tested in small rocket motors [17]. However, the combustion efficiency of

ABS is less than HTPB, which is a baseline hybrid rocket fuel [18]. Metal additives that would improve combustion performance can only be added up to a small solids loading in the filament before the 3D printed grain experiences structural flaws (i.e. voids, defects) that negatively affect combustion [19]. In essence, there is a tradeoff between having a printable material that does not combust well or a slow burning fuel with structural problems, therefore making the high solids loadings that is necessary for solid propellant combustion unachievable.

Thin, consumable molds have been 3D printed so that there is no need for removal after casting composite propellant [20, 21]. While this might allow for the construction of more complex geometries, the molds are made of materials with low reactivity which can reduce the burning rate if printed too thickly. If the molds are too thin, they will not be able to hold the original intended shape when subjected to the weight of the propellant and shrinkage that results from the curing process. Lastly, it is still not possible to construct delicate complex internal geometries with this method. Hybrid grains have also been 3D printed directly out of photopolymers (via MJP) with swirling ports and some aluminum inclusion [22, 23]. Although the ability to vary the regression rate was demonstrated, only homogeneous, low performing fuels with low solids loadings (20 wt.%) could be 3D printed. An alternative AM approach is needed to produce high solids loaded hybrid fuels, as well as solid propellants. Given that high performing solid propellants have a solids loading that ranges from 80–90 wt.% [4], the 3D printing methods used for hybrid propellants would not be useful for producing solid propellants without further modification.

The viscosity of a material has been identified as a critical parameter for many AM methods when determining if a material is printable [24]. The main limitation of printing high solids loaded propellants using a nozzle based AM process is pushing the high viscosity mixture through a small nozzle diameter. Although shear thinning is a behavior that has been observed in many propellants [25], extremely high pressures are required to overcome mixtures with high viscosities (>1 million cP). Further, the separation of the binder from the particles (dewetting) under high applied pressures would lead to unacceptable and inconsistent results. If curatives are included in the mixture, rheopectic behavior, or the increase in viscosity over time, can further complicate the process of printing solid propellants. Although several inert ceramic pastes with mid-range solids loadings have been printed with DIW based techniques [26], current commercial printers are not adequate for application to solids propellants with high viscosities. Flow rate consistency and start/stop delay times are also factors that need to be characterized for quality control [27]. We

note here that high solids loadings have been achieved for certain nozzle based AM systems. A screw extruder has been used to print 82 wt.% solids loaded copper pastes [28], but this approach may result in safety concerns for energetic mixtures due to the pinch points which could initiate a reaction.

Mock energetic formulations with Sylgard have been manufactured with a syringe printer at a solids loading between 74 and 92 wt.%. However, fine particles (~5 μm) and solvents were required to print the mixtures with higher solids loadings and more importantly, the maximum viscosity was up 500,000 cP when real propellant formulations can be more viscous (>1 million cP) [29]. Recently, AP/HTPB propellant that was catalyzed with iron oxide was 3D printed, but no solids loading nor viscosity was reported and the formulation looked like a low viscosity slurry [30]. There was also no quantitative characterization of the print quality or comparison of the combustion performance between printed and traditionally manufactured grains.

Based on the literature in several different fields, no commercially available AM method that can print high viscosity mixtures at fine resolutions exists. A new, well characterized process is needed to achieve mixtures with high solids loadings and viscosities, resolve complex geometries, and print a wider range of energetic materials. In order to 3D print high performing solid propellants or ablatives, a new technique called Vibration Assisted Printing (VAP) [31] needs to be used (explained in Section 3.1).

2.3 Layered Propellant Combustion Literature

In general, the propellant formulation remains the same from grain to grain in a SRM. However, there are times when grains of different formulations may be stacked in a SRM to change the overall thrust profile. One could potentially vary the thrust profile of a SRM by layering propellant with different formulations on a smaller scale (~1 mm). However, little is known about how layered propellants, or other functionally graded configurations, perform at high pressure because it is too tedious and/or impossible to manufacture propellant in such a way without interlayer debonding or applying adhesives that would negatively affect performance. Despite some studies on the manufacturing and combustion of layered gun propellant [32-36], there is currently no published literature that the author is aware of on the experimental performance of layered composite rocket propellant, particularly at fine scales (~1 mm layers). With the emergence of new additive manufacturing techniques, particularly VAP [31, 37], it is possible to

layer different propellant formulations at this scale. Therefore, a fundamental study on the combustion of layered propellants is needed to inform the design of additively manufactured propellant grains.

2.4 Rocfire

Rocfire is a combustion simulation program that has been used to model the burning rates of composite propellant in the past [38, 39]. The program can also use sophisticated packing algorithms that can handle new particulate shapes, such as ellipsoids, cubes, and fibers [40]. Typically, particle distributions are packed into an unit cell of finite volume using packing algorithms. Then, the repeating unit cell is burned to obtain the simulated propellant burning rate [41]. Figure 2-10 shows examples of the unit cell and the regressing surface of a simulated propellant cross-section. Typically, the model is validated by using Miller's propellant formulations [42]. The model is currently unable to predict the burning rate of aluminized propellant well [43], so AP propellant is typically used for simulation. However, it does not appear that functionally graded composite propellant has been modeled before. There have been computational studies on layered AP and HTPB sandwich configurations [39], which are common for studying kinetics [44]. Figure 2-11 shows an example of how layered structures have been studied previously in Rocfire. Therefore, Rocfire is a good tool to investigate the combustion of layered propellant combustion. With the use of VAP, it is now also possible to experimentally explore the combustion of layered propellant.

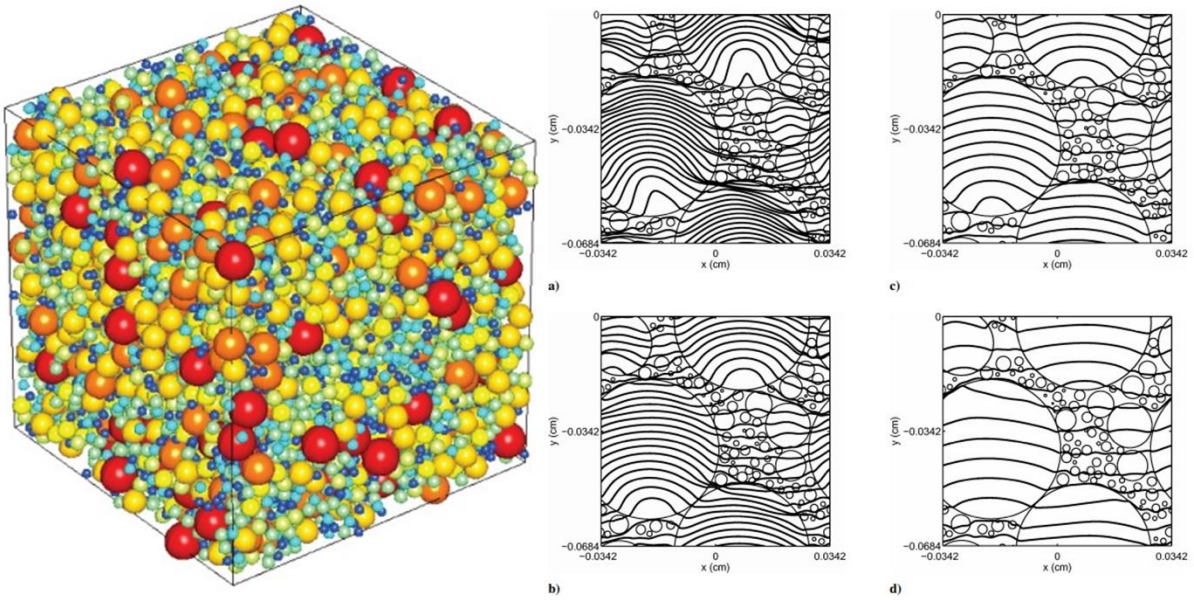

Figure 2-10. (Left) An example of an unit cell of a heterogeneous propellant generated via Rocpack and (right) surface regression of heterogeneous propellant [39].

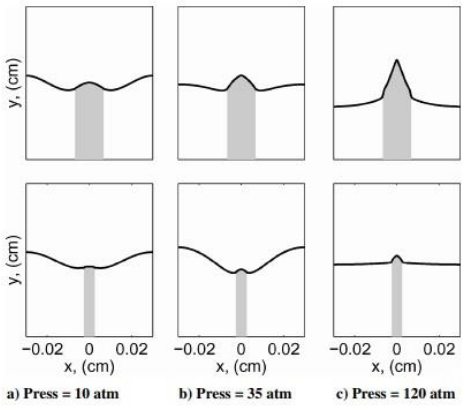

Figure 2-11. An example of an AP/HTPB sandwich combustion simulation with varying HTPB binder widths and pressures [39].

3. ADDITIVE MANUFACTURING OF SOLID PROPELLANT

Note that the content in Section 3.1 is based off of Reference [31] and has been rephrased where appropriate. The content in Sections 3.2-3.5 is based off of Reference [37] and has also been rephrased.

3.1 Vibration Assisted Printing

Vibration Assisted Printing (VAP) is a modified DIW system that is capable of printing high viscosity materials [31]. The use of high pressures to extrude the material out of a fine tip is not required because the flow of the material is initialized with high amplitude, high frequency vibrations. The vibrations are delivered through an ultrasonic probe that makes contact with the nozzle tip as seen in Figure 3-2. When no vibrations are applied, the material does not flow, but when the vibrations are applied, the material rapidly comes out. The mechanism for this behavior was explained by a stick-slip motion of the material with the vibrating nozzle walls (displacement ~15 μm), which ultimately prevented the material from experiencing wall friction for extended periods of time. The vibration also allowed for precise control over the deposition of material during discontinuous printing, which is difficult to achieve with traditional DIW systems. With optimal settings, there was no porosity in the samples and fine resolutions (0.6 mm nozzle tip diameter) could be achieved with VAP. Materials with viscosities about 1000 Pa*s or greater were successfully printed and the shape of the printed parts were well retained afterwards as seen in Figure 3-1.

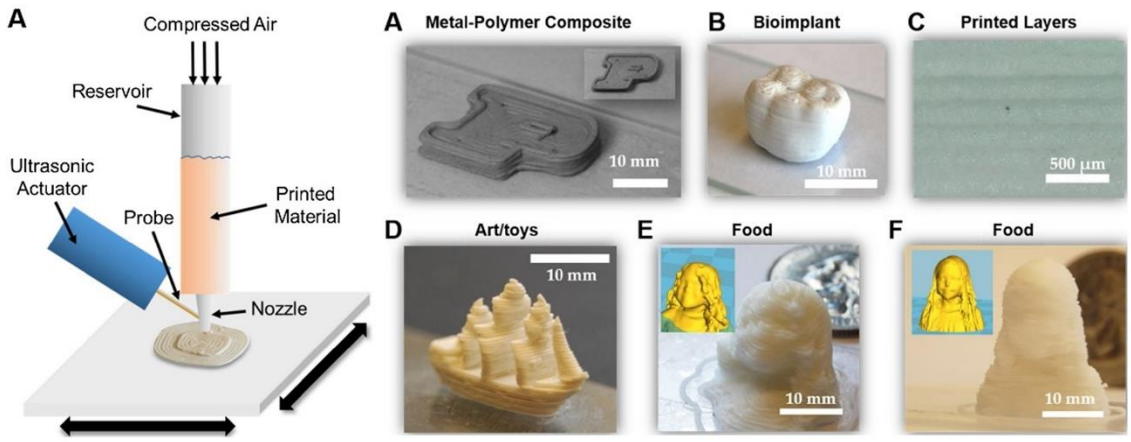

Figure 3-1. Schematic of Vibration Assisted Printing (VAP) and demonstration of its capabilities to print viscous materials [31].

Since VAP has demonstrated its ability to be a process that can handle a versatile selection of materials, it seemed that it would be a useful technique to apply to viscous energetic mixtures. The rest of this document will outline how VAP has been used to manufacture AP composite propellants.

3.2 3D Printed Propellant

The goal of this study was to pick a propellant formulation that would be comparable to a realistic mixture used in a SRM and that could still be 3D printed into a high quality grain. A quick mini study was conducted to select an optimal mixture for printing. If the viscosity was too low, then the propellant would deform easily. If the viscosity was too high, then the propellant would not print consistently, which would create voids. Ideally, one would want a smooth continuous stream of material to be deposited and for the printed structure to retain its shape afterwards. Figure 3-2 shows the difference in varying the coarse to fine ratio (CFR) of AP particles in 3D printed propellant with 85 wt.% solids loading. The coarse particles were 60–130 µm (Firefox) to prevent clogging the nozzle and the fine particles were 20 µm (ATK) AP. The binder formulation is described in the next paragraph. The CFRs tested were 4:1, 7:3, 3:2, and 1:1 and a monomodal coarse mixture was also tried. It was found that the ratios with more coarse particles printed easily, but also deformed easily, whereas the propellant with the CFR of 1:1 seemed to hold its shape the best.

Figure 3-2. Top views of 3D printed propellant strands with 85 wt.% solids loading and varying CFR. 3D printed (left) monomodal coarse propellant (which is slightly deformed), (middle) propellant with a CFR of 4:1 (which has overhang), and (right) propellant with a CFR of 1:1 (which maintains shape well).

The final propellant mixture chosen had a solids loading of 85 wt.% and a CFR of 1:1 of 60–130 μm (Firefox) and 20 μm (ATK) AP (see Reference [43] for size distributions). The AP was sieved below 180 μm to prevent agglomerates from clogging the syringe tip during the printing process. HTPB is a typical solid propellant binder due to its favorable ability to produce mixtures with high solids loadings and its desirable mechanical properties. However, HTPB is known to deform while it is curing, so there was interest in exploring UV-curable binders which can rapidly cure. Therefore, one type of propellant was made with HTPB binder (73 vol.%) and the other was made with a UV-curable polyurethane epoxy (Illumabond 60–7105) with a slightly higher density of 1.06 g/cc (76 vol.%). The HTPB binder mixture was 75.25 wt.% R-45M polybutadiene resin (Firefox), 15.05 wt.% isodecyl pelargonate (IDP) (Rocket Motor Components), 1.53 wt.% Tepanol (Firefox), and 8.27 wt.% isophorone diisocyanate (IPDI) (Firefox). The AP was weighed separately in weigh boats and the binder ingredients were hand mixed vigorously for at least one minute in a 5 g batch (if the binder is not stirred vigorously, then the ingredients do not mix enough and crosslinking becomes hindered). The 5 g batch was necessary to make it possible to measure small amounts of binder ingredients and to promote a more homogenized mixture. The appropriate amount of binder for the propellant was measured into the final mixing container and the AP was slowly added and wetted via light hand mixing.

In order to ensure complete mixing in a resonant acoustic mixer, a jar should be mostly full (~70%) with ingredients. Therefore, 20 g batches of propellant were mixed in 473 mL jars (McMaster Carr). The closed container with the propellant was secured in the resonant acoustic mixer (LABRAM Resodyn). The HTPB propellant was mixed at an intensity of 80 g's for 3 min a few times. In between cycles, the container was removed and the propellant was slightly hand mixed further to scrape the corners of the container where the propellant was not mixing well. The UV-propellant was mixed in a container wrapped in electric tape to block out UV-rays during transportation. Then, it was mixed in the Resodyn for 2 min at an intensity of 80 g's for 30 s followed by a rest period of 30 s. This on-off cycle was necessary to prevent the UV-propellant from hardening since it was sensitive to local heating induced by the friction driven mixing process. Typically, HTPB contains additives that cause it to off gas during the casting process. Therefore, degassing propellant is a common method to reduce porosity. The HTPB propellant was placed in a vacuum environment for 5 min after resonant acoustic mixing. Some propellant batches were reserved for casting, while others were made for the printing process. Cut pipets with a diameter of 6 mm were used as a mold for the cast propellant. The propellant was cast one day after preparation so the propellant would off gas less and the ends of the pipets were constrained to improve the density of the strands. Since IPDI is known to cure slowly at room temperature, the propellant was still castable the following day. The cast strands were placed in an oven set at 60 °C for three days to cure. Then, the pipet casing was removed and the propellant strands were cut to a height of approximately 22 mm. The UV-curable propellant was cast in pipet molds cut to the length of 22 mm beforehand and was then cured with a UV-lamp for 30 min.

Propellant mixtures that were not cast were prepared for 3D printing by packing them into a taper tip syringe (Zoro) with a diameter of 600 μm. A slight back pressure of 0.138–0.690 MPa was used to compress the propellant in the reservoir and to facilitate flow towards the tip. Printing did not occur until at least two hours after mixing in order to allow the propellant viscosity to settle to a steady value after the initial gel time, but before the viscosity build up that occurs from curing. Fresh mixtures were not adhesive enough to come out of the nozzle as a smooth and steady flow at low-reservoir pressures (< 0.138 MPa). The variability in flowrate made it difficult to produce high quality strands with no induced voids at these conditions. It was observed that steady viscosity, and therefore flow rate, occurred 3–7 hrs after the addition of the curative. Beyond that time frame, viscosity buildup would occur which would cause the flow rate to slow down to the point where

the strand could not be printed in a reasonable amount of time or where the nozzle would clog. The UV-curable propellant mixture maintained consistent properties over a few days as long as the mixture was not exposed to light.

The VAP head was controlled by a frequency of 30.3 kHz and the resulting amplitude of the tip displacement was 8 μm. A GCODE file of a 7 x 7 x 25 mm strand was generated in Cura 15.04.2 and was postprocessed further to control the activation of the VAP head during the print. To prevent local heating of the nozzle tip, the VAP vibrations were not run continuously. In addition, an external fan was positioned at the tip to help keep the temperature below 30 °C (temperature was monitored with a handheld IR camera). With this limited degree of temperature control, there is confidence that the local heating of the propellant was not the main mechanism to cause propellant to flow out of the nozzle tip. Figure 3-3 provides a demonstration of the propellant deposition process. Initial adhesion to the double sided tape applied on the surface of a glass slide was critical for the printing process. The 3D printed propellant strands with a traditional HTPB binder were cured at an elevated temperature of 60 °C for 3 days, whereas the finished 3D printed UV-binder strands were cured under a UV-light for 30 min.

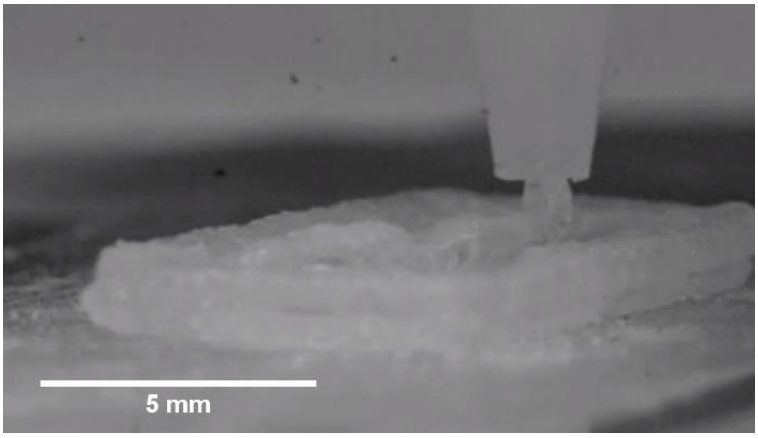

Figure 3-3. VAP head depositing propellant into a 7×7×25 mm strand shape. High energy, high displacement ultrasonic vibrations are delivered at the tip to start or stop the flow [37].

A Brookfield DVII+ Pro HB viscometer was used to measure the viscosity of a large batch of HTPB propellant starting 60 min after the addition of the curative (IPDI). A batch of 250 g of propellant was made to fill approximately 140 mL of a 150 mL beaker. Based on a prior mini study (see Figure D-1 in Appendix D), there was little difference between the measured viscosity of test material in a 150 mL beaker and the manufacturer recommended configuration of 500 mL of test

material in a 600 mL beaker. This is because viscous mixtures like slurries or pastes often require T type spindles with small diameters for viscosity measurements, so the spindle is far away from the wall which could artificially raise the viscosity measurement (wall effects).

Rotating T types spindles in viscous slurries are known to create channels of air within a pass of the spindle, which will affect measurement if the spindle rotates through that region more than once. To eliminate the possibility of making a measurement through a channel, the spindle was lowered at a rate of 22.23 mm per minute with a Helipath stand. The descent path was 6.6 cm to prevent measurement too close to the bottom of the beaker where the viscosity measurement increases due to wall effects. The propellant was manually compressed into the beaker between each trial to remove channels created from the previous measurement. In order to prevent inaccurate readings, no measurements were taken until 60 s after the rotating spindle entered the top surface of the propellant. During the descent of the T-F spindle, data was recorded every 10 s and then averaged to represent a single viscosity measurement at each time interval. It is noted that while it takes about a few minutes to complete a pass, which is supposed to represent one measurement in time, it was important to quantify the spatial variation in the viscosity of the propellant rather than rely on one instantaneous measurement. The time interval for each spindle descent was every 10 min for 60 min. After the first 60 min, subsequent measurements were collected hourly until the viscosity buildup was measurable and the propellant was noticeably hardening to the point where it was difficult to repack between each test. No temperature control was used during the tests.

When a curative is added to a HTPB mixture, temperature dependent crosslinking causes the propellant to harden over time as the rubbery matrix thermosets (see Figure D-5 in Appendix D). Time dependency is an important factor to consider during 3D printing since several time consuming steps are necessary to 3D print a propellant strand. Figure 3-4 shows the dependency of the propellant viscosity over time. Initially, the viscosity fluctuates because of the propellant gel time. Afterwards, the viscosity remains relatively stable until viscosity build up occurs. Regardless of the care taken in the viscosity measurement process, it was difficult to get low error on viscosity measurements of heterogeneous slurries because of agglomeration [6], inconsistent packing of the propellant in the beaker, the production of gases during cross linking, and incomplete propellant mixing. Spatial and time dependent variation in viscosity can lead to inconsistent flow rates, which can produce strands with extremely over and underfilled layers if

the flow rate is not constantly monitored and the VAP parameters are not adjusted to compensate. An example of a strand printed with a varying flow rate without proper adjustments can be seen in Figure H-2 (Appendix H). Waiting at least 3 hrs to print the propellant led to fewer necessary adjustments and higher quality propellant strands. The viscosity data in Figure 3-4 also verifies this observation. The propellant was pliable after 4 hrs, firm after 23 hrs, and fairly solid around 30 hrs. The average viscosity of the HTPB propellant mixture was 69 million cP. However, the viscosity in the 3-13 hr range is closer to 50-60 million cP.

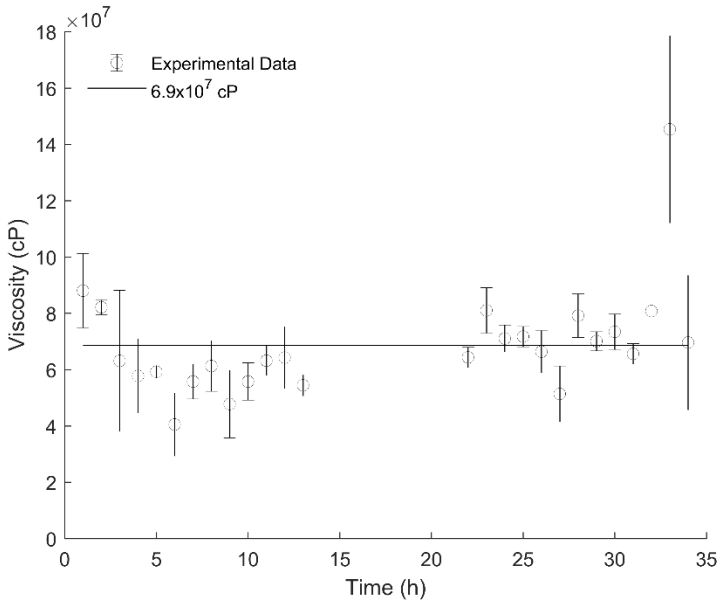

Figure 3-4. Viscosity measurements of the AP/HTPB propellant over time. Time is measured from the addition of the curative [37].

3.3 Propellant Quality

The average dimensions of the HTPB strands were 7.9 ± 0.4 mm (width), 6.0 ± 0.3 mm (height), and 25.9 ± 0.4 mm (length) compared to the CAD dimensions of 7 ×7 ×25 mm. Although the propellant was intentionally stiffened with more fine particles, there was still some slight deformation before the strands were cured into place. The tradeoff between depositing too much material with high flowrates (results in deformation) and depositing too little at low flowrates (results in voids) can be challenging. However, preference goes to producing strands without voids since even small gaps can lead to convective burning at high pressure. Even still, the strands were printed with smooth surfaces as seen in Figure 3-5. The strands with the UV-binder did not have as much time to deform before being cured at the end of a print.

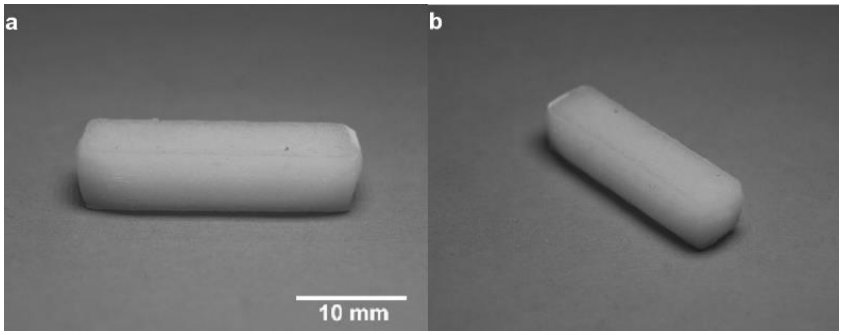

Figure 3-5. Different views of the same 3D printed HTPB propellant strand that has been cured. No voids are visible on the surface [37].

In order to analyze the internal microstructure of the cast and printed strands, X-ray micro-CT (Bruker Skyscan 1272) was used. A 80 kV intensity with an aluminum 1 mm filter was selected and the scan was calibrated for an average intensity between 60 and 61% without flat field correction and between 86 and 87% with correction as per the recommendations of the manufacturer. The resolution of the scans was between 7.5 μm and 11 μm. Using complementary software, the images were post-processed to reduce beam hardening effects, noise, and ring artifacts. In addition to analyzing the microstructure, the strand densities were measured via ASTM standard D792-13. A precision scale (RADWAG) with an error of 1 mg was used to measure the mass of the strands in air and in deionized water at room temperature. 36 gage nichrome wire was used to suspend the sample in water.

The microstructure of the printed and cast HTPB strands showed some porosity. The densities of the cast and printed HTPB strands were 1.45 ± 0.09 g/cc and 1.55 ± 0.03 g/cc compared to the theoretical value of 1.68 g/cc. Figure 3-6(a) shows the microstructure of a printed HTPB strand which has isolated voids. Figure 3-6(b) shows the microstructure of a cast HTPB strand which has larger isolated voids than the printed strand. It is believed that gas generation comes from the addition of Tepanol, which is known to react with AP to improve bonding at the expense of releasing ammonia gas. The gas becomes trapped if Tepanol based propellant mixtures are not made for long times under vacuum. It appears that printing improves the microstructure of the propellant in spite of the gas generating binder formulation that was used. The discovery of formulation based porosity initiated a mini study on the effect of the mixing method, binder formulation, and degassing time on the propellant microstructure to inform future studies. The results of that study can be seen in Appendix H, specifically in Figure H-1 and Figure H-2.

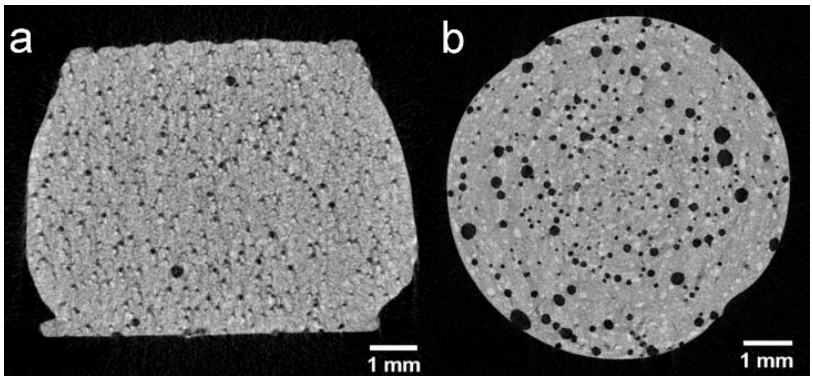

Figure 3-6. Micro-CT cross-sections of a HTPB binder propellant strand that was (a) 3D printed and (b) cast. The black holes are voids [37].

Figure 3-7 shows microstructures of printed and cast strands with the UV-binder. There was much less porosity seen, meaning that there was no off gassing from reactions between the binder and the AP. The densities of the cast and printed strands were 1.55 ± 0.06 g/cc and 1.75 ± 0.03 g/cc compared to the theoretical value of 1.73 g/cc. Given that the printed UV-strand was practically a fully dense propellant, it was concluded that the VAP process did not induce voids or gaps into the HTPB propellant strands. Printing propellant with an effectively constant viscosity allowed for controlled deposition of propellant into a high quality structure. The only limiting factor with the UV-binder was its sensitivity to vibration from the VAP process. The propellant mixture would often clog, making it difficult to manufacture multiple propellant strands. However, since there are many possible photopolymers to choose from, further study on a photopolymer that was compatible with energetic materials and was not vibration sensitive was warranted. The results of that study can be found in Chapter 4.

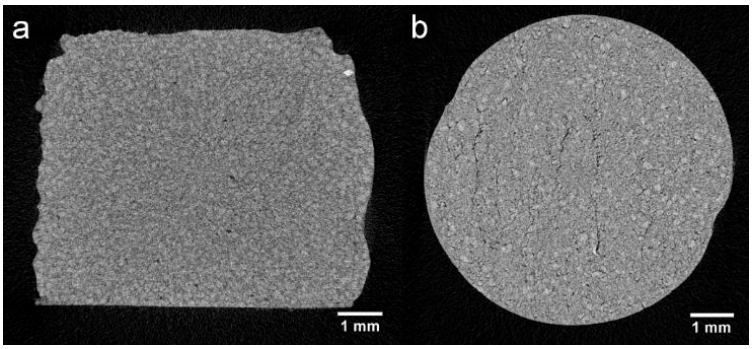

Figure 3-7. Micro-CT cross-section of a UV-binder propellant strand that was (a) 3D printed and (b) cast. The black holes are voids [37].

3.4 3D Printed Propellant Combustion

A Crawford bomb pressure vessel was used to obtain burning rate measurements of the printed and cast HTPB strands. The vessel was filled with nitrogen and the strands were ignited with 28 gage nichrome wire. The sides of the strands were inhibited with clear nail polish to facilitate a flat burning surface. A Vision Research Phantom v.10 high-speed camera recorded the combustion events at a frame rate of 2000 fps. The burning rates of the propellant were obtained manually using Phantom Cine Viewer software.

The flat combusting surface of the printed HTPB strands at elevated pressure can be seen in Figure 3-8. A flat burning surface is indicative of high quality propellant and of conductive burning. Flame spread into cracks, known as convective burning, would be indicative of low quality propellant. The printed HTPB strands were easily ignited and the flat burning surface of the printed strands proves that VAP is a viable manufacturing method that does not result in catastrophic strand failure. The burning rate curves of the cast and printed propellant seen in Figure 3-9 show the repeatability of measurement. Only one strand had a void that produced a nonplanar burn at high pressure, so that data point was omitted.

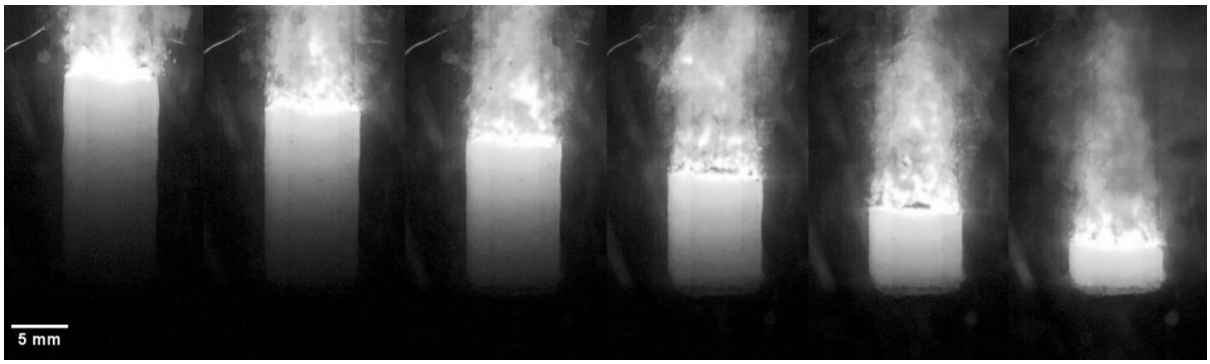

Figure 3-8. A printed HTPB strand burning at 10.34 MPa with 300 ms between each frame [37].

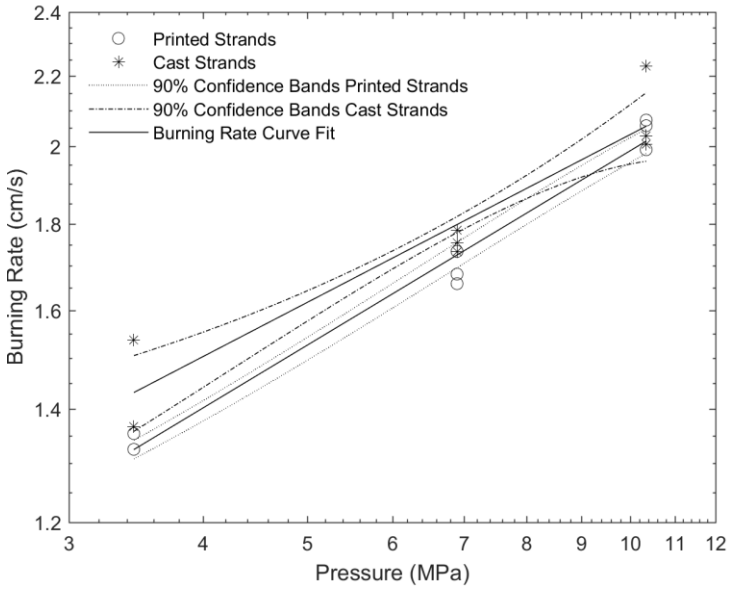

Figure 3-9. The burning rate curve of printed and cast HTPB strands at 3.45, 6.89, and 10.35 MPa. The burning rate curve fits of the printed and cast strands according to St. Robert's law are $0.826 * P^{0.38}$ and $0.952 * P^{0.33}$, respectively [37].

The burning rate curves of the printed and cast HTPB strands were effectively the same because there is overlap in the data at each pressure. In general, the burning rates of the cast strands were slightly higher, but note that the strands were more porous, which will slightly increase the burning rate. The burning rate curve fit of the cast UV-propellant was $0.622 * P^{0.31}$. When comparing the UV-propellant burning rate curve to the HTPB propellant burning rate curve, the UV-propellant burned considerably slower.

In addition to comparing the combustion of fully 3D printed and cast HTPB strands, introducing new geometries into a strand made of UV-propellant was considered. Figure 3-10 shows the combustion of a strand made of a fully dense upper portion and an intentionally porous lower portion. As expected, the combustion of the strand transitioned from conductive to convective burning when the flame front reached the intentionally placed internal gap in the strand. One should note that small internal gaps can currently not be manufactured in propellant grains made with traditional methods.

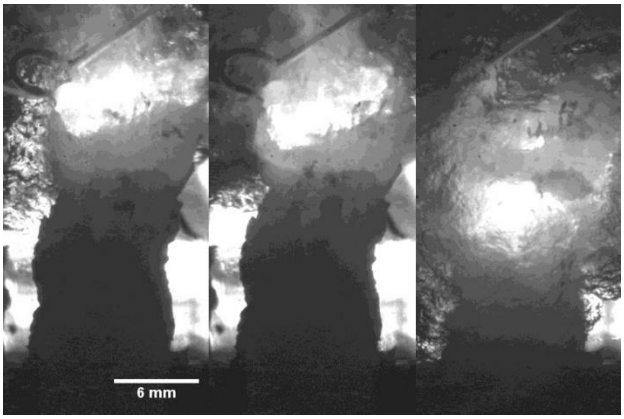

Figure 3-10. Functionally graded UV-propellant strand burning at 6.89 MPa [37].

3.5 Conclusions

VAP was used to additively manufacture high quality strands of propellant with extremely high viscosities (>10 million cP) for the first time in this study. The burning rates of printed and cast HTPB strands were effectively the same, which is significant because that means that VAP can be reliably used to manufacture propellant structures. Analysis of the microstructure revealed that the HTPB propellant suffered from some formulation issues, but the voids were not significant enough to lead to catastrophic burning. In addition, the less than optimal formulation revealed the need for a mini study to improve future formulations (see Figure H-1 and Figure H-2 in Appendix H). The microstructure of the printed and cast UV-binder propellant strands showed minimal, if any, porosity.

Another significant result was that the VAP process improved the microstructure of both formulations, rather than negatively affecting combustion performance. The binders used in this study presented some unique tradeoffs: the HTPB strands had some porosity and deformed a bit, but burned well, whereas the UV-propellant had effectively no porosity, but burned slow and clogged too frequently during the printing process due to its sensitivity to vibration. A photopolymer studied in Chapter 4 attempts to reconcile these tradeoffs. In addition, a simple example of spatial gradation was demonstrated with the UV-propellant.

The VAP technique in this study laid the foundation for constructing highly tailored propellant as seen in future chapters of this thesis. This study in particular was significant for being the first study to demonstrate additive manufacturing of a realistic propellant formulation (85 wt.% and a viscosity of 69 million cP) without sacrificing combustion performance or print quality.

4. UV-CURING OF SOLID PROPELLANT

Note that the content in this chapter is based off of Reference [45] and has been rephrased where appropriate.

4.1 Photopolymer Selection

Although VAP is a viable way to manufacture propellant, HTPB is not a suitable binder for 3D printing large or complex structures because it deforms easily even under its own weight at small heights. This occurs because the crosslinking process of HTPB is slow. Even if this process was accelerated with fast-acting crosslinkers, the working time of the propellant may not be long enough to be 3D printed without large changes in viscosity. In addition, particle size selection and solids loading will only partially mitigate deformation. Therefore, it is necessary to investigate binders that can set quickly and that are compatible with energetic materials. In Chapter 3, a polyurethane epoxy (Illumabond 60-7105) was used, but it was also extremely sensitive to prolonged vibration (over 30 s) and hardened quickly. This caused the syringe tip to clog easily. In addition, the viscosity of this propellant mixture was much higher than that of the HTPB propellant, so it took longer to print strands. The final mechanical properties of the UV-cured cast strands were also less than ideal (little force was required to crumble the strands). Since there are many well know photopolymers available with tunable properties (i.e. viscosity, adhesion, less sensitivity to vibration, and mechanical properties), it made more sense to look for a new UV-curable binder.

Photopolymers are a broad and versatile class of polymers that can be cured in a matter of seconds/minutes when subjected to UV-light or electron beam radiation and have been well adapted to several types of additive manufacturing processes (i.e. SLA and MJP). Photopolymers can be composed of 50-80 wt.% oligomer, 10-40 wt.% monomer, and ~1 wt.% photoinitiator [46]. Free radical photopolymerization can be used for quick curing at a limited depth (controlled by the wavelength and intensity of the UV-source [47]). The process involves free radicals breaking off of the photoinitiator and reacting with the monomers and oligomers [48].

Polybutadiene urethane acrylates are highly customizable and also have similar properties to HTPB (viscosity, adhesion, and hardness). When mixed with monomers, the mixture properties

can be tailored even further. The photoinitiator is important to consider since those that are responsive to a longer wavelength result in thicker coatings. For consideration with solid propellants, photoinititiors with wavelengths in the upper 300 nm or deep UV-range were vetted. Bisacylphosphine oxide (BAPO), a solid powder that cures at ~365 nm, was chosen since it was easy to add to a propellant mixture and was generally less volatile than other photoinitators with the same UV-wavelength range. BAPO can be mixed even better if hexanediol diacryalte (HDDA) is present, since BAPO is slightly soluble in this monomer. In addition to aiming to achieve large cure depths in propellant, one needs to consider the addition of opaque additives, such as aluminum (Al), in the UV-curing process since they can limit the penetration depth of the UV-light [49-52]. Common propellant formulations include 10-20 wt.% Al since it can increase the propellant burning rate, so it is imporant to select a binder that is compatible with such additives.

The focus of the study presented in this chapter is to study the effect of UV-curing parameters and Al content on the cure depth of propellant, which is much needed information for controlled curing of propellant into complex geometries in the future.

4.2 Photopolymer and Propellant Formulation

The viscosities of the individual ingredients selected were vastly different. The polybutadiene urethane acrylate does not move at room temperature and has a reported viscosity of 15,000 cP at 60 °C, while HDDA has a viscosity of 5-8 cP at 25 °C. To improve mixing between the ingredients, a sonifier (Branson) was used [53] and the acrylate was preheated to 60 °C to help with measurement/processing. Multiple 20 s cycles of 20% intensity vibrations from the sonifier dispersed the oligomer chains temporarily. The viscosity mismatch was not particularly an issue for propellant mixtures, but it did present a slight challenge for photopolymer tests. The final composition for this study was 50/49/1 wt.% of acrylate, HDDA, and BAPO.

The formulation was largely chosen because in a previous mini study, a very close version of this formulation was shown to be more reactive than the other formulations. The formulations in the mini study involved were 1) 50/49.9/0.1 acrylate, HDDA, and BAPO, 2) 50/49.9/0.1 HTPB, HDDA, and BAPO, and 3) Illumabond 60-7105. A preliminary test configuration (a refined version is described in Section 4.3) was used to determine how quickly the mixtures would reach a peak reaction temperature after a 365 nm UV-light was activated. The photopolymers and mixtures with 85 wt.% sugar were tested and an IR camera was used to record the temperatures. It

was found that formulation 1 reached a peak temperature of 107.6 °C in 14 s and the peak temperature of the sugar mixture reached was 39 °C in 6 s. Formulation 2 reached a peak temperature of 49.1 °C in 31 s while the sugar mixture reached a temperature of 26.5 °C in 32 s. Lastly, formulation 3 reached a peak temperature of 60.4 °C in 9.7 s and the sugar mixture reached its peak temperature of 34.4 °C in 10 s. None of the temperatures in this study were normalized with respect to the ambient temperature.

Formulation 2 was an attempt to add a photosensitive monomer and photoinitiator to the non-photosensitive HTPB polymer in the hopes that it could partially UV-cure the mixture enough to preserve a shape while the rest was thermally crosslinked later, whereas formulations 1 and 3 were completely photosensitive. Based on the reactivity, spiking the HTPB was not effective since the reaction temperatures were low and slowly increased and the curing was patchy. In addition, the end product did not have any rigidity. Formulation 1 was the most reactive mixture and it cured the fastest, so it was the best candidate for future study. The only change made was the percentage of photoinitiator. The value was increased from 0.1 to 1 wt.% since it was very difficult to accurately measure 0.1 wt.%. It is also likely that the reactivity slightly increased as well with the addition of more photoinitiator.

The final selected mixture of 50/49/1 wt.% of acrylate, HDDA, and BAPO was mixed in a 200 g batch in a 12 oz container (Cary Company). The same batch was used for all of the photopolymer and propellant cure depth tests in the rest of this chapter. The photopolymer and propellant was stored in containers wrapped in electrical tape to prevent polymerization from ambient light. A Brookfield DVII+ Pro HB viscometer with a H-1 spindle was used to estimate the viscosity of the photopolymer mixture after sonification. At 14.8 °C and 20 RPM, the viscosity measured was 436 cP. One should note that the reported viscosity of HTPB per the technical data sheet from Rocket Motor Components is 8000 cP at 23 °C and the acrylate hardly moves at room temperature. The acrylate is also extremely sticky on its own (has excellent adhesion to PMMA, polypropylene, and ABS), but the adhesion and the viscosity can be tempered with the addition of a monomer. Good adhesion of the binder to energetic particles can be beneficial for improving the density of the final product and for reducing binder-particle delamination.

Five 20 g batches of AP propellant with varying Al content (0 to 20 wt.%) were mixed in a resonant mixer using the same mixing profile as the HTPB propellant described in Section 3.2. There was no hardening of the propellant after multiple 3 min cycles at high intensity, which

indicated that the photopolymer was not sensitive to vibration like the Illumabond epoxy. The solids loading of all of the mixtures was held constant at 85 wt.% (72.5-73.8 vol.%) and the CFR of 60-130 µm to 20 µm AP (sieved below 180 µm) was 1:1. The aluminum of choice was -40 +325 mesh and 99.8% purity.

4.3 Design of the Cure Depth Experiments

A test was designed to quantify the cure depth because an applicable standard could not be found in literature. An AmScope LED-6W light with variable intensity and 365 nm and 395 nm lights were used to control the degree of cure in the photopolymer and propellant specimens. In order to calculate the intensity of the lights, the power and the beam diameter were measured. A Gentec MAESTRO laser power and energy meter and a XLP12-3S-H2-D0 laser power detector with an area of 1.119 cm^2 was used to measure the minimum and maximum power of each light. The lowest and highest power settings were chosen to improve the repeatability of the test, since it was very difficult to consistently set a slider to the same middle location every time. The power of the 365 nm light was 2.9 ± 0.1 mW at the minimum setting and 88.5 ± 0.1 mW at the maximum setting and the power of the 395 nm light at minimum and maximum settings were 4.5 ± 0.1 mW and 118 ± 1 mW respectively. The full schematic is shown in Figure 4-1(a) and a picture of a circular beam (diameter measured with calipers) in Figure 4-1(b). The intensity was calculated by dividing the power by the measured beam area.

Although this method gave a reasonable estimate of the intensity, the beam diameter was not measured relative to the propellant surface. Instead, it was measured on the counter because it would be difficult to know precisely how high off of the counter the propellant surface would realistically be and that would introduce more error into the calculation. It is still worth noting that the measured intensity will be slightly different than the intensity that the propellant sees, so based on the assumption that the propellant would be displaced 3 to 5 mm upward, new intensity values were calculated. The divergence of the beam was calculated to be 8.6° by measuring the beam diameter, the diameter of the projected light on the counter, and the height difference between the beam and the light. By knowing the divergence angle and by selecting an estimated upwards displacement, one can correct the beam intensity. As previously noted before, it is difficult to estimate the correction necessary, so it is best to simply use the measured beam diameter on the counter to estimate the intensity. However, this is only a meaningful estimate if the displacement

is small. Tables 4-1 and 4-2 represent the intensities if a 5 mm correction is assumed for the photopolymer and propellant cure tests respectively. Note that the absolute error is small for the lowest power setting (~0.06-0.09 mW/cm^2) yet higher for the highest power setting (~1.5-2.5 mW/cm^2). The percent increase in the intensity is on the order of 10%.

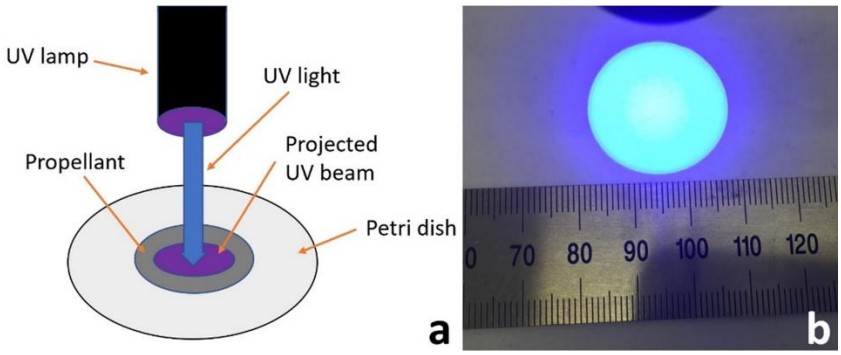

Figure 4-1. (a) The configuration of the UV-cure depth tests of propellant disks and (b) the UV-beam area measurement [45]. The figure is modified from the published (black and white) version.

Table 4-1. The measured and corrected intensities of the UV-light sources used for the photopolymer cure depth tests [45].

Wavelength (nm)	Setting	Measured Intensity (mW/cm^2)	Corrected Intensity (mW/cm^2)
365	Min	0.59	0.65
365	Max	18.03	19.89
395	Min	0.92	1.01
395	Max	24.04	26.52

Table 4-2. The measured and corrected intensities of the UV-light sources used for the propellant cure depth tests [45].

Wavelength (nm)	Setting	Measured Intensity (mW/cm^2)	Corrected Intensity (mW/cm^2)
365	Min	0.56	0.63
365	Max	17.06	19.27
395	Min	0.85	0.95
395	Max	22.16	24.99

The independent variables of interest were exposure time, UV-wavelength, and intensity for the photopolymer tests. Several 11.36 g amounts of photopolymer mixture (from the 200 g batch mentioned in Section 4.2) were dispersed in petri dishes (McMaster Carr 3854T11). The amount of 11.36 g was calculated based on the goal of filling the petri dish area to a uniform thickness of 2 mm. The propellant was pressed into disks that were 3 to 4 mm high with a 30 mm diameter to limit the waste of excess propellant. A thermal camera (FLIR A325sc) was used at a frame rate of

30 fps to monitor the heat produced from the photopolymerization. Heat release from photopolymerization could be indicative of the degree of reaction and potentially cure depth. In a test run, the UV-light was switched on manually and a timer was used to indicate when the UV-light needed to be turned off. Afterwards, uncured propellant or photopolymer was carefully removed from the cured disk that remained. The cure depth of each sample was measured at the center with calipers, although it should be noted that some of the photopolymer samples cured into a slight dome shape. This could be due to the fact that during the curing process, the cured section was not constrained well by the uncured section, so it was easier for slight warping to occur. The propellant samples cured flat and smooth (despite some slight surface roughness on the bottom surface from the particles) likely because the uncured propellant region was rigid.

4.4 Effect of UV-Parameters on Photopolymer the Cure Depth

Photopolymer samples that were cured at higher intensities (~20 mW/cm^2) were stiff, while samples that were cured at lower intensities (~1 mW/cm^2) were flexible. The difference in physcial characteristics is largely based on the degree of reaction, which is related to the amount of heat released during curing as seen in Figure 4-2. Slow polymerization is indicated by a slow increase in temperature, whereas fast polymerization is indicated by a rapid increase in temperature. Low intensities slowly heat up the polymer and the high intensities rapidly set the polymer into place. At low intensities, the peak temperature is not reached in less than 15 s, whereas the peak temperature is reached in far less than 15 s at high intensities. It was difficult to isolate the effect of intensity and wavelength since the beam area changed slightly, but it appears that the intensity has a much more pronounced effect on the heating profile in the photopolymer than the wavelength.

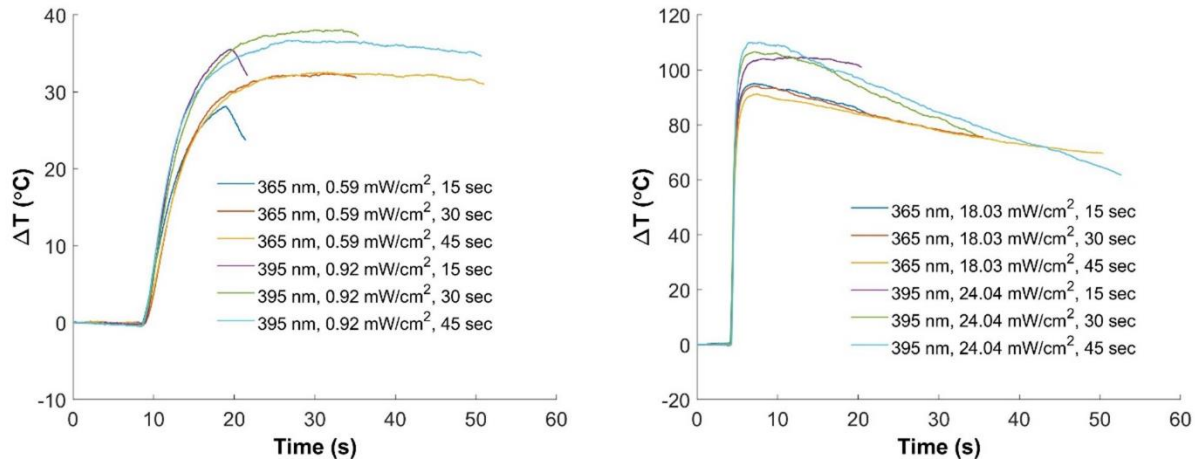

Figure 4-2. The reaction temperature traces of the photopolymers normalized with respect to ambient temperature. (Left) The low intensity cases displayed asymptotic behavior, whereas (right) the high intensity cases showed decay after reaching a peak temperature at a fast rate [45].

In order to quanitfy the speed of curing, the diameter growth rate was measured since IR cannot be used to measure the increase in cure depth over time. When the UV-light was activated, an initial beam area would appear and then grow as seen in Figure 4-3. The IR video was analyzed in ImageJ and the edge of the diameter was determined to be the red pixels based on comparison to the measured final diameter of the sample with calipers. It was found that at high intensities, the diameter stopped growing when the thermal peak was reached. However, the diameter of low intensity cases continued to grow slowly even after the asymptotic peak temperature was reached. To improve consistency in the measurement of the diameter growth rate, measurement was only considered from when the light was turned on until the thermal peak or the beginnning of the asymptote was reached. Table 4-3 shows the degree of customization in the diameter growth rate and maximum temperature by varying the wavelength and intensity.

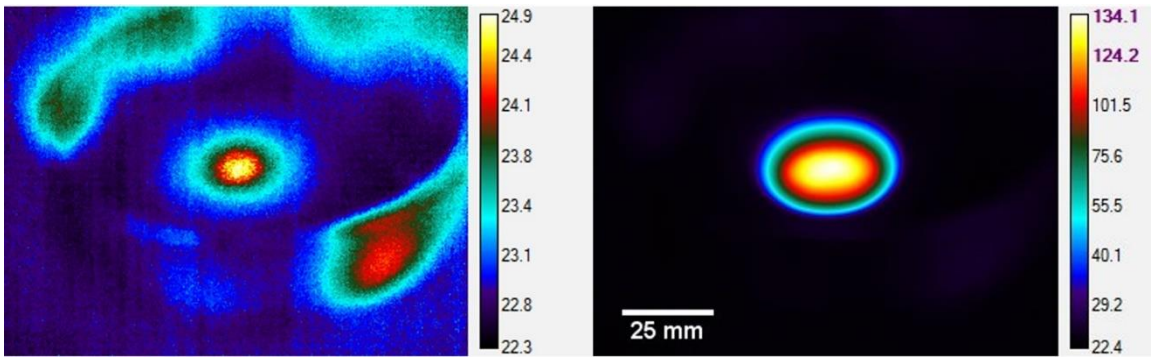

Figure 4-3. Sample IR images used to determine diameter growth rate. (Left) The first frame was selected when the photopolymer began to react and (right) the final frame corresponds to the absolute peak temperature on the thermal trace. The edge of the photopolymer is denoted by a red color and the scale bar is the temperature reported in degrees Celsius [45].

Table 4-3. The UV-cure characteristics of a 50 wt.% acrylate, 49 wt.% HDDA, and 1 wt.% BAPO photo-polymer. The exposure time was maintained at 45 s [45].

Wavelength (nm)	**Measured Intensity (mW/cm^2)**	**Diameter Growth Rate (mm/s)**	**Time to Max ΔT (s)**	**Max ΔT (°C)**
365	0.59	0.59	20.6	32.3
365	18.03	4.30	3.26	90.6
395	0.92	0.84	17.7	37
395	24.04	4.92	2.9	109.2

The values of the photopolymer cure depth are shown in Figure 4-4. Note that in the curve at a wavelength of 395 nm and intensity of 24.04 mW/cm^2, the cure depth at 30 s and 45 s actually reached the bottom of the petri dish. As mentioned before, the aim was to have an even layer of photopolymer that was ~2 mm deep and it was unexpected that the photopolymer would cure deeper than that. However, it is clear that under certain conditions, the photopolymer can cure deeper than 2 mm and it is currently unknown what the upper cure depth limits are at those conditions. At similar lower intensities, the cure depths are effectively the same for both wavelengths, so it is believed that the mismatch in the wavelength curves at high intensities (~ 6 mW/cm^2 difference) is the driving factor rather than wavelength itself. The difference in intensity is largely because although the beam areas measured before each test were the same, the power between the lights with the different wavelengths was very different, especially at the highest setting. Therefore, future tests placed emphasis on matching the intensity rather than the beam area in order to make it easier to isolate the effect of wavelength and intensity.

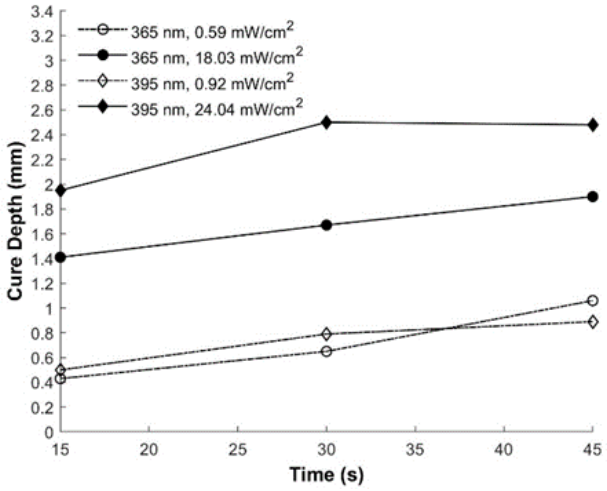

Figure 4-4. The cure depth of the 50 wt.% acrylate, 49 wt.% HDDA, and 1 wt.% BAPO photopolymer plotted as a function of exposure time, wavelength, and intensity [45].

4.5 Effect of UV-Parameters and Aluminum Content on the Propellant Cure Depth

With more understanding of how the photopolymer cures on its own, the next phase of this study was to observe the curing behavior with the addition of energetic materials such as AP and Al. Particles that reinforce photopolymers can dissipate heat, so there is less of a threat of inadvertent ignition with a higher solids loading. In general, the presence of AP particles led to deeper cure depths than those seen with the pure photopolymer in Figure 4-4. Part of this can be attributed to AP crystals scattering UV-light deeper into the mixture and the uncertainty in measurement due to rough bottom surfaces.

As seen in Figure 4-5, a higher Al content decreases the cure depth. At noted previously with the photopolymer results, it appears that wavelength does not have a significant effect on the cure depth of propellants cured at low intensities. The data at high intensities is harder to understand. Extra data points at 395 nm, 16.88 mW/cm^2 and 365 nm, 24.24 mW/cm^2 conditions were obtained to remove the mismatch in the intensity so that the effect of wavelength could be deciphered. It was surprising that the 365 and 395 nm curves at an intensity of 17 mW/cm^2 diverged significantly while the 365 and 395 nm curves at an intensity of about 23 mW/cm^2 did not. The trend of the 17 mW/cm^2 intensity propellant data, where wavelength seems to have a large effect on cure depth, is very different than the consistency seen between the 23 mW/cm^2 propellant data and the photopolymer data, where the effect of wavelength seems minimal.

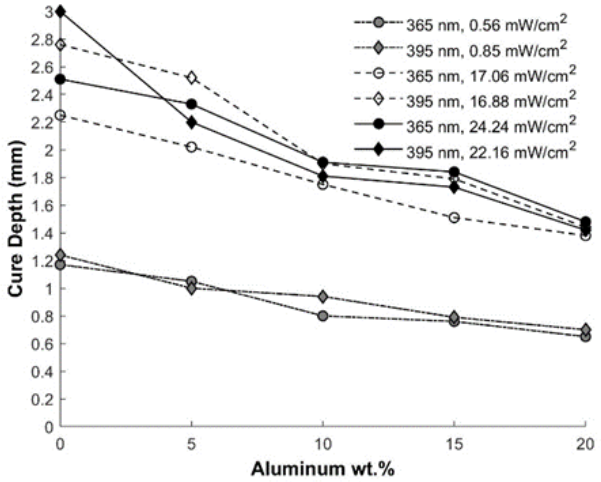

Figure 4-5. The cure depth of a propellant with 85 wt.% solids loading plotted as a function of aluminum content, wavelength, and intensity. The exposure time was 45 s [45].

Since the cure depth data alone was difficult to interpret, the normalized thermal traces with respect to ambient temperature were also analyzed. Figure 4-6 shows the thermal traces as a function of Al content for each set of curing conditions (wavelength and intensity). Some of the traces have sections where sampling skips a few frames [the 0% curve in Figure 4-6(c), the 5% and 20% curves in Figure 4-6(d), and the 5% curve in Figure 4-6(e)]. The initial increase in temperature seen on the 15% Al curve in Figure 4-6(d) is a bit of noise from a hand manually triggering the UV-light and is not a physical reaction. A similar effect can be seen towards the end of each low intensity trial where the light was manually turned off (there is a slight temporary increase in temperature) in Figures 4-6(d-e). The effect is also present in the high intensity data, but is much less noticeable given the magnitude of the temperature during the UV-curing reaction.

The effect of Al content on the temperature traces varies at each set of curing conditions. Figure 4-6(a) provides an example of an expected trend where an increase in Al content shifts the reaction temperature downward in relatively even increments. This trend does not hold for many of the other conditions, even though there is a consistent decrease in cure depth as a function Al content. Perhaps there were some slight differences in how the Al was dispersed in the propellant between batches. In particular, a lot of unexpected variance occurs in the propellant with 5% and 10% Al content. In addition, the photopolymer mixture in the propellant may not be as evenly mixed as expected, which could make some batches of propellant more reactive than others.

The maximum change in reaction temperature (max ΔT) is similar (< 5 °C) for the low intensity curves and varies between 10-20 °C for the high intensity curves. The max ΔT was compared to the cure depth and when the wavelength was held constant, a larger max ΔT coincided with a smaller cure depth for most cases as seen Figure 4-7. It is known that adding too much UV-energy can lead to vitrification, which leads to incomplete curing [13, 19]. In the context of this study, the degree of curing is believed to be related to the cure depth. Based on Figure 4-7(a) which only includes the 365 nm wavelength data, there is a direct relationship between the max ΔT and the cure depth for each Al content curve. There is less of a direct correlation with the 395 nm wavelength data as seen in Figure 4-7(b). BAPO is known to react to a wavelength of 365 nm, so it appears that the curing behavior is less predictable when cured at conditions slightly off the optimal wavelength.

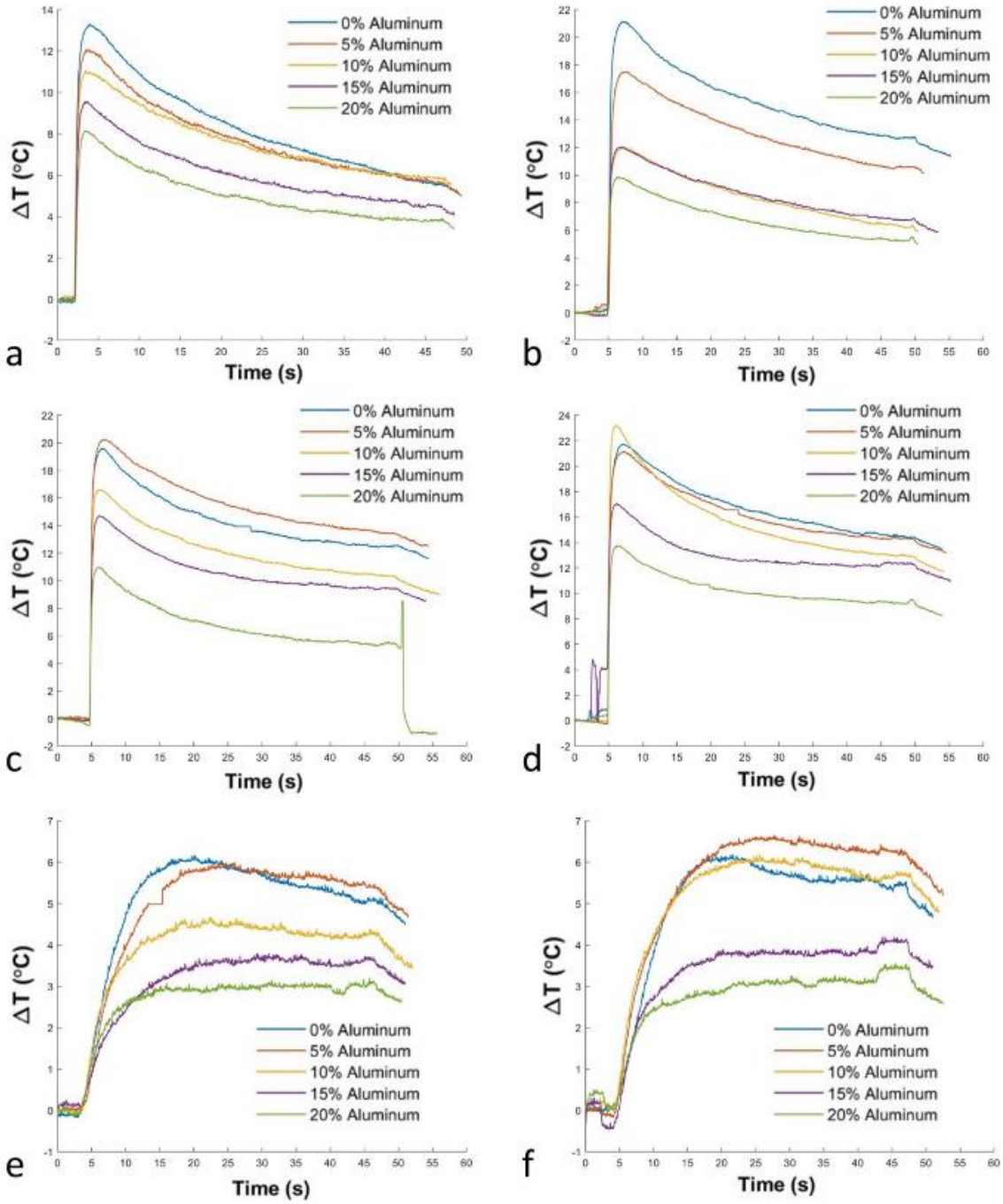

Figure 4-6. The reaction temperatures of the propellants exposed to UV-light for 45 s plotted as a function of the Al content. The temperatures are normalized with respect to the ambient temperature. The following cure conditions are (a) 365 nm, 24.24 mW/cm2 (b) 395 nm, 16.88 mW/cm^2, (c) 365 nm, 17.06 mW/cm^2, (d) 395 nm, 22.16 mW/cm^2, (e) 365 nm, 0.56 mW/cm^2, and (f) 395 nm, 0.85 mW/cm^2 [45].

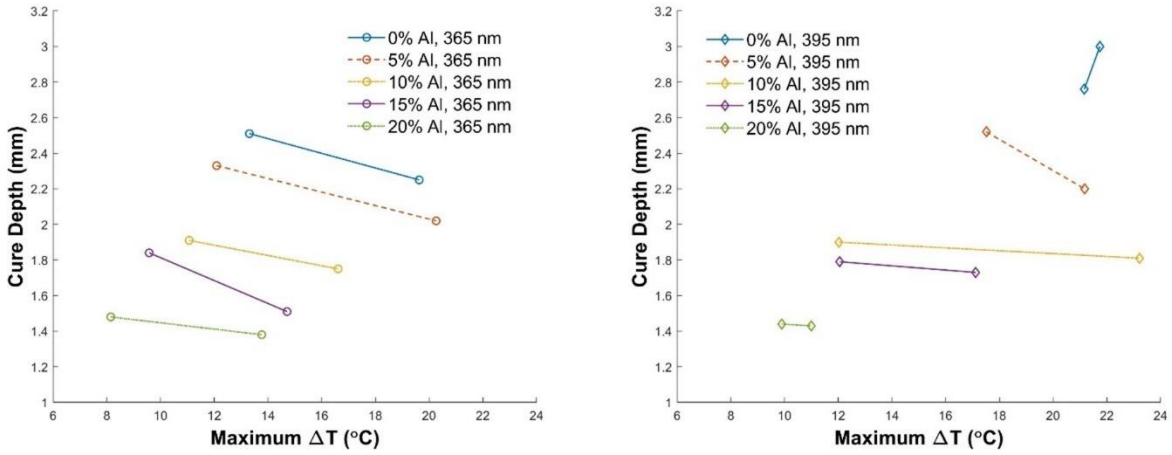

Figure 4-7. The cure depth versus the maximum change in reaction temperature (max ΔT) for a wavelength of (left) 365 nm and (right) 395 nm [45].

Simple linear curve fits and visual interpretation were not enough to isolate the effects of Al content, wavelength, and intensity on the cure depth and max ΔT, so multiple linear regression was used. A focus was placed on interpreting the high intensity data, since there is no way to know if a different controlling mechanism was occurring at low intensities that could make interpretation of the trends in the high intensity data more difficult. MATLAB was used for the analysis. The multiple linear regression model (y~1+x1+x2+x3 without interaction terms to simplify the analysis) for the cure depth data was fitted with a R-squared value of 0.893 while the max ΔT was fitted with a R-squared value of 0.538. The cure depth data satisfied the basic homoscedasticity and a normal distribution of residuals requirements. The max ΔT data satisfied those requirements to a lesser degree. The curve fit p-values in Table 4-4 show that Al content and wavelength contribute to the cure depth, while the max ΔT is only influenced by the Al content. The cure depth data and max ΔT data show different responses to UV-curing parameters, even though they are intuitively related. Although it is not fully understood how they relate, future methods that involve volume or surface area calculations will likely provide more insight. In addition, it would be important to obtain several cured samples at the same UV-curing conditions in order to determine the variance in the data.

Table 4-4. Multiple linear regression model (fitted with MATLAB) of the cure depth and the maximum change in reaction temperature data represented as a function of the aluminum content, wavelength, and intensity. The analysis only includes the high intensity (>15 mW/cm^2) data [45].

	Cure Depth Fit		**Max ΔT Fit**	
Variable	**Coefficient**	**P-value**	**Coefficient**	**P-value**
Intercept	0.036	0.972	-8.74	0.685
Aluminum Content	-0.059	4.93e-09	-0.413	0.002
Wavelength	0.006	0.032	0.086	0.119
Intensity	0.019	0.144	-0.223	0.393

For example, it would be useful to calculate the total heat required to obtain a polymerized sample with a certain cure depth and cure diameter. However, the system of interest is growing and does not have a constant mass, so the typical heat equation,

$$Q = m * cp * \int dT, \tag{3}$$

model (Q is the heat release, m is the mass, cp is the specific heat capacity, and dT is the change in temperature) will not accurately describe the total heat needed for this process. However, if one simply integrates the temperature, a trend can be seen in the data, although the integral of temperature on its own does not have a physical meaning. An example can be seen in Figure 4.8, which represents the photopolymer data from Section 4.4. The integral of temperature was obtained by calculating the area under the curves with rectangular approximations between each set of data points. This initial analysis points to a likely nonlinear relationship between thermal energy and cure depth.

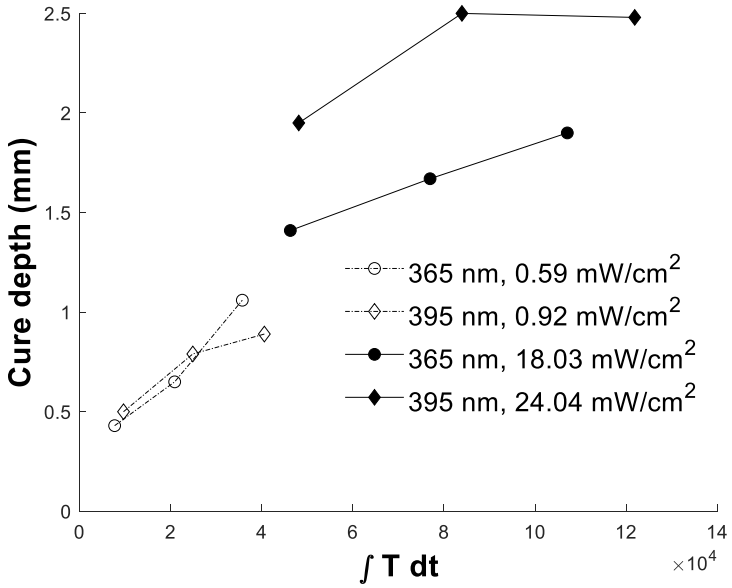

Figure 4-8. Relationship between cure depth and integrated temperature for the photopolymer data in Section 4.4.

To compare the sole effect of Al, a mixture of 20 wt.% Al and 80 wt.% photopolymer was cured with the UV-light for 45 s. One sample was cured with a wavelength of 365 nm and intensity of 17.06 mW/cm^2, while the other sample was cured with a wavelength of 395 nm and an intensity of 22.16 mW/cm^2 to replicate previously used curing conditions as closely as possible. Table 4-5 shows that Al only mixtures had a 30.0% (365 nm case) and 31.0% (395 nm case) smaller cure depth than pure photopolymer samples. The cure depth of propellant with the 20% Al content was 27.4% (365 nm case) and 42.7% (395 nm case) less than the cure depth of the pure photopolymer. At 365 nm, the addition of AP does not seem to further reduce the cure depth beyond the value of the 20% Al mixture. At 395 nm, the addition of AP seems to slightly reduce the cure depth further from the 20% Al content mixture. On its own, Al seem to be the main contributor to the reduction in the cure depth rather than the presence of a significant amount of AP in the mixture.

Table 4-5. The effect of 20 wt.% neat Al and 20% aluminized propellant (85 wt.% solids loading) on the cure depth. The exposure time maintained at 45 s [45].

Mixture (wt.%)	Wavelength (nm)	Measured Intensity (mW/cm^2)	Cure Depth (mm)
100 Polymer	365	18.03	1.90
100 Polymer	395	24.04	2.48
20 Al/80 Polymer	365	17.06	1.33
20 Al/80 Polymer	395	22.16	1.71
20 Al/65 AP/15 Polymer	365	17.06	1.38
20 Al/65 AP/15 Polymer	395	22.16	1.42

4.6 UV-Cured Propellant Properties

Most of the results in this study involved curing one layer, but in the reality of additive manufacturing, the properties of UV-cured layers will be critical. Therefore, micro-CT of a propellant structure with 4 cured layers was investigated and can be seen in Figure 4-9. Each layer was pressed to a thickness of about 1 mm and a radius of about 30 mm and cured for 45 s (395 nm, 23.72 mW/cm^2). Based on the propellant cure depths in Figure 4-5, each 1 mm layer would be completely cured. The layered propellant structure had a thickness of 3.88 mm and a diameter of 25.37 mm. The same micro-CT system that was used in Section 3.3 was operated at 100 kV and a resolution of 16.5 μm. No cracks at the center (where the UV-light energy is concentrated) nor binder separation from the particles were visible. The layered structures tested were difficult to cut with a razor blade and preserved their shape well, which is a promising result for 3D printing resilient propellant grains in the future. It is noted that an important area of future research is the study of layer-to-layer adhesion to determine if the interfaces are weaker than the cured photopolymer matrix itself.

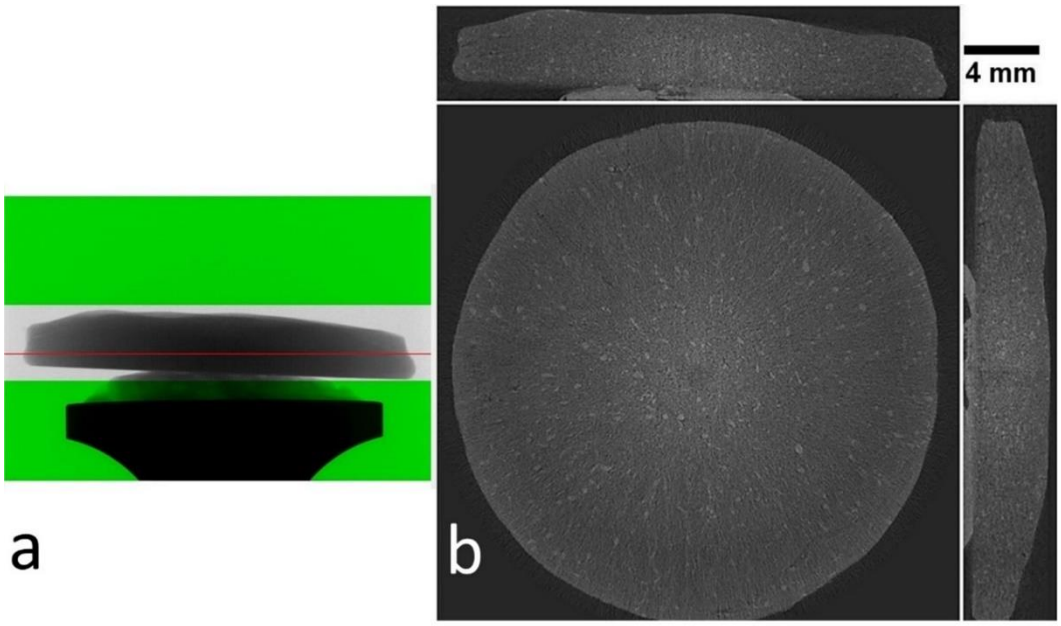

Figure 4-9. An image obtained via micro-CT of 4 cured layers of propellant (85 wt.% solids loading) with 15% Al content. (a) The red line represents the Z cross-section. (B) the X, Y, and Z planes are shown from the middle of the sample [45]. The figure has been modified from the published (black and white) version.

Lastly, the cured disks where burned in atmospheric conditions. In Figure 4-10, the combustion of 0%, 5%, 10%, 15% and 20% aluminized propellants can be seen. There were no visible cracks on the surface from the curing process or from thermal conduction beneath the propellant surface during combustion. Another future area of study is investigating the viability of multilayer UV-cured propellant at high pressure as a function of UV-curing parameters. Figure 4-11 shows a demonstration of a 3D printed UV-cured ring with a 0.7 mm nozzle. The propellant mixture is the same as the non-aluminized formulation used in this chapter. A parsing code written in Python was used to add UV-curing commands. The code can control the time of cure, the overlap of the UV-beam in the curing path, and the frequency of cure (i.e. cures every specified number of layers). A future research area would be to manufacture complex grain geometries with the presented photopolymer and with a VAP system capable of controlled UV-curing.

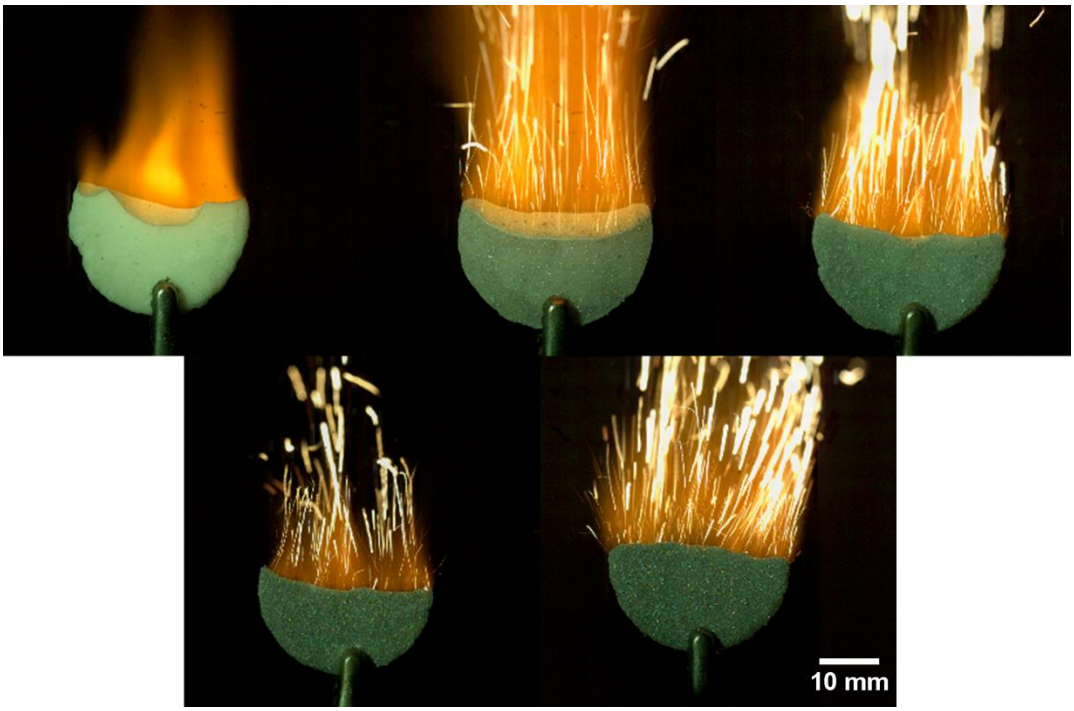

Figure 4-10. Combustion of UV-cured propellant at 1 atm. From top left to bottom right, the propellants have 0 wt.% Al, 5 wt.% Al, 10 wt.% Al, 15 wt.% Al, and 20 wt.% Al [45].

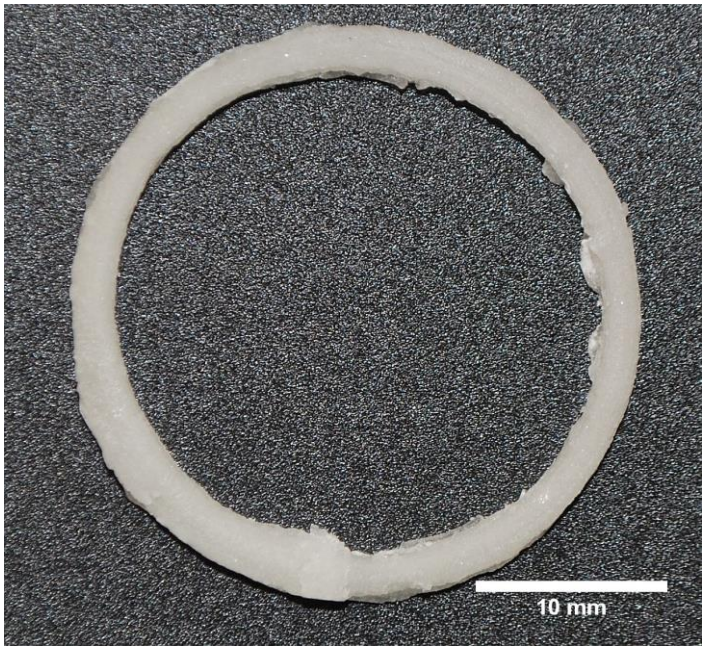

Figure 4-11. Additively manufactured ring that was UV-cured using a modified VAP system [54]. The ring was cured every few layers.

4.7 Conclusions

Since there were no standards available to determine the effectiveness of photopolymers in propellant mixtures with opaque additives, this study identified potential methods to analyze the effect of parameters such as wavelength, intensity, and aluminum content on the cure depth of propellant. In general, it was difficult to isolate the effect of wavelength and intensity due to the error induced from the test method. For all intents and purposes, the intensity was the most important factor in cure depth of the photopolymer. As expected, increasing Al content in the propellant decreased the cure depth regardless of the wavelength and intensity used. However, the cure depth varied from 1 - 3 mm, which is more than enough for what is required for 3D printing with VAP. More work is needed to fully isolate the effects of wavelength, intensity, and Al content on the propellant cure depth, even though it was found that higher reaction temperatures (max ΔT) lowered the cure depth for a given wavelength. The study also clearly showed that Al had the largest effect on the decrease in the cure depth (~30% reduction) and that the solids loading of AP in a propellant mixture had little effect. X-ray tomography showed no interfaces nor binder separation from particles in layered aluminized (15%) propellant. Lastly, a ring of propellant was additively manufactured successfully on a new VAP system capable of controlled UV-curing [54] and cured samples were burned at atmospheric conditions.

5. MODELING OF LAYERED PROPELLANT COMBUSTION

5.1 Motivation

As previously noted in Section 2.3, there is very little literature on the combustion of layered gun propellants and there is none on layered composite rocket propellant that the author could find in open literature. Shortly before it was possible to use VAP to layer propellant, it was decided to computationally explore layered propellant combustion using a code called Rocfire and a layering algorithm developed by Dr. Brian Bojko at China Lake. The modeling of layered AP propellant presented in this chapter is the first study of its kind in known open literature. The material in this chapter is being prepared for publication.

5.2 Rocfire Parameters

Rocfire is capable of modeling the deflagration of heterogeneous materials as described in Section 2.4. A random packing algorithm, Rocpack, is used to pack spheres of AP into a periodic cube to replicate the distribution of AP crystals in a real-world propellant. The volume between spheres is the volume of the HTPB binder. The simulated propellant pack is burned in Rocfire to yield burning rate data. The X-Z plane represents the surface of the propellant pack that is exposed to the flame and the pack burns in the Y direction. In the gas-phase, the top boundary is considered open, while the sides of the propellant pack are periodic boundaries where information needed on the X+ direction is taken from the interior nodes on the X- direction (and vice-versa). The same applies for the Z direction. The mass loss rate at the surface is determined using an Arrhenius rate law as a function of the surface temperature for AP and HTPB separately. The temperature of the surface is assumed to be in thermal equilibrium with the gas-phase, and heat conduction is modeled within the solid-phase. Fresh propellant is fed in from the bottom of the solid-phase model at an ambient temperature of 300 K. A four step kinetic mechanism is used to model the combustion of AP/HTPB, which considers the AP monopropellant flame, the primary flame between AP and HTPB, a homogeneous dirty binder flame that accounts for fine crystals, and a final diffusion flame ~200 μm above the surface (refer to [55] for more details about the mechanism adopted here). Grid compression is used to increase the resolution of the propellant near the surface, and the interface is mapped to an η-coordinate surface function (which relates the surface location to

the Y-coordinate) to increase computational efficiency [38]. Several recommendations for parameters that result in convergence in Rocfire were followed [56, 57].

5.3 Propellant Selection and Layering Effects

To model the combustion of layered propellant, single propellant packs were created and then a layering code was used to slice each single pack by the number of specified layers (3 in this study) and add them together. Since each single propellant pack has its own packing fraction, each slice could technically have a different packing fraction. The difference in packing fraction from the original single pack to the layered pack would likely get worse as thinner slices are taken from a single pack, so care was taken when picking a minimum layer thickness (~500 μm). Once the slices were created, precedence was given to the most current slice (i.e. any AP particles that overlapped between layers were deleted from the previous slice). This likely has a small effect on the total packing fraction of the layered propellant, except when multiple large AP particles are removed. Once all of the slices were stacked, the packing fraction was set based on the slice of the first single pack and was used to define the stoichiometry needed by the simplified kinetics model. Overall, this assumption is reasonable if each single pack has a similar packing fraction. This assumption can be relaxed by summing all of the AP particles in the layered propellant to determine the effective packing fraction. Note that the packing fraction is the number of spheres packed in a binder volume and is not the same as volume loading in a propellant mixture. This layering approach causes some compositional variations at the interface that may affect combustion, but experimental configurations may result in interfacial variations as well, especially if adhesives are used.

Table 5-1 shows the test matrix of single propellant packs as well as layered propellant packs in vertical orientations (level-set in the X direction) and horizontal orientations (level-set in the Y direction). The particle size distributions involved in the propellants are monomodal 20 μm, monomodal 90 μm, bimodal 90 μm /130 μm with a 1:1 CFR, and monomodal 130 μm AP. The slow burning propellant in this study is made of monomodal 130 μm AP particles, while the other three particle size distributions were used to make faster burning propellant formulations for the middle layer. The particle size distributions for the 20 μm and 130 μm AP were obtained from experimental data in Yan et al. [43], while the 90 μm particle size distribution was a lognormal distribution from Miller et al. [42]. These particle sizes were chosen since they would be

compatible with VAP [37], allowing the results of this paper to be relevant to experimental tests in the future. The 130 μm AP is the same as the 60-130 μm AP reported in previous Sections (3.2 and 4.2). The 20 μm AP packing fraction is low because the cutoff diameter of AP for the dirty binder assumption (particles below the cutoff binder are assumed to be homogenized within the binder) was 10 μm. Each formulation had a solids loading of 75 wt.% (58.6 vol.%). Since most of the formulations were monomodal, it was difficult to computationally pack more particles above that limit. The layered propellant was either packed into a vertical orientation (the layers burn perpendicular to the flame) or a horizontal orientation (the layers burn parallel to the flame). It should be noted that there is a negligible directional dependence on the number of particles packed in a layered propellant based on packing orientation (X or Y).

Table 5-1. Single and layered propellant pack configurations in horizontal and vertical orientations.

Propellant	# of Layers	Orientation (X/Y)	Domain in μm (X and Z)	# of Particles	Packing Fraction
20 μm	1	N/A	1612 x 1612	105700	0.347
90 μm	1	N/A	1612 x 1612	328922	0.490
90 μm/130 μm (CF 1:1)	1	N/A	1612 x 1612	170344	0.530
130 μm	1	N/A	1612 x 1612	11762	0.566
130 μm| 20 μm| 130 μm	3	X	537 - 537 - 537	41932	0.566
130 μm| 90 μm| 130 μm	3	X	537 - 537 - 537	115172	0.566
130 μm| 90 μm/130 μm (CF 1:1)| 130 μm	3	X	537 - 537 - 537	63621	0.566
130 μm| 20 μm| 130 μm	3	Y	537 - 537 - 537	41664	0.566
130 μm| 90 μm| 130 μm	3	Y	537 - 537 - 537	114382	0.566
130 μm| 90 μm/130 μm (CF 1:1)| 130 μm	3	Y	537 - 537 - 537	63394	0.566

Figure 5-1 shows the X-Z cross-section 120 μm below the top surface of vertically oriented layers at t=0 s in Rocfire. Red represents the AP particles, while blue represents the dirty HTPB binder. The figures are level-set descriptions in Rocfire of AP particles in a discretized domain on a Cartesian mesh, which results in a slightly pixelated effect for the mesh used in this study. It is clear that the layering code was successfully able to layer propellants at small thicknesses (~500 μm) without creating significant AP particle deficient regions between layers. However, we note there is a slight binder rich region at the interface of the left slice and the middle slice compared to the interface of the right slice and the middle slice. This is because the layering preference was given to the recent slice, while particles from the previous slice were deleted (the layering order was from left to right).

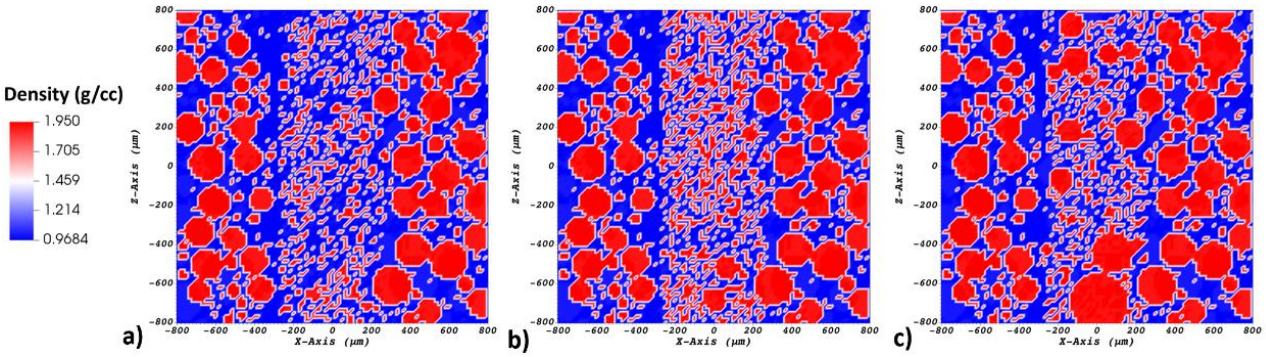

Figure 5-1. X-Z cross-section 120 μm below the surface of vertically layered (a) 130 μm| 20 μm| 130 μm, (b) 130 μm| 90 μm| 130 μm, and (c) 130 μm| 90 μm/130 μm (CFR1:1)| 130 μm propellant in Rocfire at t=0 s.

5.4 Combustion Dynamics of Layered Propellant

Typically, the burning rate of single propellant packs in Rocfire is averaged over time to normalize local oscillations. For layered propellant, it is important to consider the time-varying burning rates, which are seen in Figure 5-2 at a pressure of 10.34 MPa. The initial rise (until ~0.02 s) is a due to the initial conditions of the simulation (essentially an ignition transient) and the propellant packs are then burned twice in the Y direction, resulting in a periodic burning profile thereafter. It is not surprising that in the vertical orientation (flame perpendicular to the layers) in Figure 5-2(a), the burning rate accelerates over time due to the increase in burning surface area, as the more reactive inner layer propagates faster than the slow outer layers. The acceleration of the 20 μm, 90 μm, and 90 μm/130 μm (CFR1:1) layered propellant burning rates occurs at a rate of 1.52 cm/s^2 (R-squared=0.804), 1.55 cm/s^2 (R-squared=0.764), and 1.30 cm/s^2 (R-squared=0.725) respectively. The acceleration was calculated with data taken from t=0.03 s until the end of the burning rate profile to avoid the inclusion of initial transient data. The 20 μm and 90 μm layered propellants accelerate similarly while the bimodal mix is slightly slower. The R-squared fit decreases with increasing particle size because larger particles cause more surface variation at a low solids loading and therefore more oscillation in the time-varying burning rate. This effect can be seen in the burning rate of single propellant packs (i.e. the burning rate oscillation decreases with particle size).

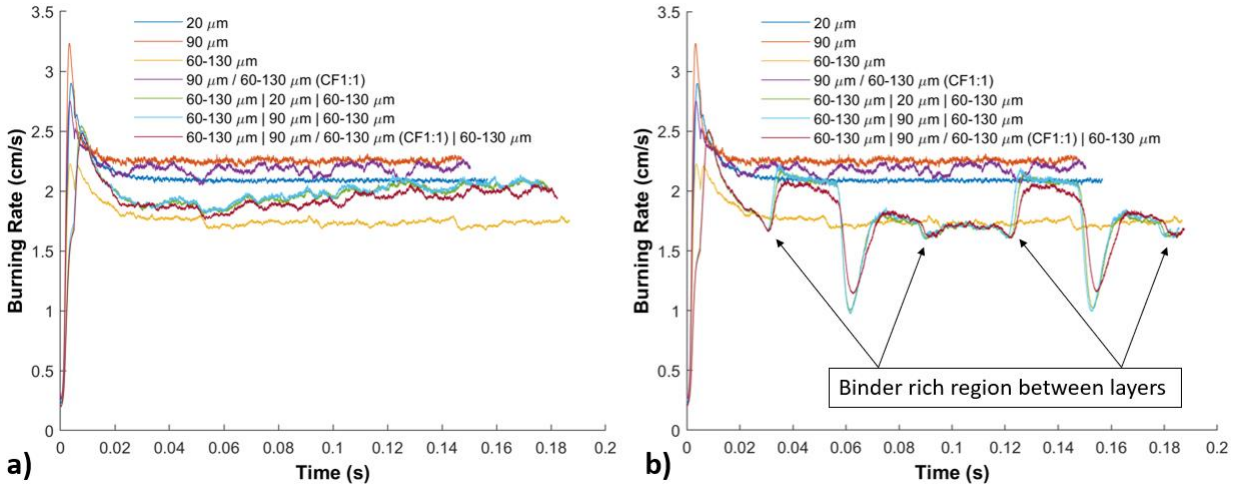

Figure 5-2. Burning rate profiles of single pack and layered propellants burned through 2-3 periods at 10.43 MPa in (a) vertical and (b) horizontal orientations.

An example of the developing burning surface can be seen in Figure 5-3 where after a short time, a divot with a depth of ~0.4 mm develops, which is a consequence of increasing burning surface area. Figure 5-4 shows the surface contours of the layered propellant as it regresses in order to illustrate the progression of the burning surface profile. Although the burning rate of the layered propellant in the vertical orientation does not level out at the speed of the faster layer in these simulations, the surface contours show that past 130 ms, the burning surface contours stays the same, so it is assumed that the propellant surfaces are reaching an equilibrium point and the burning rate would do the same if the simulation ran longer. The layered propellant surface contours develop in a similar way for each case. A practical consideration is that the inclusion of a fast burning layer between slower baseline propellant layers will cause the surface area to adjust to increase the effective burning rate, assuming that the layer thickness is large enough. Thus, only some of the propellant needs to have a high burning rate to produce an overall higher effective burning rate.

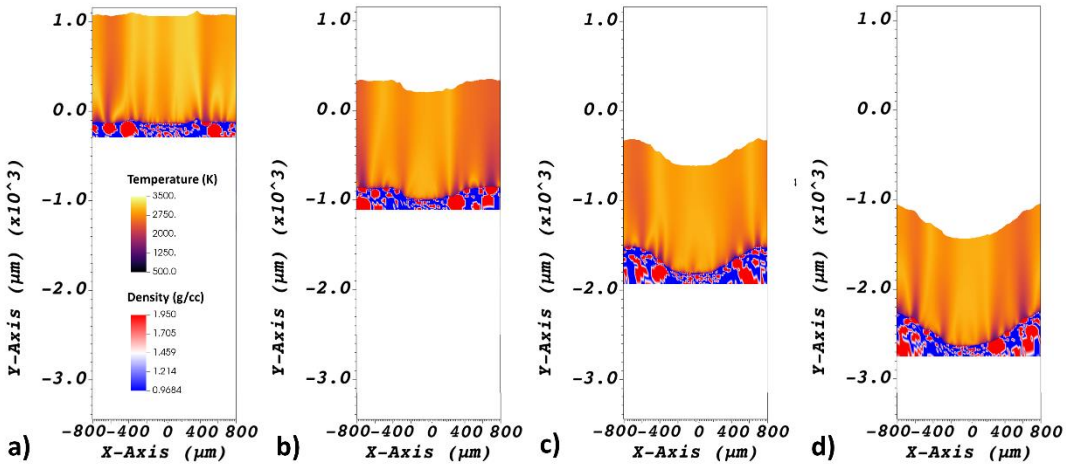

Figure 5-3. Burning surface profile of 130 µm | 20 µm| 130 µm vertically layered propellant burning in the Y direction at 10.34 MPa. The cross-section is shown halfway into the Z direction and there are 40 ms between each frame. The propellant surface is (a) flat at ignition and then (b-c) the burning surface area increases until it (d) becomes fully developed.

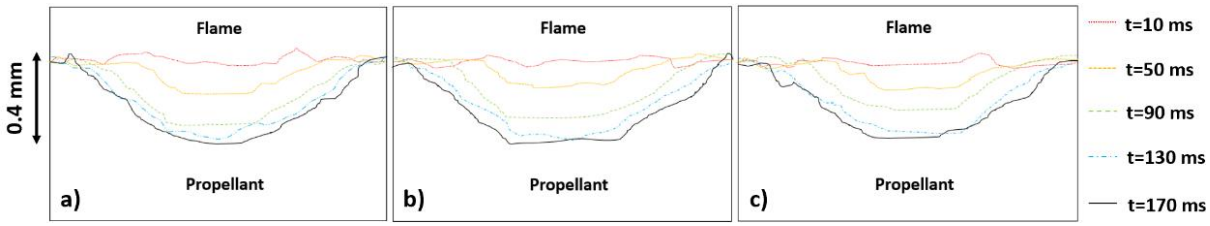

Figure 5-4. Surface contours of (a) 130 µm| 20 µm| 130 µm, (b) 130 µm| 90 µm| 130 µm, and (c) 130 µm| 90 µm/130 µm (CFR1:1)| 130 µm vertically layered propellant over time at 10.34 MPa.

The burning rate profiles of the horizontally oriented (flame parallel to the layers) propellant in Figure 5-2(b) show very different behaviors between the transition from slow to fast burning layers and vice-versa. The acceleration from the slow layer to the fast layer results in slight overshoot for the 20 µm layered propellant case, but then the burning rate matches the speed of the fast layer shortly thereafter. The burning rate of the other two layered propellant formulations do not quite reach the value of the respective fast burning layer. However, the transition from the fast to slow layer results in a dramatic decrease in burning rate, which severely undershoots the speed of the slowest layer in all of the simulated cases. Then, the propellant recovers after some time.

Figure 5-5 shows how the transition from fast to slow layers occurs: a) the fast layer is burning flat and approaches the slow layer, b) the slow layer experiences surface unsteadiness and

the flame structure dramatically changes, and c) the slow layer recovers in speed and the surface flattens out. In Figure 5-2(b), the addition of large 130 µm particles in the bimodal layered propellant has a slight damping effect on the transition in burning rate between layers. However, it appears that the fine AP (50% 90 µm) is dominating the combustion behavior and is creating similar combustion dynamics to the 20 µm and 90 µm layered configurations.

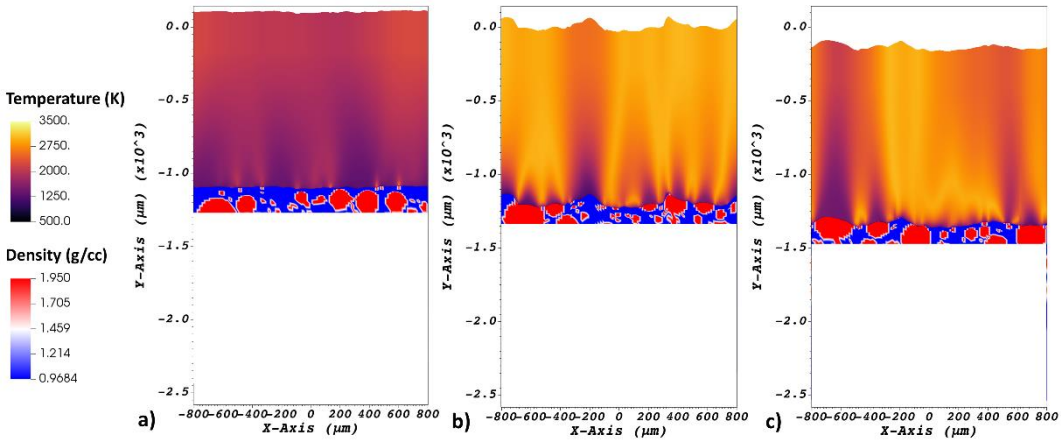

Figure 5-5. Burning surface profile of 130 µm | 20 µm| 130 µm horizontally layered propellant burning in the Y direction during the transition from fast to slow layers. The cross-section is shown halfway into the Z direction and there are 8 ms between each frame. The surface is (a) flat while burning through the 20 µm layer, (b) becomes unsteady at the transition to the 130 µm layer, and then (c) recovers while becoming relatively flat again.

The average burning rates for the 20 µm, 90 µm, and 90 µm/130 µm (CFR1:1) single propellant packs are 2.09 cm/s, 2.25 cm/s, and 2.18 cm/s respectively for the fast layers and 1.74 cm/s for the slow (130 µm) layer. It is noted that experiments show that as AP particle size decreases, the burning rate increases, so it was necessary to find an explanation for the low burning rate of the 20 µm AP. In a previous study, one of the key parameters for the combustion of fine propellants is cutoff diameter [55]. In order to obtain more accurate burning rates of fine propellant at high pressure, it was found that the cutoff diameter should be around 1 µm rather 10 µm, which was used in this study. Therefore, we note that the burning rate of the 20 µm AP is not representative of the actual experimental value. However, the simulated propellant in this study still represents a fast burning propellant with a small particle size that can be used to study the combustion dynamics of layered propellant.

To quantify the responsiveness of the dynamic burning rate, data from 0.03079 s to 0.05571 s was used to analyze the transition from the slow to fast layer and data from 0.05571 s to 0.08706

s was used to analyze the fast to slow layer. Table 5-2 summarizes the overshoot (if present) and peaks. It can be seen that only the 20 µm layered propellant exceeded the speed of the 20 µm single propellant pack. The peak burning rate of the 90 µm layered propellant falls 1.3% below the average burning rate of the 90 µm single propellant, while the peak burning rate of the bimodal layered propellant falls 3.7% below the average bimodal single propellant burning rate. The overshoot from the fast to slow layer of the 20 µm layered propellant is about 4 times larger than from the slow to fast layer. The presence of 50% 130 µm AP in the bimodal layered propellant dampens the overshoot by a factor of 2 compared to the burning rate overshoot of the 90 µm layered propellant in the fast to slow direction. There seems to be some effect of the binder rich interface between layers due to the layering code which is highlighted in Figure 5-2(b). However, the order of magnitude of those dips is the same as the magnitude of the oscillations in the burning rate of the bimodal single propellant pack.

Table 5-2. Dynamics of the burning rate profile between horizontally oriented layers. Italicized lettering refers to the transition from slow to fast layers while unitalicized lettering refers to the transition from fast to slow layers.

Transition direction	Overshoot %	Peak (cm/s)
130 µm to 20 µm	*4.72*	*2.19*
20 µm to 130 µm	19.8	1.00
130 µm to 90 µm	*N/A*	*2.22*
90 µm to 130 µm	20.5	0.97
130 µm to 90 µm/130 µm (CF 1:1)	*N/A*	*2.10*
90 µm/130 µm (CF 1:1) to 130 µm	11.1	1.14

One possible explanation of the transition phenomena between horizontal layers involves the thermal theory of homogeneous propellants [58] and the effect of pressure on the thermal profile in a propellant. Figure 5-6 shows the thermal profile from the fresh propellant temperature (T_∞) to the flame temperature (T_F). The slope of the profile at the interface of the propellant is much steeper for a propellant with a faster burning rate (analogous to a propellant burning at higher pressure) than for a propellant with a slower burning rate (analogous to a propellant burning at lower pressure). More thermal energy is stored in the propellant when the slope is shallower, so it is relatively easy to transition from a slow burning layer to a fast burning one due to slight preheating into the propellant. In the other direction, there is a thermal energy deficit in the propellant, so the transition from fast to slow layers almost results in extinction/quenching. After a short time, the slow layer has burned long enough to store more thermal energy deeper into the

propellant and that is when the burning rate recovers. We hypothesize that given a more abrupt change, extinguishment could occur.

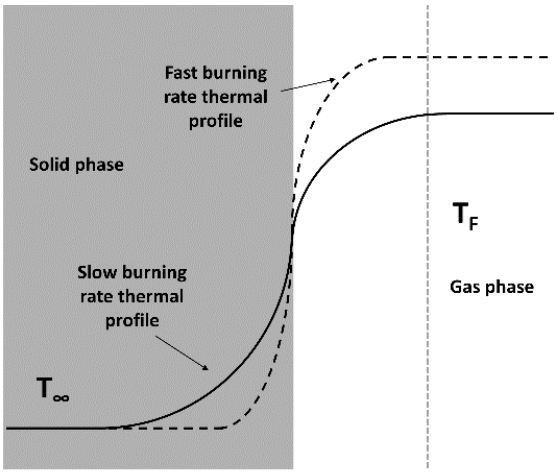

Figure 5-6. Schematic of thermal profile in homogeneous propellant for fast and slow burning propellants.

Another effect could be due to how particles are distributed within the binder in each layer. When transitioning from a slow to a fast layer, the more evenly dispersed fine particles can ignite more easily and therefore readily accelerate the burning rate. In the order direction, the coarse particles are further apart so the particles and binder are igniting and burning locally at different rates. It then takes more time for the unsteady surface ignition of the coarse layer to burn more cohesively. This uneven ignition due to particle size would likely not be as big of an effect in propellant layers with a higher solids loading or a closer match in particle size.

In an attempt to isolate the effects, the surface area ratio (defined as the ratio of burning surface area to a planar cross-sectional area), burning rate, and the equivalence ratio (divided by 10 to fit on the plots) were analyzed. In Figures 5-7 to 5-9, there is a dramatic increase in the equivalence ratio at the transition from the fine to coarse layers, which is due to the fact that in that region, there is a very small cross-sectional area of AP since the particles are so coarse relative to the binder. This increase in the equivalence ratio drives the drop in burning rate as the surface becomes very fuel rich. As the surface regresses, the cross-sectional area of AP increases, causing the equivalence ratio to decrease as more oxidizer is consumed. As the surface regresses further, there is a large increase in the surface area ratio since locally, there are some regions that are still binder rich and other regions where the coarse AP particles are starting to burn. This large increase

in surface area contributes to the recovery in the burning rate. It is likely that a stabilizing equivalence ratio also contributes to the recovery.

This process is also applicable for explaining the transition from slow to fast layers where the region is slightly binder rich due to the removal of overlapping particles and can be summarized as follows:

1) There is a small increase in the equivalence ratio due to a slight binder rich region, causing a slight dip in the burning rate.
2) There is a decrease in the equivalence ratio as more fine AP particles are consumed.
3) There is a slight increase in the surface area, and subsequently burning rate, as fine AP particles are consumed.

Based on these observations, it appears that there are two forces that drive the combustion dynamics at the interface: equivalence ratio and particle size. As long as the equivalence ratio between two layers is different, we can expect to see a change in burning rate, so this behavior could also be seen in layered homogeneous propellants. However, a large mismatch in particle size between two layers has the ability to dramatically affect the local equivalence ratio, especially when igniting a layer with larger particles. It is potentially possible that the mismatch in particle size can change the equivalence ratio at the interface much more than simply two different homogeneous propellants could. In addition, the ignition of layers with larger particles will induce larger increases in surface area due to the local variation in burning rate between small AP cross-sections and excess binder. It is likely that as the larger particles begin to burn, both a decrease in equivalence ratio, from a fuel rich condition, and an increase in burning surface area drive the burning rate recovery process.

The layered propellant with the 20 μm AP middle layer has the largest peaks in the equivalence ratio (see Figure 5-7) while the configuration with the bimodal inner layer has the smallest peaks (see Figure 5-9), indicating that particle size plays a role. The magnitude of the peaks in the equivalence ratio correspond to the magnitude of the decrease in burning rate. One might argue that the equivalence ratio is the only driving factor in the combustion dynamics, but when looking at the same relationships between the surface area ratio, burning rate, and equivalence ratio in the vertically oriented configurations, the equivalence ratio remains effectively constant (except when starting to burn through a repeating unit cell), while the surface area ratio increases (refer to Figures 5-10 to 5-12). Therefore in the vertical configuration, the

surface area increase is the driving force behind the increase in the burning rate, so it is likely that it also plays a role in the burning rate profile of propellants burned in the horizontal configuration.

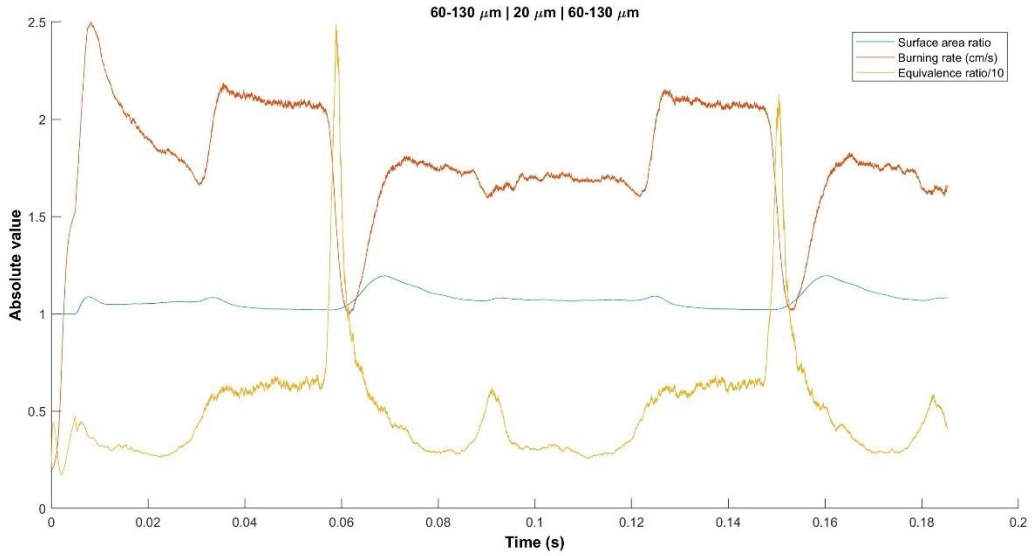

Figure 5-7. Comparison of surface area ratio, burning rate, and the equivalence ratio divided by 10 of 130 µm | 20 µm| 130 µm layered propellant burned in the horizontal orientation.

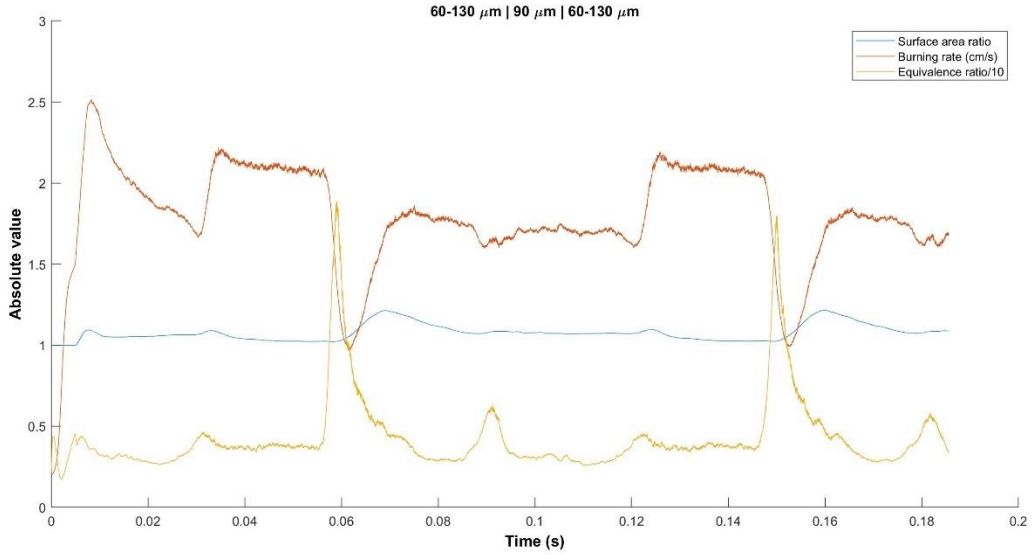

Figure 5-8. Comparison of surface area ratio, burning rate, and the equivalence ratio divided by 10 of 130 µm | 90 µm| 130 µm layered propellant burned in the horizontal orientation.

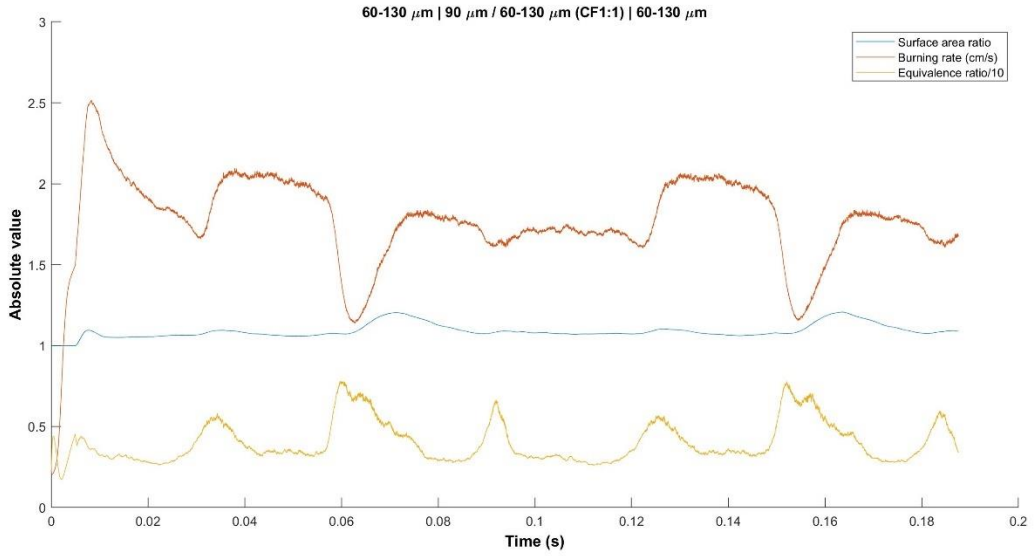

Figure 5-9. Comparison of surface area ratio, burning rate, and the equivalence ratio divided by 10 of 130 µm | 90 µm/130 µm (CFR1:1) | 130 µm layered propellant burned in the horizontal orientation.

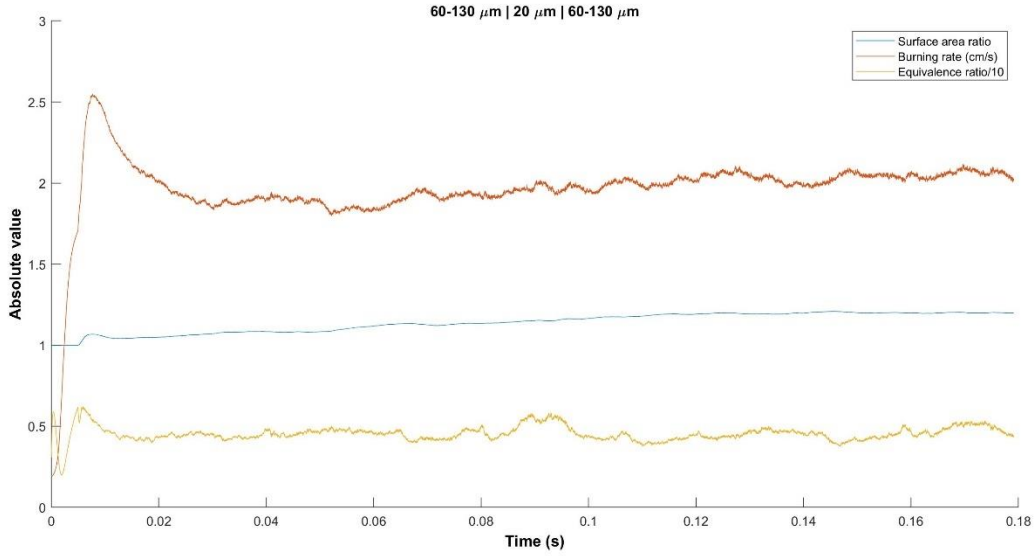

Figure 5-10. Comparison of surface area ratio, burning rate, and the equivalence ratio divided by 10 of 130 µm | 20 µm| 130 µm layered propellant burned in the vertical orientation.

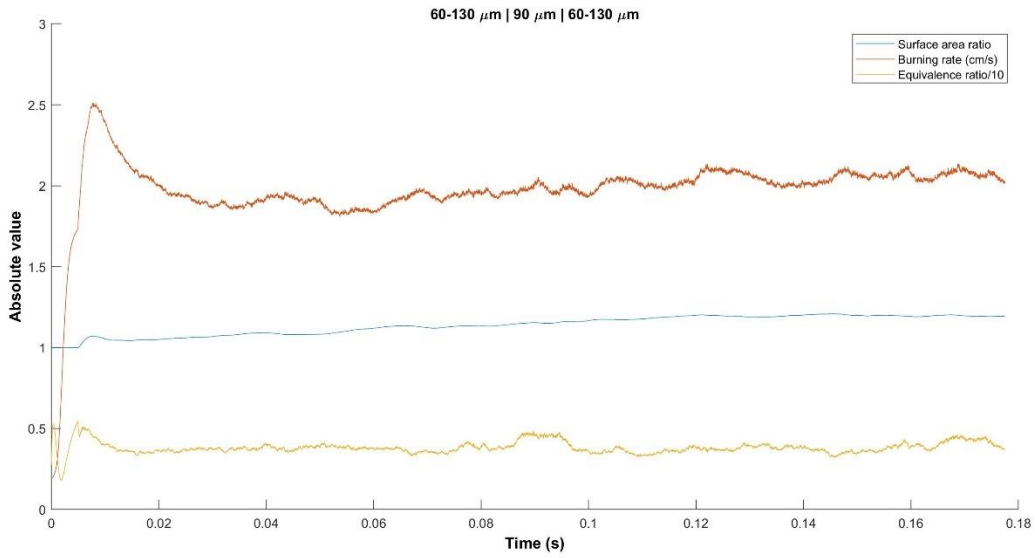

Figure 5-11. Comparison of surface area ratio, burning rate, and the equivalence ratio divided by 10 of 130 µm | 90 µm| 130 µm layered propellant burned in the vertical orientation.

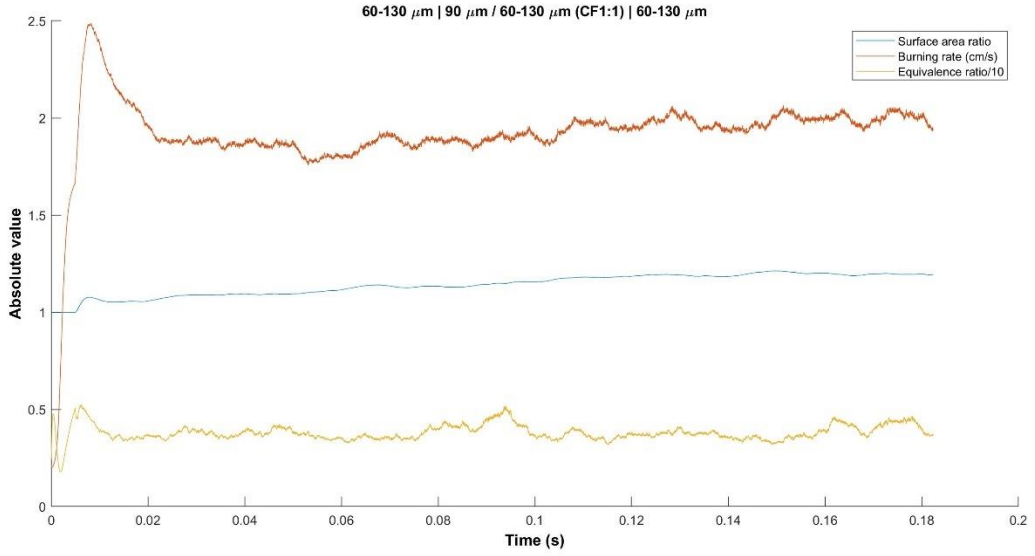

Figure 5-12. Comparison of surface area ratio, burning rate, and the equivalence ratio divided by 10 of 130 µm | 90 µm/130 µm (CFR1:1) | 130 µm layered propellant burned in the vertical orientation.

5.5 Experimental Validation

There was an attempt to experimentally validate the increase in burning surface area seen in the vertical configurations. It was thought that using VAP to deposit propellant with a low solids loading (75 wt.%) into layers of 0.5 mm with high accuracy would be too challenging. Therefore, a tape caster was used to achieve this goal. The 60-130 μm AP was sieved below 180 μm, the 90 μm AP (Firefox) was sieved below 120 μm, and the 20 μm AP was sieved below 45 μm. The propellant binder was 76.55 wt.% HTPB (Rocket Motor Components), 15.05 wt.% IDP (Rocket Motor Components), and 8.4 wt.% IPDI (Firefox). Each propellant was mixed according to previously described parameters used for HTPB propellant (see Section 3.2). After a layer was freshly mixed, the propellant was smeared onto a heated glass plate multiple times (55 °C) at a speed of 10-12 mm/s until there were no missed gaps in the deposited propellant. The height of the blade was 0.559 mm. After the first layer of propellant was deposited, it was cured in an oven overnight at 60 °C because it was not possible to smear a thin layer of fresh propellant onto unsolidified propellant accurately. The process was repeated each day until all three layers were complete. Then the propellant was removed from the plate and cut into strands. Nitrocellulose lacquer (Firefox) was used to attach nichrome wire to the top of the strands which were burned in a pressurized environment.

There were several issues with the tape cast layered propellant. The biggest issue was that the resulting strand was very thin (~1.5 mm), so it was difficult to evenly ignite the surface. In addition, the propellant would occasionally self-quench due to the heat loss to the surroundings. Lastly, there appeared to be some bonding issues between the interfaces of the strands. This phenomenon has been documented before [59] and it is noted that layering with VAP produces superior interlayer bonding. In order to experimentally validate computational studies of layered propellant in the future, it is recommended to select formulations with a higher solids loading that are viscous enough to be manufactured with VAP (i.e. bimodal/trimodal formulations) and for the computational domain of the layers to be increased from ~0.5 mm to at least 1 mm or larger.

5.6 Conclusions

In this work, small changes in propellant formulation (namely particle size) significantly altered the burning rate profile of layered propellant with 75 wt.% (58.6 vol.%) AP/HTPB mixtures

at 10.34 MPa when compared to single propellant packs. This is a profound finding because layering propellant at a fine scale (~ mm) can result in large changes in the burning behavior of the bulk material. In addition, there is a directional dependence on the orientation in which propellant is burned, which could inadvertently result in extinction or at least dynamic burning rates that significantly differ from steady burning rates. Although the layering method presented here resulted in regions between layers that were slightly more binder rich (depending on the order of layering) that affected the burning rate, those changes were no larger in magnitude than oscillations seen in the burning rate of the bimodal single propellant pack. However in experiments, interfacial effects will likely occur and attention is needed on the transition between layers. The extreme deceleration is largely explained by the coupled effects of local equivalence ratio and surface area ratio, which ultimately affect the burning rate. It is believed that a large difference in the particle size between layers at this low solids loading is responsible for driving large changes in the local equivalence ratio. The local ignition of AP particles and binder drives the change in the surface area ratio, which is exacerbated by coarse particles. This study provides some fundamental insight as to how different propellants interact at fine scales, which has not been previously studied. In addition, the fundamental mechanisms for this behavior have been identified and it will be important to explore their role in experimental studies.

5.7 Future Work

There are a few more tests that are necessary to fully strengthen the arguments made in this chapter. First, there is a question as to whether the large deceleration seen with the horizontally oriented propellant was physical or caused by the layering algorithm. One way to address this is to burn the propellant in the opposite orientation. If a large change in burning rate is still seen at the transition from the fine to the coarse layers, then it is likely that the transition is physical. In addition, it is also believed that homogenous layered propellant could also show complex burning dynamics. As noted, the equivalence ratio seemed to play an important role in the combustion dynamics, so it will be important to isolate this effect from particle size by testing layered homogeneous propellant. Lastly, it is suggested to increase the mismatch in particle size even further by exploring a 400 μm |90 μm |400 μm configuration. This should reveal more insight on the effect of particle size on the combustion dynamics.

6. COMBUSTION OF ADDITIVELY MANUFACTURED LAYERED PROPELLANT

Note that some of the data in this chapter has been presented in Reference [59]. Most of the analysis in this chapter is new and is being prepared for publication.

6.1 Motivation

Shortly after the computational study on layered propellant, the construction of an upgraded VAP was completed. Since the VAP system was limited to high viscosity mixtures, it was not possible to directly manufacture the layered propellant configurations that were simulated in Chapter 5. Therefore, the decision was made to try new layered propellant configurations which included the use of burning rate enhancers, such as iron oxide and nanoaluminum. The experimental study of additively manufactured layered AP propellant presented in this chapter is the first of its kind in known open literature.

6.2 Additive Manufacturing of Layered Propellant

Two different propellant layered formulations were tested. The solids loading of each mixture was 85 wt.%. The slower burning outer layers consisted of monomodal 60-130 μm AP (Firefox), which was sieved below 180 μm to prevent clogging during the additive manufacturing process. The faster burning inner layers either consisted of 1 wt.% 325 mesh iron oxide (Firefox) with 84 wt.% 60-130 μm AP or 5 wt.% 80 nm nAl (Novacentrix) with 80 wt.% 60-130 μm AP. The particle size distributions of the iron oxide, AP, and nAl can be found in the following references [43, 60, 61]. The volume percent of the AP, iron oxide, and nAl propellants are 72.6%, 72.4%, and 72.1% respectively. The binder formulation for all of the layers was 76.55 wt.% HTPB (Rocket Motor Components), 15.05 wt.% IDP (Rocket Motor Components), and 8.4 wt.% IPDI (Firefox).

Nonlayered propellant was prepared in 20 g batches and was mixed in 1 oz containers (Cary Company) via resonant acoustic mixing (LabRAM Resodyn) for two, three minute cycles at 80% intensity. The propellant was then cast into molds and cured at 60 °C for two days to

solidify. The resulting propellant slab was cut into strands that had a width and depth of 3 mm and a length of 25 mm.

An updated VAP machine [54] was used to deposit layered propellant onto a removable borosilicate glass slide. Each propellant was freshly mixed in 10 g batches via resonant acoustic mixing, loaded into a syringe with a 600 µm tip (Zoro), and then printed into a layer within 1-2 hours. Three layers with intended dimensions of 20 x 60 x 1 mm were printed on top of each other by switching syringes and using custom GCODE to deposit propellant relative to the previous surface. The propellant was deposited with a print layer height of 0.25 mm and a print speed of 300 mm/s. Due to the deformation of uncured HTPB propellant, the edges of the final print were cut with a blade which resulted in a final strand length of about 17 mm. Then, the propellant was placed in an oven set at 60 °C for two days. Afterwards, the propellant was cut into strands about 3-4 mm wide.

Note that the propellant formulations and corresponding acronyms are described in Table 1. FeO represents iron oxide, FeOCP represents cast composite propellant catalyzed with iron oxide, LFeOCP represents a middle layer made of composite propellant catalyzed with iron oxide, nAlCP represents cast composite propellant with nAl, and LnAlCP represents a middle layer made of composite propellant mixed with iron oxide.

Table 6-1. Composition of layered and nonlayered propellants.

Propellant composition	APCP	FeOCP	nAlCP	LFeOCP	LnAlCP
85 wt.% AP (3 mm)	X				
1 wt.% FeO/84 wt.% AP (3 mm)		X			
5 wt.% nAl/80 wt.% AP (3 mm)			X		
85 wt.% AP (two, 1 mm layers)				X	X
1 wt.% FeO/84 wt.% AP (one, 1 mm layer)				X	
5 wt.% nAl/80 wt.% AP (one, 1 mm layer)					X

6.3 Print Layer Consistency

Microscopic imaging (Hirox KH-8700) was used to analyze the uniformity of the layers and the interlayer bonding. Figure 6-1 shows a LFeOCP strand and Figure 6-2 shows a LnAlCP strand. The layers are relatively the same thickness and there is only slight interlayer mixing seen in the LFeOCP, whereas there is no visible interlayer mixing in the LnAlCP. The propellant is deformable before it is cured, so it is likely that as more propellant is deposited, there is a shear

profile within the propellant that might cause the layers to slightly mix. However, the nAl propellant was more viscous so it deformed less between the two AP layers, which improved the interface. Overall, the VAP method was able to layer propellant at the 1 mm scale.

Figure 6-1. Microscopic images of LFeOCP. The outer layers are monomodal 60-130 µm AP/HTPB (85 wt.% solids loading) propellant and the middle layer is catalyzed with 1 wt.% iron oxide [59].

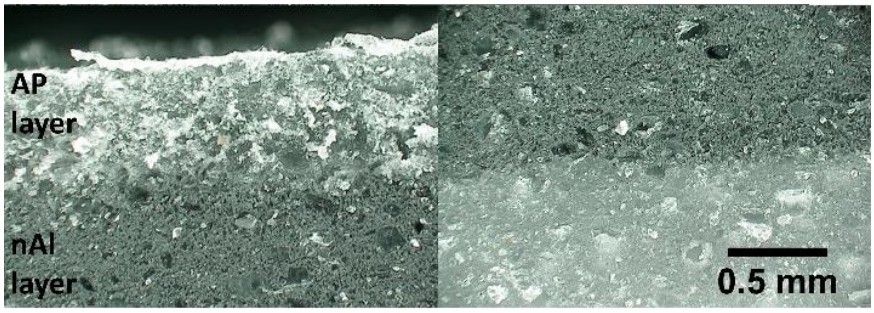

Figure 6-2. Microscopic images of layered LnAlCP propellant. Outer layers are monomodal 60-130 µm AP/HTPB (85 wt.% solids loading) propellant and the middle layer is catalyzed with 5 wt.% nAl [59].

6.4 Layered Propellant Combustion

A Phantom v10 (Vision Research) high-speed camera was used to record the combustion of the layered propellant strands in a Crawford bomb pressure vessel filled with nitrogen. All strands were inhibited with clear nail polish. To reduce the uncertainty in the burning behavior of the printed strands, a light coating of clear nitrocellulose lacquer (Firefox) was used to attach a nichrome wire to the top surface of the strand. The purpose of the nitrocellulose was to create even surface ignition.

In order to explore the development of burning surface area, a layered propellant configuration that was similar to a computational case was studied first (see Chapter 5). Figure 6-3 shows a 130 µm|90 µm /130 µm (CFR 1:1)| 130 µm layered AP propellant (85 wt.% solids

loading) burning at 10.34 MPa. With time, the flat burning surface increases to create a curved burning surface profile 116 ms after the first frame shown. As the surface area develops, the flame gets brighter and the propellant burns faster. This trial case proved that it was possible for layered propellants with different particle sizes to develop a curved burning surface like what was seen in the computational study. However, the difference here is that the solids loading is higher (85 wt.% rather than 75 wt.%) and the layer thicknesses are larger (1 mm rather than 0.5 mm). It is important to use AP/HTPB propellants to experimentally validate computational results. However, matching computational conditions with experimental ones can be challenging, but it is a worthy area for future study.

Figure 6-3. Layered printed propellant burning at 10.34 MPa with 29 ms in between frames. Outer layers are monomodal 60-130 µm AP/HTPB propellant and the middle layer is bimodal 90 µm and 60-130 µm AP/HTPB propellant (CFR 1:1). After flat ignition, a curved burning surface develops [45].

To fundamentally understand the combustion behavior of layered strands, it is important to quantify the burning rate of each constituent propellant. Since the cast propellant strands were thicker than the middle layer of the printed propellant, it was essential to compare the burning rates since it is known that below a critical strand surface area, the burning rate of propellant will be slower due to heat loss to cold surroundings. However, the faster burning middle layer of the printed propellant is not subject to heat loss from cold surroundings, but it could be subject to temperature gradients induced by the surrounding slow propellant layers. Figures 6-4 and 6-5 show the burning rate curves of FeO and nAl based propellant in comparison to the baseline APCP propellant and Table 6-1 shows the pressure coefficients and exponents. The burning rates of the FeOCP and the LFeOCP have very similar curve fits, so it is clear that layering did not affect the combustion behavior. The burning rate curve of the nAlCP was steeper than the burning rate of the LnAlCP. Is it suspected that there is a mismatch in surface temperature between the propellant

layers or that there could be less heat feedback to the surface (the LnAlCP would not have as much radiation heat feedback as the nAlCP [62]).

The rocket problem at equilibrium conditions in NASA CEA was used to analyze the gas temperatures of the APCP, FeOCP, and nAlCP which can be seen in Table 6-2. Kubota's formulation and heat of formation were used for the HTPB calculation ($C_{7.075}H_{10.65}O_{0.223}N_{0.063}$ with a heat of formation of -58 kJ/mol [63]) and the nAl is assumed to have 75% active Al content. It is clear that the difference in temperature between the APCP and FeOCP is low (~20 K) whereas the nAlCP is anywhere from 133 to 142 K higher than the APCP. Since the gas temperatures, and likely surface temperatures, of the FeOCP and APCP are close, there is no major heat loss between the LFeOCP and APCP layers, so the burning rate of LFeOCP is essentially the same when compared to the FeOCP. However, the nAlCP has a much larger gas temperature than the APCP and it is likely that there is an appreciable difference in surface temperature as well. Radiation can largely impact the combustion (surface temperatures) of aluminized propellants, so there is likely some relationship between the thickness of the nAl and the radiation feedback to the surface, which drives the burning rate.

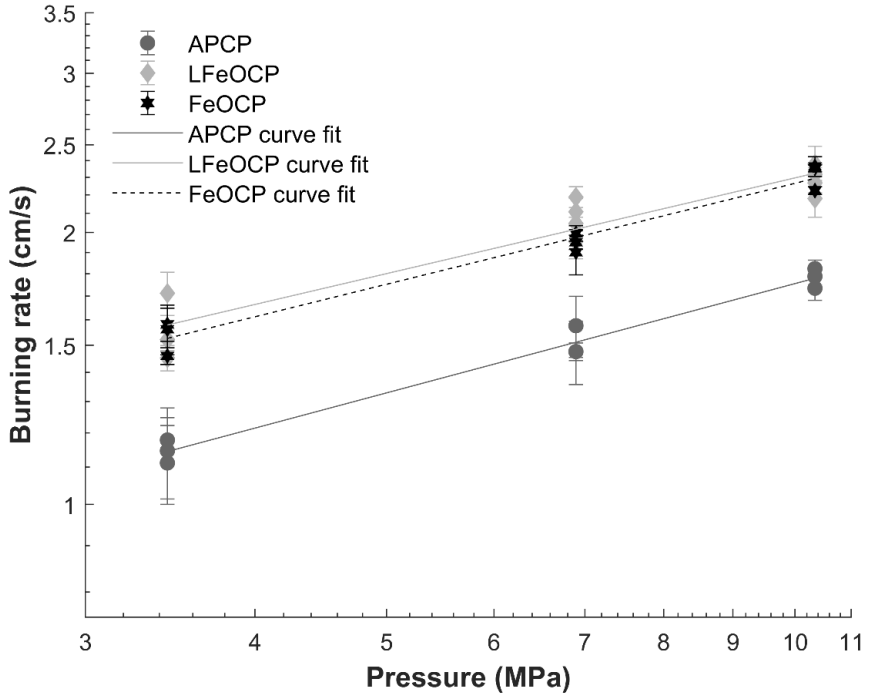

Figure 6-4. Burning rate versus pressure curves of FeOCP, LFeOCP, and APCP. The error bars represent the variation of each data point.

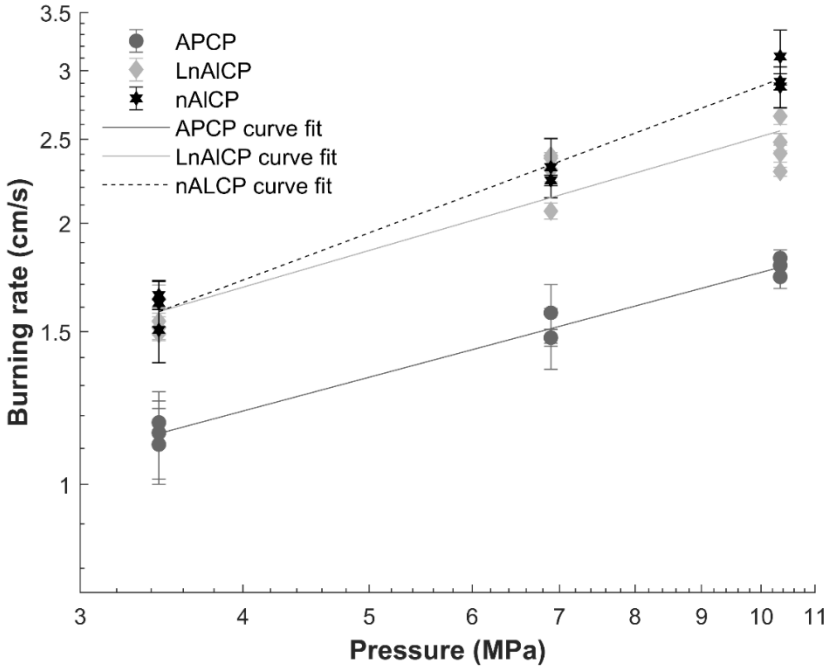

Figure 6-5. Burning rate versus pressure curves of nAlCP, LnAlCP, and APCP. The error bars represent the variation of each data point.

Table 6-2. Pressure coefficients (a) and exponents (n) of the 1 mm thick inner layer of printed propellant and of the cast propellant.

St. Robert's law parameters	AP cast	LFeOCP	FeOCP	LnAlCP	nAlCP
a	0.70	1.02	0.96	0.92	0.79
n	0.40	0.35	0.37	0.44	0.56

Table 6-3. NASA CEA rocket problem equilibrium chamber temperatures (K) of APCP, FeOCP, and nAlCP propellants at 3.45, 6.89, and 10.34 MPa.

Pressure (MPa)	APCP Temperature (K)	FeOCP Temperature (K)	nAlCP Temperature (K)
3.45	2812.20	2831.00	2945.68
6.89	2833.34	2852.97	2972.36
10.34	2843.73	2863.79	2985.51

Figures 6-6 through 6-8 show the combustion sequences of the LFeOCP and LnAlCP at 3.45, 6.89, and 10.34 MPa. There are 116 ms between each frame. In some image sequences, it is clear that when the surface is ignited as a flat surface, the surface area increases into a fully developed curved surface. Even if the ignition does not yield an entirely flat initial surface, the burning surface area still increases until it is fully developed.

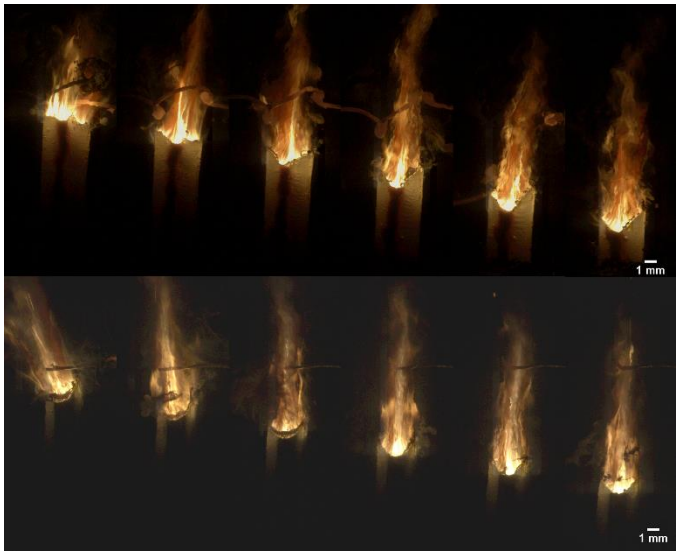

Figure 6-6. (Top) LFeOCP and (bottom) LnAlCP strands burning at 3.45 MPa with 116 ms in between frames. Even after flat ignition, a curved burning surface develops.

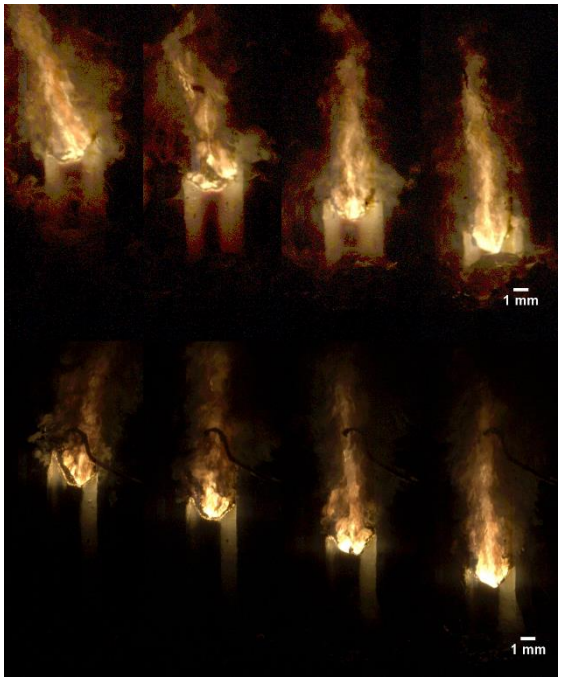

Figure 6-7. (Top) LFeOCP and (bottom) LnAlCP strands burning at 6.89 MPa with 116 ms in between frames. Even after flat ignition, a curved burning surface develops.

Figure 6-8. (Top) LFeOCP and (bottom) LnAlCP strands burning at 10.34 MPa with 116 ms in between frames. Even after flat ignition, a curved burning surface develops.

The surface ratio is defined as the arc length of the fully developed curved surface divided by the width of the strand. This quantity is useful for describing the increase in burning surface area relative to a APCP strand. The burning rate (r_b) difference is defined as the burning rate of the LFeOCP or LnAlCP minus the average burning rate of the APCP. The burning rate difference is believed to be important in describing relative changes in the surface area ratio. The relationship between the surface area ratio and the burning rate difference as a function of pressure can be seen in Figure 6-9. It seems that when the average burning rate difference is highest, the average surface area ratio is highest. However, the response is different between the LFeOCP and the LnAlCP strands. The LnAlCP has the highest burning rate difference, but the change in surface area ratio is similar, if not slightly smaller, than the LFeOCP surface area ratio.

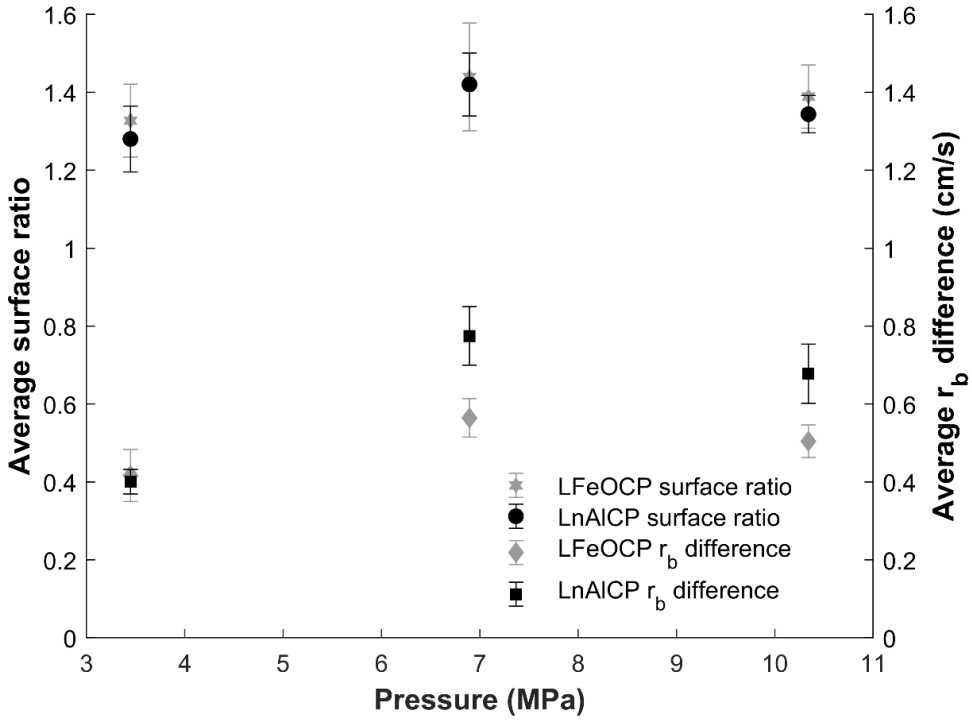

Figure 6-9. The average surface ratio and the average burning rate difference of the LnAlCP and the LFeOCP strands versus pressure. The error bars represent standard deviation in the data.

The transition time is defined as the time it takes for a layered strand to change from a flat surface into a fully developed curved surface. Figure 6-10 shows that as the pressure increases, the transition time decreases. In general, the transition time of the LnAlCP is smaller than the LFeOCP. At first glance, it appears that the transition time of the LnAlCP reaches a regime beyond 6.89 MPa where it is independent of pressure, but one must consider the burning rate curve of the LnAlCP in Figure 6-5 to truly understand the underlying reason. There is little increase in the burning rate of the LnAlCP from 6.89 to 10.34 MPa when compared to the nAlCP burning rates. In general, it is likely that the faster the layered propellant burns, the faster the curved burning surface develops. Since the burning rates of the LnAlCP are similar at 6.89 and 10.34 MPa, the transition times are also similar. If the LnAlCP was thicker (3 mm rather than 1 mm), then it should have a larger burning rate at 10.34 MPa that would approache the value of the nAlCP burning rate. This would then correspond to a shorter transition time at 10.34 MPa, so it appears that the burning rate and transition time are related. The transition time versus pressure slope of the LFeOCP is -14.5 ms/MPa and has a R-squared value of 0.984. The slope of the LnAlCP in the first “regime’

is -15.4 ms/MPa while the slope of the second “regime” is 1.16 ms/MPa. Fast transition times indicate that the benefits of increased burning surface area can be realized quickly after ignition. In addition, designing a functionally graded grain with more reactive propellant could potentially aid in the ignition of regions made of less reactive propellant.

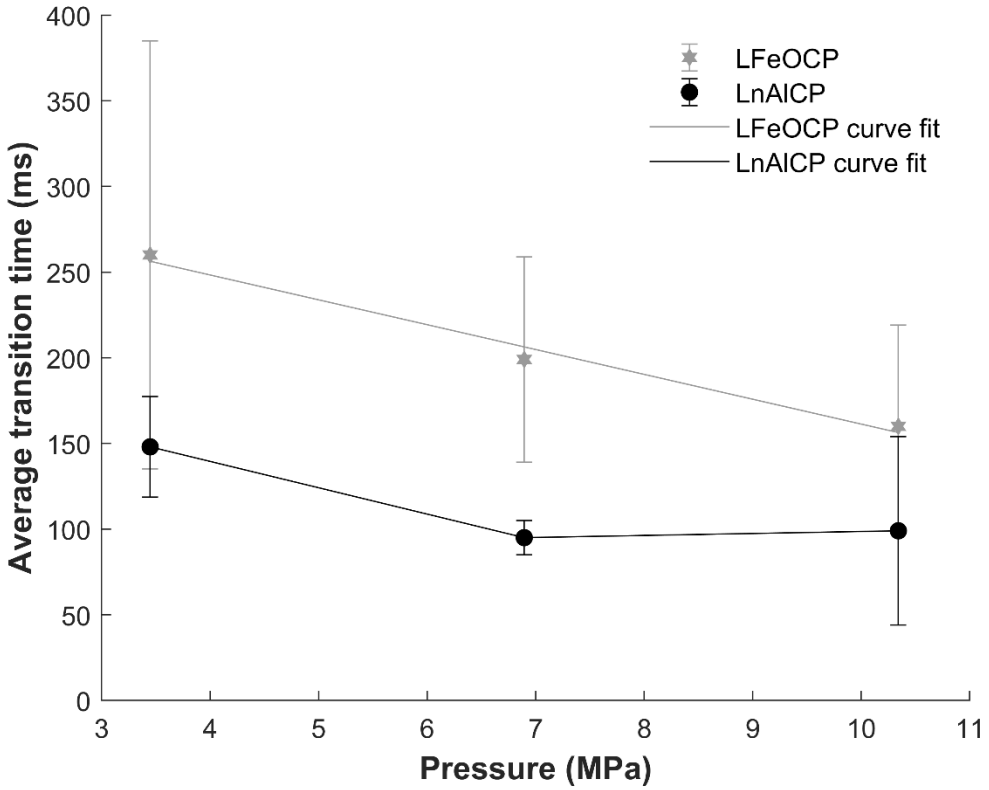

Figure 6-10. The average transition time from a flat to a fully developed curved surface plotted as a function of pressure. The error bars represent the standard deviation of the data.

In addition, the angle of the fully developed surface was quantified. The angle was defined relative to the plane that is perpendicular to the burning direction (or parallel to the stand). Angles on both sides of the inner layer were measured. Those angles were not always consistent since the thickness of the layers had a bit of variation throughout the strand. It is difficult to see a relationship of the angle with pressure due to this variation. However, the angles for the LnAlCP strands are about 49 to 63 degrees while the angles for the LFeOCP are about 38 to 53 degrees as seen in Figure 6-11.

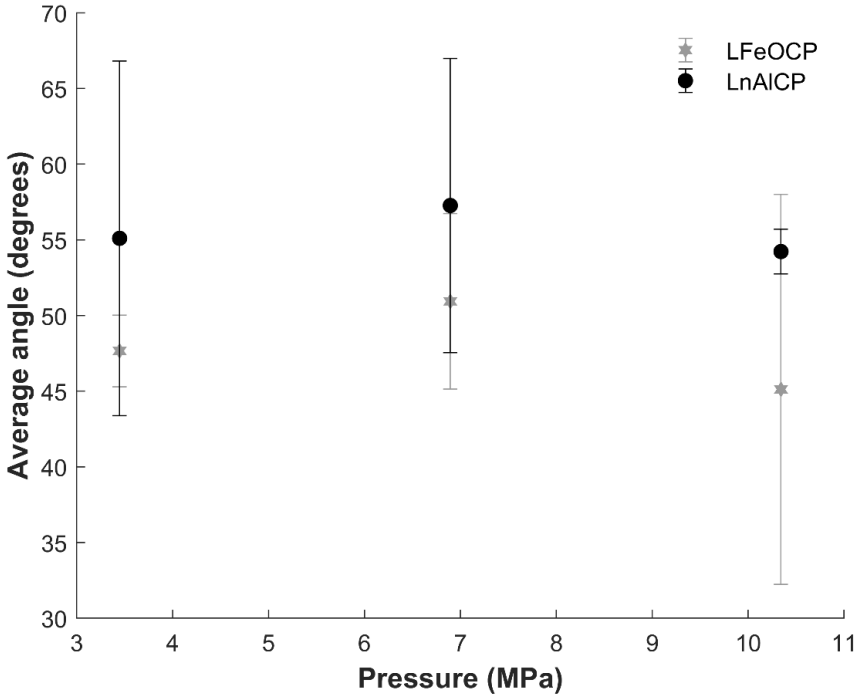

Figure 6-11. The average angle relative to the surface perpendicular to the burning direction versus pressure. The error bars represent the standard deviation of the data.

In order to understand the fundamental relationship between surface ratio and burning rate difference in Figure 6-9 (where middle layer thickness is not considered), it is important to analyze the relationships between the thickness of the middle layer, burning rate difference, and the surface ratio. Although pressure has a clear effect on the burning rate difference and therefore surface ratio, it appears that the middle layer thickness is an important factor for the near-surface temperature gradients between two propellant layers, which is believed to affect the middle layer burning rate. Figure 6-12 shows the relationship between surface ratio and burning rate difference. The relationship is positively linear for the LFeOCP (R-squared=0.997) while it is relatively linear for the LnAlCP (R-squared=0.899). The p-value of the LFeOCP and LnAlCP curves are 0.0328 and 0.206 respectively, meaning that the burning rate difference is a significant driving factor in the surface ratio for the LFeOCP, but not for the LnAlCP. The largest change in the burning rate difference occurs at 6.89 MPa rather than at 10.34 MPa for both the LFeOCP and LnAlCP strands. The burning rate of the LFeOCP does not increase much past 6.89 MPa, while the APCP burning rate still increases slightly, so that explains why the burning rate difference at 6.89 MPa is larger than at 10.34 MPa. This behavior also explains the pressure where the peak burning rate difference

occurs for the LnAlCP. If the thickness of the LnAlCP was closer to 3 mm, then that layer would experience more heat feedback to the surface. Based on the data in Figure 6-5, the burning rate of the LnAlCP would be higher, which would cause the largest burning rate difference to be at 10.34 MPa, rather than at 6.89 MPa, and would possibly result in a larger surface ratio.

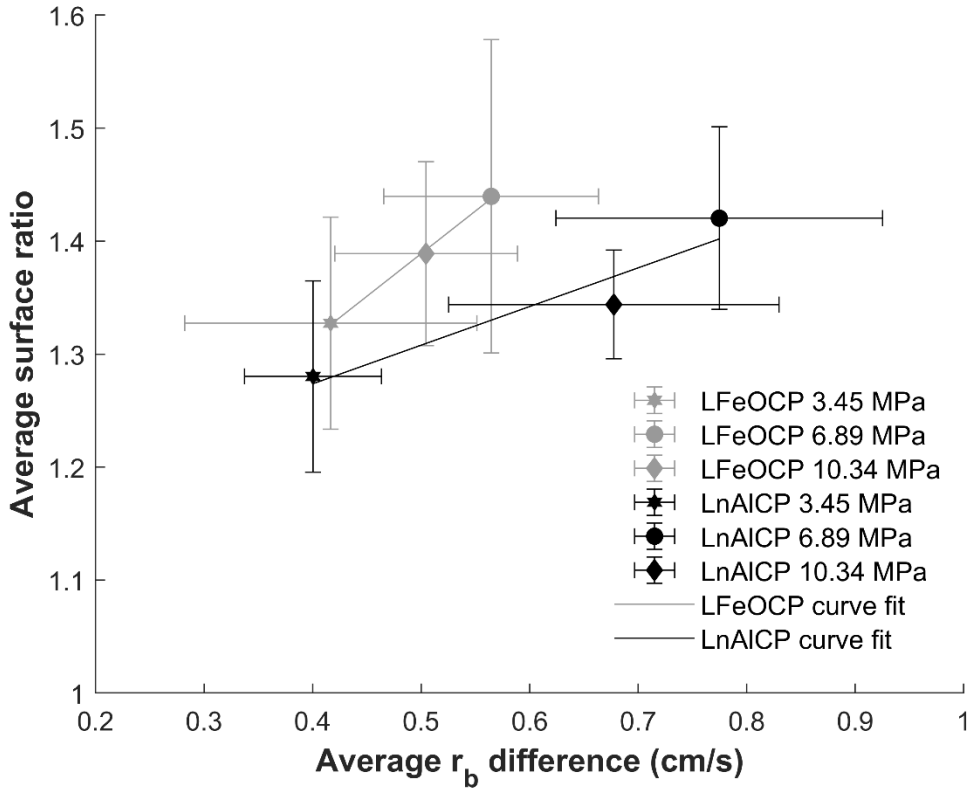

Figure 6-12. Surface ratio as a function of burning rate difference. The error bars represent the standard deviation in the data.

It is important to note that in Figure 6-13, the standard deviation of the average burning rate difference (0.09 - 0.13 cm/s for LFeOCP and 0.06 - 0.15 cm/s for LnAlCP) is on the order of the measurement variation of the middle layer burning rate data in Figure 6-4 (0.03 - 0.11 cm/s for LFeOCP and 0.03 - 0.12 cm/s for LnAlCP). Therefore, it appears that there is not too much deviation in the burning rate difference over the range of middle layer thicknesses (0.65 - 1.33 mm for LFeOCP and 0.52 - 1.62 mm for LnAlCP) meaning that the pressure has more influence. However, if the middle layer thickness varied from 1-3 mm, it is likely that there would be more consistency in the burning rate difference.

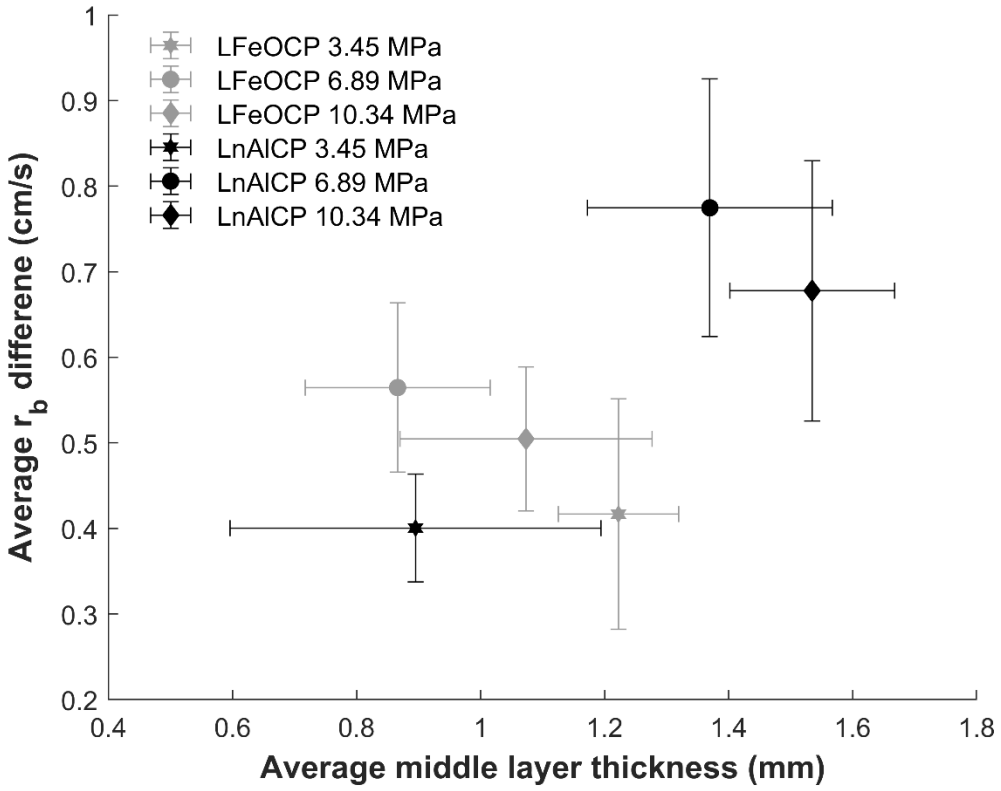

Figure 6-13. Dependence of burning rate difference versus middle layer thickness. The error bars represent the standard deviation of the data.

Knowing that the difference in burning rate drives the surface ratio, the selection of propellants based on burning rate curves is very important to consider in functionally graded designs. Many propellants have different sensitivities to pressure, which are typically quantified by the pressure exponent. If these exponents are different between two layered propellants, then the difference in burning rate will vary at different pressures, thereby changing the amount of surface area increase. For example, the burning rate difference could decrease as a function of pressure if the burning rates converge or it could increase if the burning rate curves diverge. There could even be select conditions where the propellant burning rate curves intersect (likely at lower pressures), so there could be a range of pressure where negligible surface area develops. Theoretically, although likely not common, there could be a low range of pressure where the middle, supposedly faster, layer actually burns slightly slower than the outer layers. Therefore, it is extremely important to consider this in the selection of different propellants since the initial pressurization after ignition will drive how quickly the burning surface area will adjust. It would

likely be useful to select propellants with converging curves so that the burning surface area is highest at lower pressure, which will accelerate the initial pressurization rate of a SRM.

Transition time is also an important parameter. Ideally, one would want the region with the faster propellant to quickly transition from a flat to a fully developed curved surface to rapidly increase the burning surface area. If the transition takes too long, then the immediate benefits of increasing burning surface area will not be realized. Even with the non-optimized propellant used in this study, the 100 - 300 ms time scale is not unreasonable for application and this value could be easily improved by incorporating high performance propellant. It would also be beneficial to identify layered propellant configurations where the transition time becomes independent from pressure because that would ensure a constant a transition time as was seen with the LnAlCP at 6.89 MPa and 10.34 MPa.

The intent in this work was not necessarily to use optimized propellants. Optimizing the nAl content would have significantly increased the viscosity, which would have made it difficult to deposit propellant consistently via VAP. A higher nAl content would have had worse mechanical properties ,such as more porosity, that would have led to erratic and unstable combustion [61, 64]. However, many propellant formulations are compatible with VAP, a process that has been shown to improve the density of propellants [37]. As long as the binders are compatible between formulations and the propellant particles are fully wetted, functionally graded propellant can be manufactured with high precision and will not debond, which is a distinct advantage over relying on adhesives to connect individually manufactured slices of propellant.

6.5 Conclusions

In this work, two types of finely layered (~1 mm) propellant strands with a fast burning inner layer (LFeOCP or LnAlCP) and slower burning outer layers (APCP) were additively manufactured and the combustion properties were studied. The layered propellant was manufactured with minimal interlayer mixing and had some variation in thickness, although it was not unreasonable given the scale of the printing process. The burning rate of LFeOCP with a thickness of 1 mm matched the burning rate of the 3 mm thick FeOCP, whereas the burning rate of the 1 mm thick LnAlCP burned slower than the nAlCP. This burning rate loss can likely be attributed to near surface heat loss from the LnAlCP to the outer APCP layers and overall less radiation heat feedback to the surface. The driving force behind the increase in surface area was

attributed to the difference in burning rate between the inner and outer layers, which is ultimately influence by the pressure. As the pressure increased, the transition time from a flat to a fully developed surface curvature decreased in general. There was no specific correlation between the burning angle and the pressure due to a large variance that was likely caused by local variation in layer thicknesses. Overall, this study quantifies important parameters that are necessary to understand how to design functionally graded propellant and highlights suggestions for the design process.

7. CONCLUSIONS

7.1 Impact

Prior to the research compiled in this thesis, there was little work on how AM affects the combustion of viscous energetic materials. One reason for this research deficiency was the lack of a commercially available AM process that could 3D print viscous mixtures, such as propellants, that have high volume loadings (> 60 vol. %) without the addition of shear thinning additives and with a fine resolution (< 1 mm). With the creation of VAP, it suddenly became feasible to explore the effect of this novel process on the combustion performance and microstructure of realistic propellant formulations. Given that this dissertation work was largely exploratory, rather than dependent on producing a set of explicit deliverables, it was possible to investigate how AM could expand the feasible design space of propellant grains.

First, it was important to establish VAP as a viable method to produce defect-free propellant strands with a high volume loading (> 70 vol.%) and viscosity (69 million cP). It was found that VAP was capable of producing 3D printed propellant strands of AP/HTPB and AP/UV-curable epoxy with improved density when compared to their cast counterparts. In addition, the VAP process did not negatively affect the combustion of the strands in high pressure environments. An internal void was intentionally 3D printed into a section of a strand that was otherwise fully dense. The demonstrated change from conductive burning in the fully dense section to convective burning in the section with a void showed the ability of VAP to produce geometries that cannot be traditionally manufactured via casting.

Once VAP was established as a viable technique to 3D print propellant strands, a photopolymer that was compatible with VAP and that could cure at reasonable depths (even with the addition of opaque aluminum particles, which are commonly used to increase the burning rate of propellants) was developed and characterized. It was found that the final properties of the photopolymer could be customized by varying UV-light parameters, such as wavelength and intensity. It was also possible to customize processing properties of this photopolymer mixture (i.e. adhesion or viscosity) by changing the ratio of the oligomer and the reactive diluent. Lastly, a technique that was able to measure the cure depth of propellant with a high solids loading was developed. By using this technique, it was shown that it was possible to cure propellants quickly

(in 45 s) to a wide range of cure depths (0.5 to 3 mm), all of which are deeper than the print layer height that is used in the VAP process (0.25 mm). At least one of these propellant formulations has been 3D printed and cured layer-by-layer with a UV-light that was integrated into a VAP system. In addition, propellant samples that were burned at atmospheric conditions did not seem to crack at the burning surface front.

A new research area that the author has not seen applied to AP composite propellant in open literature was explored in this thesis. The behavior of functionally graded propellants, or propellant structures that are made of more than one propellant formulation, is an important area of study if one wants to exploit the ability of VAP to construct finely layered multi-formulation propellant strands, since is not economical and is extremely tedious (if at all feasible) to produce them with traditional casting. First, a computational tool called Rocfire, which has been shown to simulate propellant burning rates of AP/HTPB propellants, was used to model the combustion of finely layered propellants. The particle size of the AP in the middle propellant layer was decreased in order to increase the burning rate of the middle layer relative to the burning rate of the outer layers. It was found that the orientation in which the layers were burned produced vastly different burning rate profiles. When the layers were perpendicular to the flame front, the surface area changed from a flat front into a curved surface, resulting in a steady acceleration in the burning rate. When the layers were parallel to the flame front, large changes in the burning rate (over and undershoot) were seen at the interfaces. The local equivalence ratio and the local surface area ratio were determined to be critical factors in this dynamic combustion behavior that was not necessarily intuitive prior to this study.

Lastly, VAP was used to additively manufacture functionally graded layered propellant. The propellant in the middle layer was either enhanced with iron oxide or nAl, while the outer layers were composed of AP composite propellant. The layered propellant strands were burned at a variety of pressures, and the burning rates of the middle layers were compared to the burning rates of cast nonlayered propellant. It was found that the burning rate curve of the LFeOCP was essentially the same as the burning rate curve of the FeOCP. However, the pressure exponent of the LnAlCP was less than that of the nAlCP. It is believed that the heat feedback towards the surface of the LnAlCP is not as high as that of the nAlCP, likely because of the reduced radiation feedback along the entire propellant surface. In addition, there is a mismatch in the adiabatic flame temperatures of the nAlCP compared to the APCP and the FeOCP, which had similar values. New

metrics such as transition time, surface ratio, and burning rate difference were used to describe the experimental combustion of layered propellant and images of the microstructure showed clean, well bonded interfaces between the layers.

To summarize, the main contributions of this work to the energetics materials community were 1) to show that the VAP process is a viable option to produce high quality AP/HTPB propellant that performs well at high pressure, 2) produce a photopolymer mixture that is compatible with metalized propellants while achieving reasonable cure depths (0.5-3 mm), 3) analyze the combustion of layered propellant computationally to understand the effect of particle size and burning orientation on the burning rate response, and 4) conduct combustion experiments on additively manufactured layered propellant to understand the factors that drive the increase in burning surface area at relevant pressures. This body of work explored fundamental studies that are necessary to produce additively manufacturing functionally graded viscous structures with complex geometries. In particular, this work specifically has application to solid composite propellant, but the manufacturing techniques used can be extended to other viscous mixtures such as explosives, other types of propellants, ceramics, and composites.

7.2 Future Work

Although several significant milestones were accomplished in this thesis, there are many more research questions that can be answered in the near future. For example, although the photopolymer used in Chapter 4 was able to cure aluminized propellant to large cure depths, there are still questions as to how the UV-curing process affects high pressure combustion and mechanical properties. Curing the photopolymer with different parameters changes the stiffness of the cured section and will be important to characterize. In addition, as more layers are cured, there will be more potential failure points. One way to investigate the quality of the UV-cured propellant is to use flexural tests (ASTM C1161), since the propellant is rigid and brittle rather than flexible like HTPB. Flexural tests have been used before to test layered ceramics [65], and the failure modes from this experiment can be used to qualitatively investigate if the strength of the interfaces is weaker than the strength of the cured polymer matrix. In addition, high pressure combustion can be used to investigate if the degree of curing has an effect on the propellant strand quality.

In this thesis, a new research area in layered propellant combustion was initiated. There are many research questions as to how layered propellant interacts in pressurized environments. A

computational study enabled the ability to test finely layered propellant (~500 μm layers), which has been proven to be very difficult to study experimentally due to heat loss. In addition, it allowed the study of burning layered propellant in a horizontal configuration ,which would be difficult to test experimentally if the layers are very thin (mm scale). The simulated results of the layered propellant burned in the vertical orientation verified that the burning surface area could increase over time and this behavior was also later seen in experimental studies. However, there are still questions as to how the layering algorithm affects the combustion of the layered propellant. There are also questions about how to accurately model additively manufactured propellant when it is suspected that a random packing algorithm produces a vastly different microstructure since fluid flow is not considered. In addition, there are questions as to what the driving force is (particle size or equivalence ratio) behind the dramatic combustion dynamics seen in the simulations. The effect of layer thickness, pressure, and particle size (i.e. bimodal or trimodal) should be investigated in future studies.

The additively manufactured layered propellant (~1 mm thick layers) developed an increase in burning surface area at high pressures. However, it is still unknown how the thickness of each 3D printed propellant layer affects combustion. A future research area could be to further investigate the effect of middle layer thickness on the middle layer burning rate. Although some metrics were identified to describe the performance of layered propellants, it will be important to develop analysis techniques with less error so that it will be easier to discern trends. For example, an image processing code that could calculate the burning surface length of the layered propellant over time would be useful for determining what the surface ratio is in real time and how it fluctuates. It could also more accurately describe how long it takes a layered propellant to ignite and then change into a fully developed surface where there is no further increase in burning surface area. The interaction of other propellant formulations should also be investigated.

Given that there now exists a foundation to 3D print realistic propellant formulations into complex geometries and functionally graded structures at small scales, the question now becomes where will this research take the design and manufacturing process of propellants and other energetic materials in the future? With more rigorous characterization on the effect of additive manufacturing on the performance of 3D printed propellant, it will become possible to refine the process of 3D printing and reduce the current parameter space. Customized slicing software is necessary to enable the manufacturing of large structures that may require multiple nozzles to

construct a grain. In addition, continuous upstream mixing of propellant will be necessary to enable the manufacturing of larger motor grains, since batch to batch preparation will limit manufacturing time and induce more variability. Alternately, small scale manufacturing of propellants can have niche applications in thrusters or igniters to improve performance efficiency and reliability. Either way, increased customization and improved quality control techniques will be necessary to further expand the design space and improve the reliability of additively manufactured propellant structures. In addition, dissimilar material additive manufacturing, where two different AM processes are joined to deposit materials with very different viscosities, adhesion, stiffness, etc. will be an important step for manufacturing propellant grains that require reinforcement during transportation (i.e. 3D printing a thermoplastic or an ablative casing around the grain for protection) or functionally graded propellants (i.e. reactive Al/PVDF wires in propellant).

APPENDIX A. GCODE

Inventor was used to generate the 3D CAD files for this dissertation work. Initially, Cura was used to generate the GCODE necessary for VAP. In addition, some custom scripts were used to control the on/off cycle of applied vibrations. Specialized lines of code were used at the beginning and the end of the file to deactivate printer components such as the fan and the extruder temperature. Later, Simplify3D was used instead of Cura since it has more customization features. A custom script was made to control the on/off cycle of UV-light and the cure path. In addition, Notepad+ was used to make slight manual adjustments to the GCODE, such as changes in the print speed or layer height.

APPENDIX B. 3D PRINTER DESIGN

The printing platforms that have been used for VAP are the IIIP Monoprice mini and a DIY dual nozzle Prusa i3 printer. In general, it is beneficial to use 3D printers that have open source firmware and slicing software so that modifications for VAP can be made. A Hyrel 3D printer that was originally purchased for multi-material printing was not capable of accomplishing that task because the software/firmware was not open source and the print heads were not designed to be level. The lack of open source capability also prevented the attempt to add VAP capabilities to the printer. The Prusa i3 printer on the other hand, was successfully adapted to print VAP and FFF together [54]. It is potentially possible to use this printer to manufacture propellant grains with thermoplastic casings or reactive wires that can be additively manufactured (see Appendix G for the role of reactive wires in propellants). Lastly on the modified printer, the VAP head was leveled with an electromagnetic induction probe that can sense the metal print bed. The addition of this leveling feature was important for additively manufacture layered propellant in Chapter 6.

APPENDIX C. 3D PRINTING PROCEDURE

1) Preparing GCODE
    a. It is best to print propellant at a speed of 250-300 mm/s, although other viscous mixtures could print slower. In general, propellants made of finer particles print more consistently, but require slower speeds. A typical print layer height is 0.25 mm. The nozzle diameter should be set to 0.5 mm (no more than 0.6 mm) in the slicing software to ensure some overlap in the deposited material. Be sure to disable commands for the fan, variable print speeds (many slicing softwares change the print speed between the first layer and top layer as well as the infill versus the shell), bed temperature, and extruder temperature. You can also save the settings profile that you created which will be useful in the future.
    b. Export GCODE
2) Postprocessing GCODE
    a. Use Notepad+ to verify that the speeds are correct (search for F throughout the document).
    b. Use **parse_V2.py** to add in UV-light commands if necessary (written by Aaron Afriat). The parameters that can be changed in the script are part_diameter (in mm and will determine the printing area), desired_height (in mm and the UV-light will be activated every time the specified height is printed), fan_time (in s and determines how long the UV-light is activated), light_diameter (in mm and represents the diameter of the projected beam), and overlap (in mm which determines how much the UV-beam path should overlap during curing). Make sure to save the GCODE in the same folder as the script. The command should look like **parser_V2.py name.gcode**. The output script will be **name_parsed.gcode** and will be saved in the same folder.
3) Test GCODE
    a. Always run a new GCODE on the printer before testing it with energetic materials. This will ensure that everything is working properly and will improve safety during manufacturing. Depending on the printer, the GCODE must be saved on a 1-2 GB

microSD or SD card to work. SDHC formatted cards will not be compatible with the printer.

4) Mixture properties

a. Mixtures that are compatible with VAP should have the following properties: no clumping (can be avoided if the particles were sieved), the biggest particle diameter should be less than 1/3 the nozzle diameter to prevent clogging, the material should stick to itself well (if it breaks up easily, it will be harder to print).

5) Pre-printing procedure

a. The more material that is loaded into the syringe, the more friction the reservoir feeding system (pressure fed or motor fed) has to overcome. For really viscous materials, fill the syringe about 1/3-1/2 of the way. Usually 10 g of propellant is a good amount. Eliminate air bubbles and try to push the material as far down into the nozzle tip as possible. Add the stopper and push until it makes contact with the material. The stopper is supposed to separate the material from the air so be sure to inspect the seal. When the material stops flowing during VAP, sometimes this is because the plunger has stopped moving so that is cannot feed reservoir material to the nozzle tip. If an energetic mixture is used, complete this step in a fumehood or other well ventilated area to reduce exposure.
b. If an energetic mixture is used, then make sure there is some sort of ventilation near the printer or PPE (respirator) to prevent exposure.
c. If using a pressure fed system, pressurize the material to 40 psi and let it sit a bit (5 min). If the material is visibly moving, leave the syringe pressurized at that level. If nothing has moved, raise the pressure. Do not exceed 90 psi (syringes are rated to 100 psi). Wait until the material starts to peek through and try to let some flow out. If the material does not stick to itself well, higher pressures will cause the material to spit out in chunks since it is not strong enough to stick to itself. You have to use lower pressures for these mixtures and run the VAP head at lower intensities or the material will separate and become messy. Note that sometimes, you can use a needle to poke the mixture in the nozzle tip to induce flow. However, if the mixture is dry, this will not help (spitting will occur). In addition, sometimes after material flows a bit due to the needle, it will slow down again and may stop at some point.

d. Relieve the pressure.
e. Verify that the VAP probe is secured tightly to the VAP head. If it is loose, it will cause the local temperature to increase enough to melt the polypropylene syringes. One can test this by running the VAP head and either quickly touching the head or using an IR camera to monitor temperature. In addition, one can verify that the VAP head is working by placing a thin piece of metal on the probe (one should hear screeching).
f. Secure the syringe into the VAP head. Make sure that the syringe does not move. One can wrap foam around the syringe to help sure it better. When screwing the nozzle tip into the VAP probe, only use between 1-2 full rotations. If the nozzle is secured to tightly, the nozzle walls could contract inward and reduce the effective inner diameter. One can test this by slipping a needle through the syringe tip to verify that there is space.
g. Pressurize the syringe and let sit the syringe for a few minutes before activating the VAP head. Set the pressure slightly lower than what was used in step 2. The pressure should not cause the material to flow out. It should just hold it in place.
h. Activate the VAP head. The goal is for the material to be responsive to VAP activation/deactivation and flow in a continuous manner. If the flowrate does not change when the VAP head is turned on or off after multiple attempts, then it is likely that either the pressure is not correct, the syringe is not packed properly, or the syringe is not secured properly into the head (too may rotations or not firmly secured). If the flow is not continuous, then it is likely that there are voids in the reservoir material, the pressure or magnitude of the vibrations is too high, or the plunger is stuck.

6) VAP printing procedure

a. Turn on the printer
b. Insert the microSD/SD card
c. Run the desired GCODE, but start with the VAP head off. First, you want to see where the syringe tip will hover so that you can level the printing surface for your setup. If you plan to place the finished product in the oven, make sure to print onto something that can survive in the oven (glass or borosilicate slides). Double sided tape seems to work well for adhesion or part removal, although it is not always

necessary. When you are satisfied with the X and Y position, tape the slide to the printing bed. Make sure to calibrate the Z offset as the print head descends with the metal detector sensor. The nozzle tip should not drag on the printing surface. It should be low enough that the material will stick to the tape but not to the point that the material spreads out too much or does not come out at all. ~1 mm is recommended. Once the positioning is set, cancel the printing code and get ready for the actual printing

d. Start the GCODE and turn the VAP head on. Observe how the material sticks to the double sided tape. Manually adjust the VAP vibrations to ensure continuous extrusion. If you find that the print speed is still too fast to match the extrusion speed of the VAP head, then you will have to alter your GCODE (easy change by search F commands and replacing all in Notepad + after you cancel the print). Usually, it will take a layer or two for the flowrate to stabilize after you have determined the appropriate parameters. There is a lag in the response of the material to changes in the VAP settings, so it is important to monitor the entire print. Usually, it is best to slowly change one parameter (back pressure or VAP input parameters) at a time and wait at least few minutes to see the consistency at steady state. There are a few parameters that you can modify during the print:
    i. Pressures that are too low will not allow the reservoir material to keep up with the nozzle flow rate. Pressures that are too high can cause the material to shoot out. Some materials (typically those with a low binder viscosity) will dewett from particles at higher pressures. In general, it might be necessary to change the pressure slightly throughout the duration of a print, but it is not recommended to change this drastically.
    ii. Print speed: This is dictated by GCODE and should ideally match the flowrate of the material. It may take some trial and error to figure out which print speeds match the extrusion speed of a material.
    iii. Magnitude: This VAP input parameter will change how fast the material extrudes or potentially heats up. It is best to operate in mid-range magnitudes to prevent overheating.

7) Cleanup

a. After a long print, depressurize the syringes and turn off the printer and VAP head. Clean up the area with IPA and be sure to remove as much excess material as possible. Remove the syringe and clean the VAP probe (if this is not clean, then it will be difficult to ensure proper contact with nozzle tips). Properly dispose of energetic materials (i.e. burning or REM hazardous waste pickup).

APPENDIX D. VISCOSITY DATA

Measurement of viscosity is crucial for determining the printability of a propellant mixture. In general, it is difficult to measure materials with high viscosities. Although a capillary rheometer is useful for measuring the viscosity of various types of clay (see previous study [31]), it was not available for testing energetic materials because it was located in another lab across campus. A capillary rheometer does require a decent amount of material (100 g of fondant mixture from reference [31] was used for both test sections) which is compressed in the measurement section. A minimum pressure of 0.5 MPa is needed before measurements are taken, but pressure can easily be increased by the compression speed and could exceed a safe limit. Rotational viscometers do not require compression of the material. Therefore, rotational viscometers tend to be a much more common tool to measure the viscosity of energetic materials.

According to Brookfield, the manufacturer of the viscometer used in the first additive study [45], the recommended amount of test material is 500 mL in a 600 mL beaker. The reason is to prevent an artificially increased viscosity measurement when the edges of the rotating spindle (HA/HB) are too close to the beaker walls. However, this recommendation is based on a viscous liquid rather than a paste/slurry. T-spindles tend to have smaller measurement diameters than the standard spindle and are meant to measure viscous materials. Therefore, a mini study was conducted to see if less propellant could be tested, yet yield the same viscosity measurement (no wall effects).

First, the Brookfield viscometer was calibrated with N4000 fluid. Based on the viscosity versus temperature curve, the measurements taken with a HB4 spindle (greater than 10% torque which is necessary for an accurate measurement) showed that the viscometer was calibrated as seen in Figure D-1.

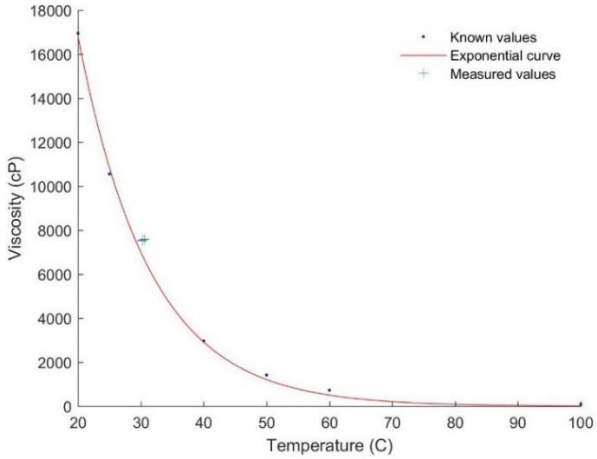

Figure D-1. Viscosity measurements of N400 calibration fluid with HB4 spindle in a 600 mL beaker compared to the calibration values.

It is generally known that many propellants have shear thinning behavior (viscosity decreases with increasing shear rate) as seen in Figure D-2. One way to characterize the degree of shear thinning is the pseudoplasticity index (PI) [25]. The PI is the exponent of a curve fit of viscosity versus shear rate (or rotational speed) on a log-log scale multiplied by 100. It only applies to propellant that is shear thinning. Propellants also exhibit rheopectic behavior (meaning that the viscosity increases over time) because of the crosslinking process. Both properties are important to characterize.

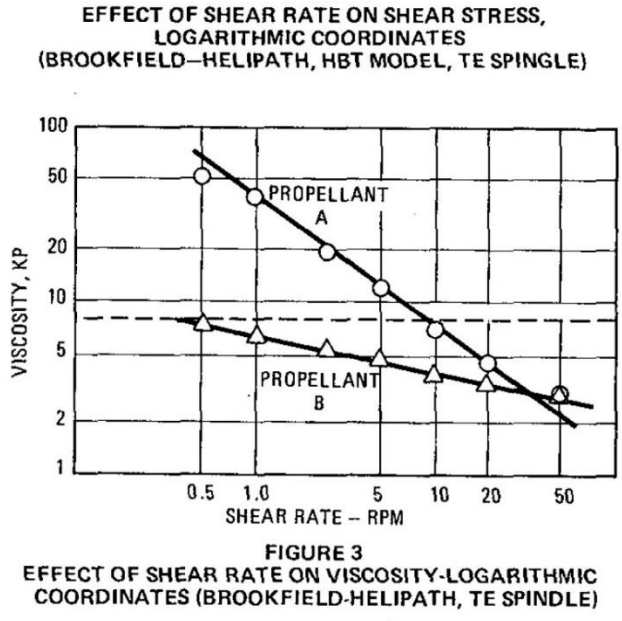

Figure D-2. Typical propellant viscosity curves versus shear rate [25].

Initially, natural clay was used to compare the effect of beaker size on viscosity measurements. A T-F spindle was used and the clay was manually packed into the beaker to remove air pockets. In order obtain more accurate measurements, the spindle was allowed to descend into the material for 30 s before measurement began. Several measurements were made during the descent that were averaged and no further measurements were taken when the spindle was close to the bottom (the viscosity would noticeably increase at this point due to wall effects). The data can be seen in Figure D-3. In general, there is not a large difference in measurement between the 100 mL, 250 mL, and 500 mL amounts of clay likely because the T-F spindle was small and far away enough from the beaker walls. However, the PI varies slightly and it is clear that the 100 mL data is not as linear as it should be. In general, it was decided that it would be acceptable to scale down from the standard of 500 mL of material to smaller amounts of propellant for rotational viscosity tests since there was plenty of overlap in the data.

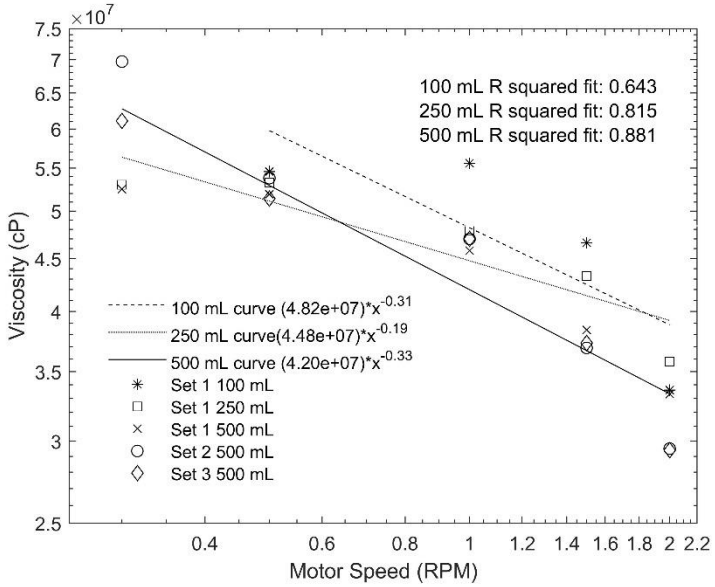

Figure D-3. Viscosity of natural clay in different containers as a function of rotational speed.

The next step was to test the viscosity of propellants. To simplify the process, no curative was added to the mixture. Monomodal propellant with 60-130 μm AP and R-45M resin was used with a varied solids loading. 216 g of propellant was used for each test (~140 mL in a 150 mL beaker). Since it was difficult to mix large batches of propellant in the resonant acoustic mixer at 80% intensity, it was necessary to split the propellant batches into 150 g and 66 g mixtures. Figure D-4 shows the viscosity measurements of propellant with 80, 82.5, and 85 wt.% solids loading.

The 80 wt.% propellant was tested at 25.3-26.2 ºC and had a PI of 81, the 82.5 wt.% propellant was tested at 22.7-22.8 ºC and had a PI of 36, and the 85 wt.% propellant was tested at 26.6-27.2 ºC and had no PI (this mixture was shear thickening, or dilatant). It is clear that even small changes in solids loading can dramatically change the viscosity behavior in a propellant.

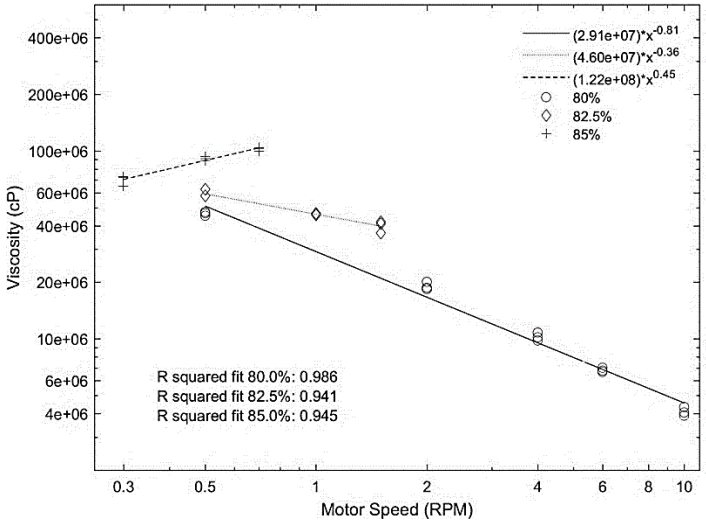

Figure D-4. Viscosity of 140 mL of propellant (AP/HTPB without a curative) in a 150 mL beaker as a function of rotational speed and solids loading.

The next set of viscosity tests involved an AP/HTPB propellant with a fast acting curative. The solids loading was 80 wt.% and the binder formulation was 86.93% R-45M resin and 13.07% Desmodur E-744. The test was conducted with a T-F spindle at rotational rate of 4 RPM and at a temperature of 28.6 to 29.1 ºC. Figure D-5 shows the shear thickening process, which is commonly known as viscosity buildup. The crosslinking process is initially slow, but then it dramatically speeds up past 70 min.

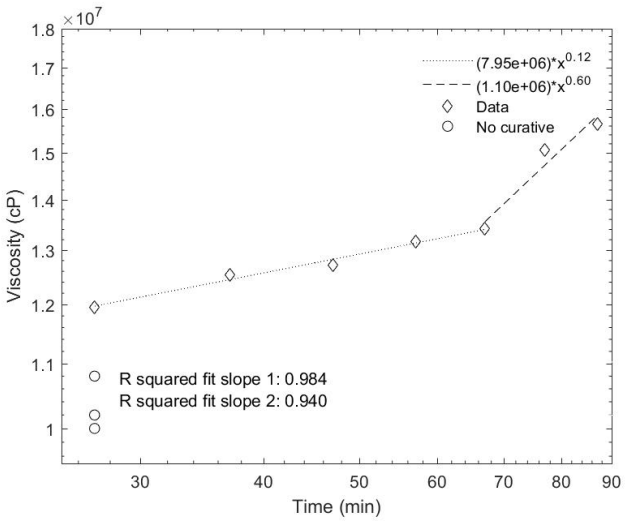

Figure D-5. Viscosity of 140 mL of propellant (AP/HTPB with Desmodur E-744 curative) in a 150 mL beaker as a function of time. The rotational speed was 4 RPM.

Lastly, the viscosity of 85 wt.% solids loading (CFR 1:1 of 60-130 μm AP and 20 μm AP) was measured. The binder was composed of HTPB, IDP, IPDI, and Tepanol (refer to Section 3.2 for details on the formulation and the mixing process). 250 g of propellant was mixed and packed into a 150 mL beaker. Figure D-6 shows that before 150 min, there is a lot of variation in the viscosity. Shear thickening does not happen within the test time frame (3 hours). Although this data was taken on a different day than the data seen in Figure 3-4, the values are relatively similar and prove that this measurement process produces repeatable results.

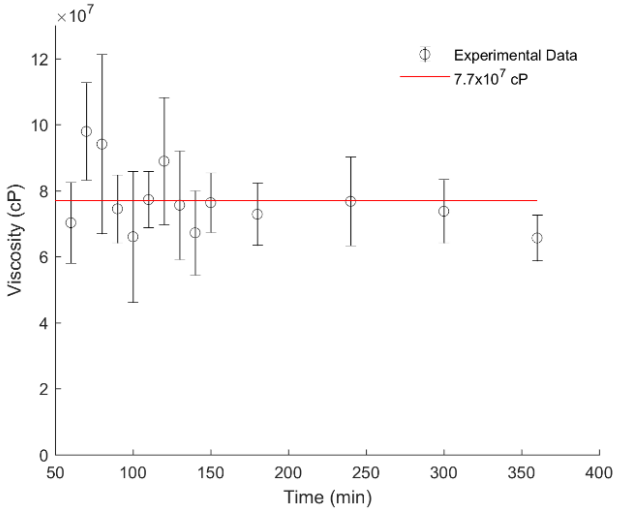

Figure D-6. Initial data on the viscosity of 85 wt.% solids loading (CFR 1:1 with 60-130 μm and 20 μm AP) propellant over time. It is comparable to the viscosity in Figure 3-4 [37].

APPENDIX E. NASA MARSHALL SPACE FLIGHT CENTER SUMMER 2018

Note that the study in this section is based off of Reference [66]. The work in this section has been paraphrased.

Background

Solid rocket nozzles are typically made out of ablative materials, such as graphite and fiber reinforced phenolics or epoxies [4] because the flame temperatures of solid propellants are extremely high and the exhaust species are volatile. In addition, solid rocket motors are typically not made for reuse, so using actively cooled nozzles is not economical. Ablative materials provide a tangible solution since they erode slowly so that the shape of the nozzle is preserved well enough during flight, have low manufacturing costs compared to actively cooled nozzles, and do not add a significant weight penalty. In addition, the ability to additively manufacture an ablative nozzle could potentially reduce manufacturing cost since molds/mandrels will not be needed. Lately, there have been several studies on the printability of carbon fiber reinforced thermoplastics, via FFF [67-69]. One study showed that a filament reinforced with continuous carbon fiber was only printed with 10 wt.% carbon fiber, while other studies that used customized filaments with discontinuous carbon fiber had a fiber content no higher than 40 wt.%, because it led to undesirable rheological properties that would clog the nozzle. Although these mixtures can be printed into shapes where the fibers are highly oriented with the flow [69], the tradeoff is that a much higher degree of fiber reinforcement is necessary to reduce the erosion rate at realistic conditions. The nozzle is where the harshest chemical, mechanical, and thermal conditions are experienced in a rocket. In addition, the throat area is the point at which the highest heat fluxes are present, making it the most susceptible to erosion. If the throat area rapidly increases, it will not be possible for the motor to maintain supersonic speeds. Therefore, it is doubtful that thermoplastics with relatively low fiber reinforcement will survive long enough to be a useful material in a SRM environment that can have combustion temperatures on the order of 3000 K.

A different AM approach is necessary. In this brief study which was specifically requested by Dr. Jonathan E. Jones at NASA Marshall Space Flight Center, there was strong interest in applying

VAP to this unique problem. The reasoning was that since VAP can print viscous mixtures with high particle solids loadings, it could be possible to increase the overall carbon fiber content in a final part compared to previous literature involving FFF research. Ultimately, this led to the selection of a different mixture which ended up being carbon fiber and polymer based. The polymer used was a ceramic forming polymer that can be post-processed into a ceramic. If mixed with reinforcing materials, it can be classified as a ceramic matrix composite (CMC).

CMCs appeared to be the perfect material for this study since they have been used for many high temperature applications. A well studied CMC is carbon fiber reinforced with silicon carbide (C-SiC), which is a low erosion rate ablator that shows promise for SRM applications [70]. For example, C-SiC composite vanes were subject to a SRM exhaust and an erosion rate of 1-2 mm/s [71] was measured (comparable to the erosion rates of traditional fiber reinforced phenolics [4, 72]). In addition, a C-SiC nozzle has survived LH_2/O_2 flames [73] and eroded at a rate of 0.05 mm/s near the throat in UH25/dinitrogen tetroxide flames [74]. It has also been found that fiber orientation affects the erosion rate of nozzles [75].

There are multiple methods to create CMCs, although some are more costly than others. Polymer pyrolysis is the method of choice for this study since it is compatible with AM of viscous materials. Polycarbosilane is a direct precursor to SiC, but it is not viscous/sticky enough to be compatible with VAP. Even if mixed with carbon fiber, it is likely that the polymer would separate from the fibers easily and the printed component would deform easily. Polysiloxane is a ceramic precursor that can pyrolyzed into silicon oxycarbide (SiOC). Basalt reinforced SiOC composites (0.25 in thick) made via pyrolysis have been shown to withstand flame temperatures of 3500 °C for up to 30 s [76]. In addition, multiple cycles of polymer reinfiltration and pyrolysis (a typical process to reduce porosity) was not necessary for the components to perform well. Therefore, polysiloxane was chosen for this study. Although carbon fiber and ceramic forming polymers have been 3D printed with DIW before [77], only a 33 vol.% of carbon fiber was achieved with a 840 μm tip and the print speed was 10 mm/s, which is slow. The objective of this feasibility study was to determine the maximum fiber loading in a polysiloxane mixture that VAP could manufacture and to quantify some properties of those mixtures to assess their viability for solids rocket nozzle construction.

Formulation and printing mini study

The ideal formulation would have a higher fiber loading, be printable, and be able to hold its shape after being printed. The polysiloxane based precursor was composed of 99.98 wt.% of Methylphenylvinylpoly(siloxane) (Polyramic SPR-688 from Starfire Systems) and 0.2 wt.% of a platinum divinyltetramethyldisiloxane complex catalyst (CAT 776 from Starfire Systems). The purpose of the catalyst was to allow the mixture to be thermoset, which occurs at much lower temperatures than pyrolysis. Initially, a 4 fan blade rotational mixer (Mophorn 20L 2000 RPM) was used to make 40 g mixtures of pure carbon fiber (100 μm length, 7.5 μm diameter from Easy Composites) with polysiloxane in varying ratios. First, the fibers were wetted by the polymer at a speed of 80 RPM for 10 minutes. Then, the speed was increased to 350 RPM for 2-4 hours depending on the wt.% of carbon fiber. A maximum of 60 wt.% (48.1 vol.%) carbon fiber could be mixed with this method. However, it was difficult to deposit this material consistently. Regardless, a dogbone was successfully printed with a layer height of 0.25 mm and a speed of about 300-330 mm/s as seen in Figure E-1. The 50 wt.% (38.1 vol.%) mixture extruded much easier, but the final structure deformed as seen in Figure E-2(a). However, the fully pyrolyzed sample appeared to have a reasonable density based in visual inspection [Figure E-2(b)].

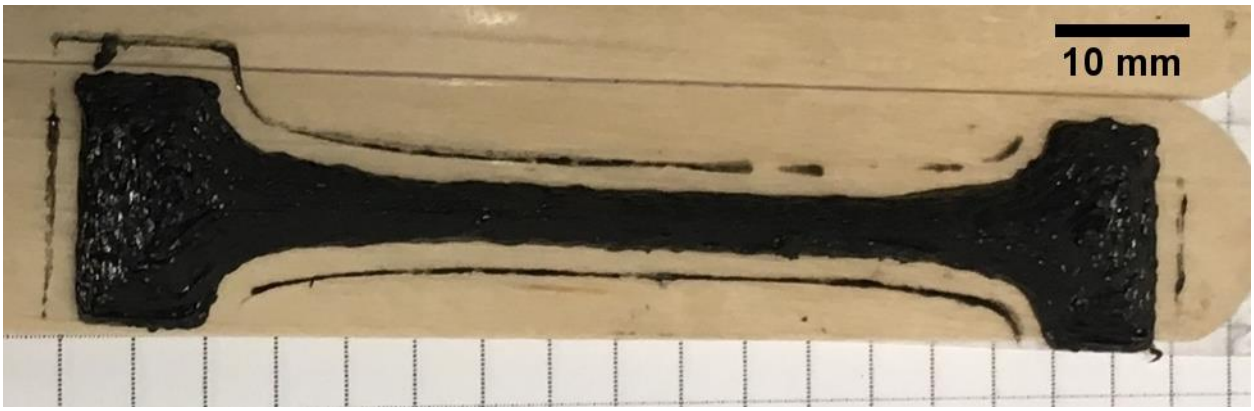

Figure E-1. An 80 mm long dogbone printed with 60 wt.% carbon fiber and polysiloxane. The height is 6.25 mm.

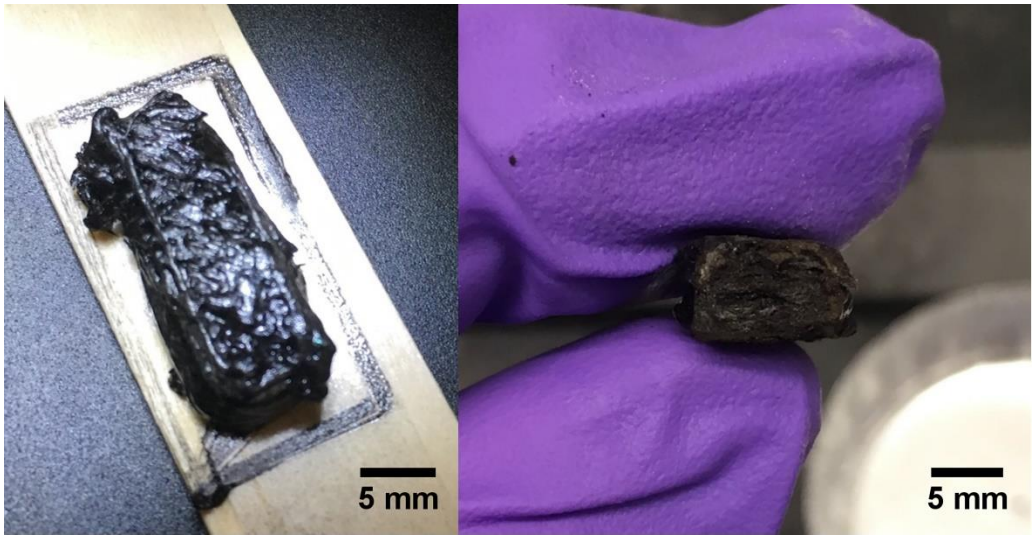

Figure E-2. (Left) Deformed 50 wt.% carbon fiber and polysiloxane 3D printed structure that is 20 mm long. (Right) The cross-section of the pyrolyzed structure has reasonable density (right).

Even though the rotational mixer was able to make mixtures with up to 60 wt.% carbon fiber, there were times when the polymer would separate from the fiber during the printing process (likely due to tangled fibers clogging the nozzle). Therefore, part of the carbon fiber content was substituted with 10 wt.% carbon black (LA108 Spectrum) in the final mixture to stiffen the polymer. The final mixture composed of 45 wt. % of carbon fiber and 10 wt.% carbon black which had a total carbon content of 55 wt.% (43.2 vol.%). The carbon fiber was sieved below 106 µm to remove large clumps. A resonant acoustic mixer was used to reduce the mix time of the 40 g batches. Each batch was mixed for a total of three cycles of 3 minutes at 80 g's.

Methods

Since the equipment needed to fully pyrolyze the printed samples was in a different facility, it was important to thermoset the samples so that they would not deform during transportation. This was easily achieved by heating a vacuum oven filled with argon to 180 °C. The argon was not actively cycled to remove generated products during the thermoset process. Although this is typically done during pyrolysis to prevent oxidation, that lack of cycling did not visually affect the quality of the thermoset components. Since the heating and cooling rates were not controllable in the vacuum oven, they were approximated as 1.03 °C/min and 0.55 °C/min. A Centorr Furnace in another facility was used to pyrolyze the thermoset samples according to a suggested schedule

from the manufacturer (see Table E-1). A constant flow of argon was used to prevent oxidation (and weakening) of the samples.

Table E- 1. Pyrolysis cycle [66].

Temperature (°C)	**Rate (°C/min)**
25 - 650	1
650 - 875[a]	2
875	0[b]
875 - 300	-1

[a] Minimum of 850 °C for pyrolysis.
[b] Held for 120 minutes.

In order to understand the mass loss and heat flow of the mixture, 15.52 mg of material was heated from room temperature to 1000 °C at a rate of 10 °C/min in a Q600 DSC-TGA machine (TA Instruments). 20/80 vol.% O_2/Ar gas was constantly flowed through the system at a rate of 100 mL/min.

The determination of flexural strength required manufacturing C bars (8 x 90 x 6 mm) in accordance with ASTM standard C1161-18. The fresh 55 wt.% carbon/polysiloxane mixture was thermoset in a polytetrafluoroethylene mold. Uneven surfaces were sanded before the C bars were then pyrolyzed. An ESM 1500 machine (Mark 10) with a precision of 0.5 N was used to test four samples via a 3 point bending configuration as seen in Figure E-3.

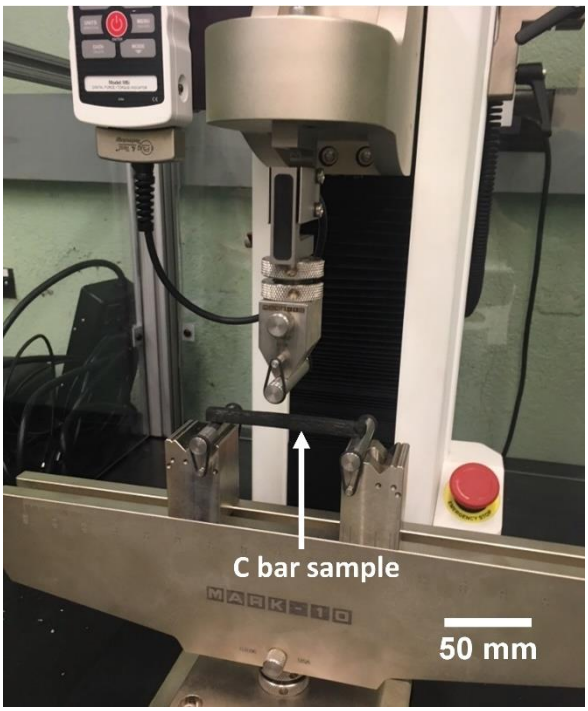

Figure E-3. 55 wt.% carbon/SiOC composite C bar setup configured for 3 point bending tests.

Adhesion between the carbon fiber and SiOC ceramic matrix was visually inspected with a HIROX KH-8700. The samples were illuminated on the top surface. A propane torch (TS4000 Bernzomatic) was applied 8 cm from the surface of a broken C bar for 1 minute to asses heat resistance. The mass loss from the process was measured and reported.

A modified Monoprice Select Mini 3D VAP with similar specifications to the printer used in Chapter 3 was used to deposit material. The same syringes were also used to hold the mixture. A reservoir pressure of 0.34 MPa was applied to the barrel and was managed by a DX-250 (Metcal) dispenser to prevent rapid changes in pressure that would affect the flow. The VAP system operated at a 24 kHz frequency and the material was deposited onto a borosilicate plate or a microscope slide.

Mass Loss

Many ceramic precursors lose mass during pyrolysis since it is a necessary process to remove excess polymer in order to obtain the ceramic backbone. Polysiloxane precursors have been reported to lose between 12 to 30 % of their original mass [78]. To improve the density, it is possible to reinfiltrate low viscosity precursors into a porous component and to then pyrolyze the

part again until the density is satisfactory. However, this could be a costly process that may not be necessary for the application in mind. In addition, reinforcing particles or fibers can reduce the overall mass loss and shrinkage. Figure E-4 shows the mass loss curve of the 55 wt.% carbon content mixture. Approximately 5% of material is consumed at a constant rate up until 500 °C. Between 500 and 600 °C, there is a steep descent where an additional 7% mass loss occurs. After this range, the mass loss consumption rate slows and above 750 °C, hardly any more mass is lost. The total mass loss from room temperature to 1000 °C is 14.25%.

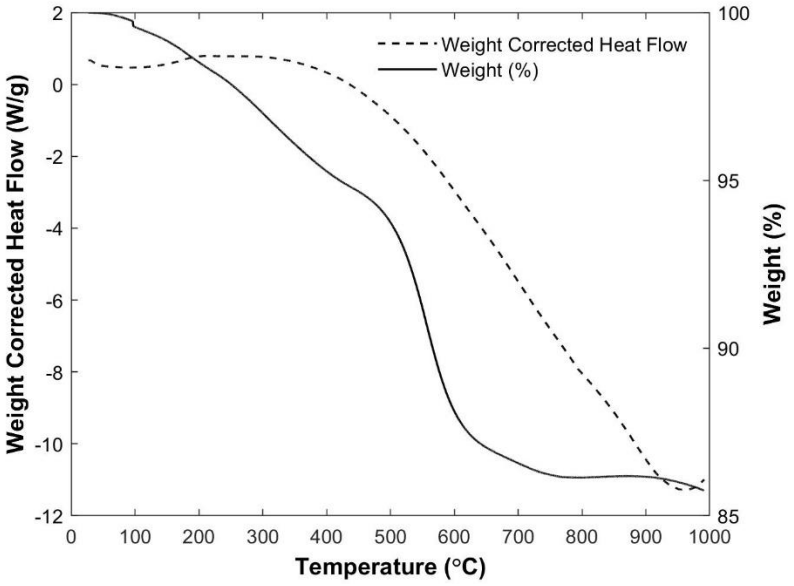

Figure E-4. DSC-TGA of 45 wt.% carbon fiber, 10 wt.% carbon black, and 45 wt.% precursor. The heating rate is 10 °C/min [66].

Flexural strength

The mechanical strength of an ablative material should not be neglected because in addition to high temperatures and volatile products, the inner flow of a nozzle for a SRM will experience the force of impinging condensed products. Although there are several types of strength measurements (i.e. tensile/compressive, flexural, and shear), flexural strength is a much more common metric for ceramics. In addition, continuous fibers are not used which eliminates the need for tensile testing. The measured flexural strength of the pyrolyzed C bars was 11 ± 1 MPa, which is low compared to other common ablative materials such as graphite (45 MPa) [79] and continuous fiber reinforced composites [80]. This is because the C bars are porous as seen in Figure E-5. The microstructure

of the porosity likely influences the fracture modes seen in Figure E-6. However, tailoring the carbon content (carbon fiber to carbon black ratio) and the addition of an extra cycle of reinfiltration and pyrolysis will affect the flexural strength.

Figure E-5. Pyrolyzed C bar for flexural strength testing [66].

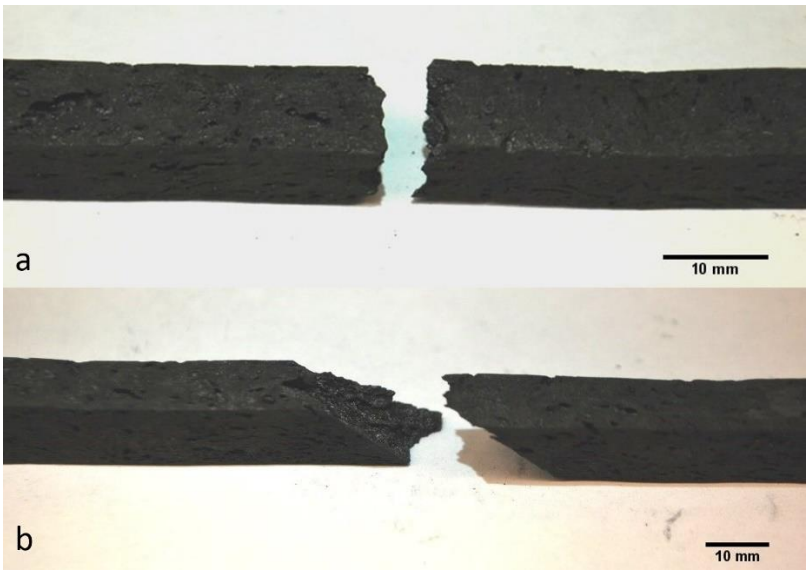

Figure E-6. Fracture modes of C bars [66].

Another method to improve flexural strength is to alter the pyrolysis schedule. At temperatures above 1100 °C, SiOC can separate into SiC and SiO_2 [81, 82]. The general reaction is

$$Si_xO_yC_z \xrightarrow{T>1000^\circ C} aSiC + bSiO_2 + C, \quad (4)$$

It is possible that with the addition of carbon black, the degree of SiC formation could increase further. However, one must consider the effect of silica phases in the ceramic matrix, which could

also weaken the final part. An area of future work would be to test the effect of carbon content and maximum pyrolysis temperature on SiC formation. In addition, one could choose to reinfiltrate the component with polycarbosilane, a low viscosity direct precursor to SiC, to tailor the microstructure further.

Microstructure

Microscopic imaging was useful for observing the microstructure of the porosity on the surface of the C bars which can be seen in Figure E-7(a). It appears that sanding the surface could have damaged some fibers, but the porosity is internal and a result of mass loss during pyrolysis. Figure E-7(b) shows some degree of bonding between the fibers and the SiOC. An adequate cleaving method is needed to cut the surface without cracking the porous ceramic so that the fiber-ceramic bonding can be analyzed better. Typically, SEM imaging is used to inspect fiber-matrix interfaces. In general, improved density of the ceramic matrix is likely needed to improve overall bonding between the fiber and SiOC matrix, which will likely improve the flexural strength.

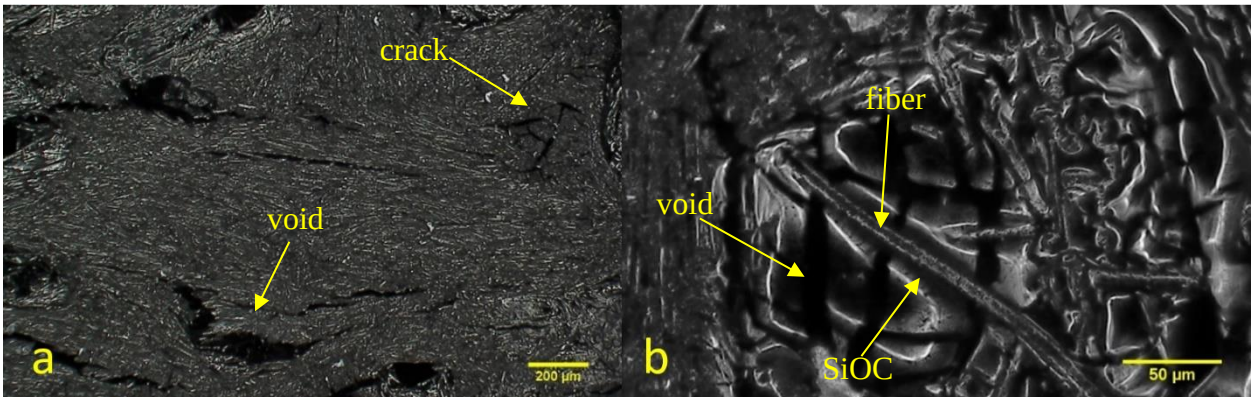

Figure E-7. (a) Polished surface of pyrolyzed material and (b) SiOC bonding to carbon fibers [66].

Heat resistance

Under high thermal stresses, some materials melt or crack. Although oxyacetylene torches are common for testing the erosion rates of ablative materials (ASTM E285), a simple propane torch was used to quickly vet this material. As seen in Figure E-8, there did not appear to be any change in size and damage to the sample. Only 4.52% mass was lost during this process. This simple test shows that this material is much more resistant to heat than printable carbon fiber reinforced filaments, so this material is likely a more viable material for SRM environments.

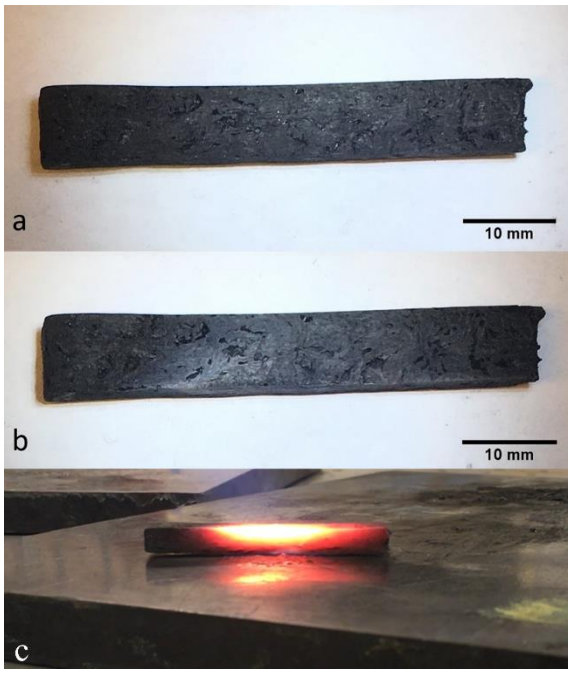

Figure E-8. (a) C bar before and (b) after propane torch test for 1 minute [66]. (c) The C bar during the propane test.

VAP

There were a few challenges to overcome in order to 3D print this material. The fibers would occasionally clog and then the polymer would dewet from the fibers. However, sieving the fibers to remove clumps and adding carbon black reduced the frequency of these issues. Figure E-8 shows successfully printed parts. When the printing parameters were optimized, the fibers appeared to be highly oriented with the flow and print path. Future work would involve quantifying the orientation of the fiber within the printed mixture.

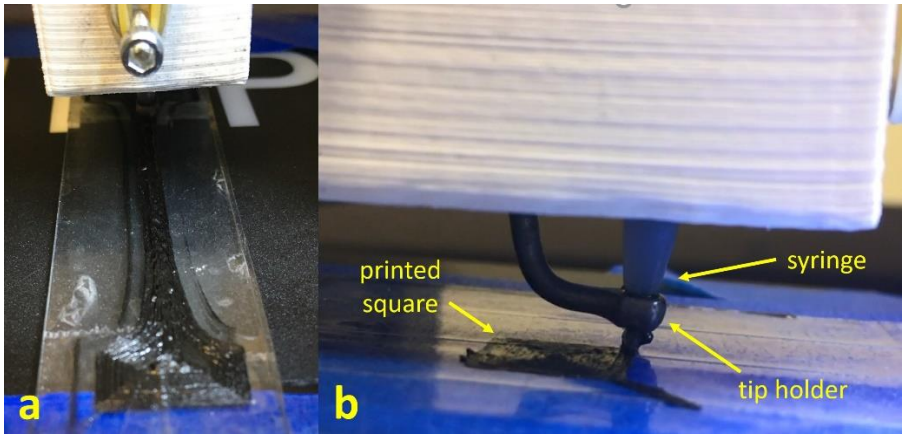

Figure E-9. (a) Examples of 3D printing a dogbone and (b) a square. The width of the microscopic slide is 25 mm and the width of the square is approximately 20 mm [66].

Conclusions

A mixture of high carbon content (up to 60 wt.%) and a SiOC precursor was additively manufactured using VAP. The heat resistance of the finalized product was promising and the flexural strength was acceptable for use in solid rocket nozzles. The fibers were oriented in paths that could not be achieved if traditional composite manufacturing methods, such as wet layup or injection molding, were used. The ability to orient carbon fiber more precisely increases the ability to control local mechanical and thermal properties within a printed part, which are of great importance in the design of a rocket nozzle where fiber orientation affects erosion rate.

Future work

It would be useful to investigate the ratio of carbon black to carbon fiber to understand its effect on rheological properties (printability) and mechanical properties. For example, the presence of carbon fiber made the mixture appear to be shear thickening, whereas a formulation with more particles could transition the mixture to shear thinning. It would be valuable to manufacture parts with manipulated print orientations to study their effect on erosion rate and flexural strength. An example of possible print orientations and expected heat flow paths can be seen in Figure E.10. Afterwards, small nozzles with varying internal print orientations should be tested to demonstrate the viability of 3D printed CMCs directly in a SRM exhaust and the effect of print orientation on erosion rate.

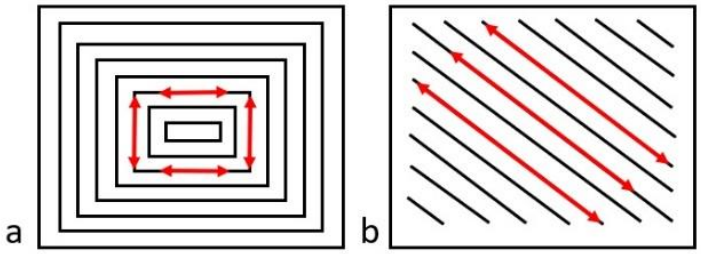

Figure E-10. How heat will likely flow through square panels 3D printed with fibers in (a) a concentric printing path and (b) a 45 degree rectilinear printing path.

APPENDIX F. NAWCWD CHINA LAKE SUMMER 2019

Thanks to the Combustion Science and Propulsion Research Division at NAWCWD China Lake, I was able to work on the Rocfire study in Chapter 5. With the help of Dr. Brian Bojko, I was able to learn how to use Rocfire and I was able to run studies on layered solid propellant. In addition, I was given a project by Dr. Clare Dennis to measure the melt layer of pure AP single crystals *in-situ* at pressure. Previous studies have been conducted on the burning rate of AP single crystals [83]. A melt layer was reported, but only based on quenched samples that were imaged in a SEM. Lately, a new pressure vessel configuration at Purdue has been used to allow a K2 lens to view the melt layer of AP single crystals at pressure. These results will be presented at the AIAA JP&E in August of 2020 and will provide important insight on the combustion of AP to the energetic materials community.

APPENDIX G. REACTIVE WIRE RESEARCH

Motivation

The research presented in this section is largely preliminary work for a different, yet related study on how reactive wires can be 3D printed into structures that can affect propellant combustion by increasing burning surface area [84]. The goal of the study in this section was to investigate the combustion of Al/PVDF wires (details on the manufacturing process in Reference [85]) that were embedded in windowed propellant at pressure. The hope was that the Al/PVDF would burn faster than the surrounding propellant and would therefore open up burning surface area. The Al/PVDF wires were of particular interest because they can be 3D printed into structures via FFF. Those structures can then be embedded into propellant in order to open up various dynamic port geometries while contributing energetically. One could also potentially 3D print the wires into 3D printed propellant in the future. A windowed propellant configuration that used in a previous study [86] was helpful for determining the viability of Al/PVDF in propellant.

The author wants to note that the subsequent study from another colleague involved tuning the reactivity of the Al/PVDF wires (by varying the particle size and the additive type) and investigating the combustion of 3D printed structures that were embedded into propellant [84]. In addition, they used an X-ray technique to visualize how the embedded components increased burning surface area within the propellant. The work presented in this chapter presents results at pressurized conditions, although the manufacturing technique was not completely refined which led to inconsistent results. The manufacturing and visualization processes were improved upon in Reference [84], but the propellant was burned in atmospheric conditions, so the results in this section can still provide insight on the role of 3D printable reactive wires in pressurized environments.

Manufacturing of windowed propellant with reactive wires

The propellant mixture used was 85 wt.% AP with a 4:1 CFR of 200 μm (Firefox) and 20 μm (ATK) AP. The binder formulation was 72.9 wt.% R-45M, 14.61 wt.% IDP, 0.99 wt.% Tepanol, and 11.5 wt.% Desmodur E-744. Propellant batches of 32 g were made via resonant acoustic mixing, which were then degassed for 10 min. The propellant was pressed into a Teflon mold with

casting dimensions of 95.06 x 25.45 mm. Sections of Al/PVDF filament were cut about 20 mm long and were slightly embedded into the propellant. Then, 3.3 mm thick polycarbonate windows (cut to 11 x 24 mm) were pressed on top as seen in Figure G-1. Adhesion between the window, wire, and propellant was difficult to achieve. This configuration led to some gaps around the wire, but this was an unavoidable issue with the configuration used. It was difficult to squeeze propellant into gaps created by a filament with a 1.75 mm diameter next to a flat surface. The wires (copper and Pyrofuze) used in a previous study were much thinner and the propellant was less viscous, so this was not an issue in that study [86].

Figure G-1. Embedded Al/PVDF filament in AP/HTPB with polycarbonate window in a Teflon mold. After curing, the propellant is cut into strands. The windows are approximately 11 x 24 mm.

In order to understand the effect of the window on the combustion of the propellant, baseline samples with no embedded propellant were burned at pressure in a Crawford bomb. A nitrogen environment was used. The burning rate curve and the pressure coefficient and exponent can be seen in Figure G-2. This data was not compared to the burning rate of propellant without a window, although previous studies have expressed concerns about the effect of the window on combustion [86]. If future research will use this configuration, then it would be useful to quantify the effect on the window which may not have been previously studied.

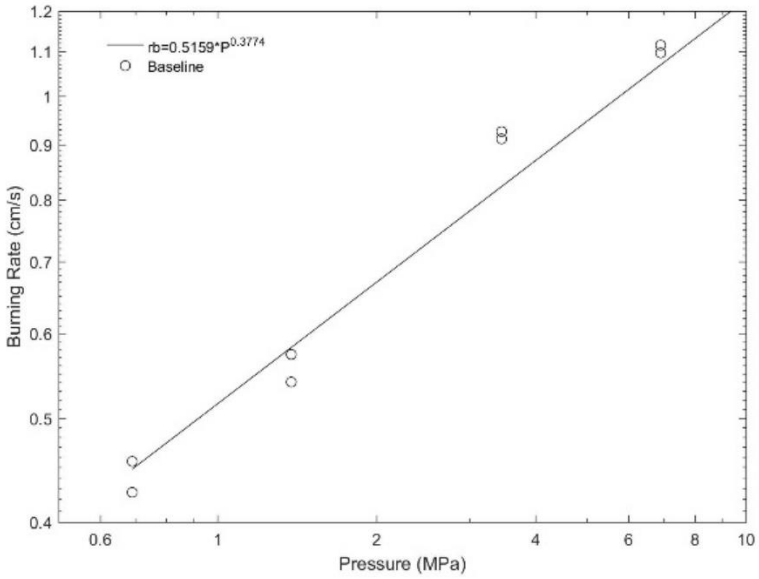

Figure G-2. Burning rate curve of baseline AP/HTPB propellant with a polycarbonate window and no embedded wire.

Combustion of reactive wires at pressure

Due to the unreliable method of embedding the wire into the propellant and against the window, varied results were observed during high pressure experiments. Essentially, when there were no significant gaps near the wire, the wire did not burn faster than the surrounding propellant as seen in Figures G-3, G-5, G-7, and G-9. When there was a gap, the flame spread quickly, ignited the wire, and then opened up burning surface area as seen in Figures G-4, G-6, and G-8. Occasionally, there would be only a short gap between the wire and the propellant. In that region, the surface area would open up, but then no further surface area would develop as seen in Figure G-10. The conductive (flat burning) and convective (erratic burning) behavior was seen at all of the pressures tested (1.38 to 10.34 MPa).

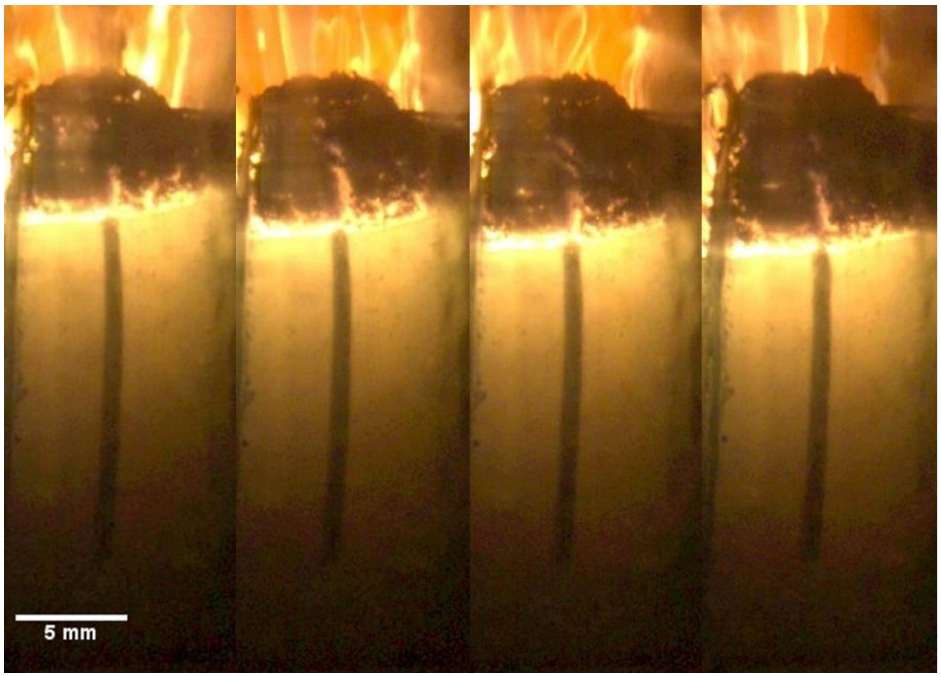

Figure G-3. Conductive burning of Al/PVDF wire embedded in AP/HTPB propellant at 1.38 MPa. There are 0.1 s between frames.

Figure G-4. Convective burning of Al/PVDF wire embedded in AP/HTPB propellant at 1.38 MPa. There are 0.1 s between frames.

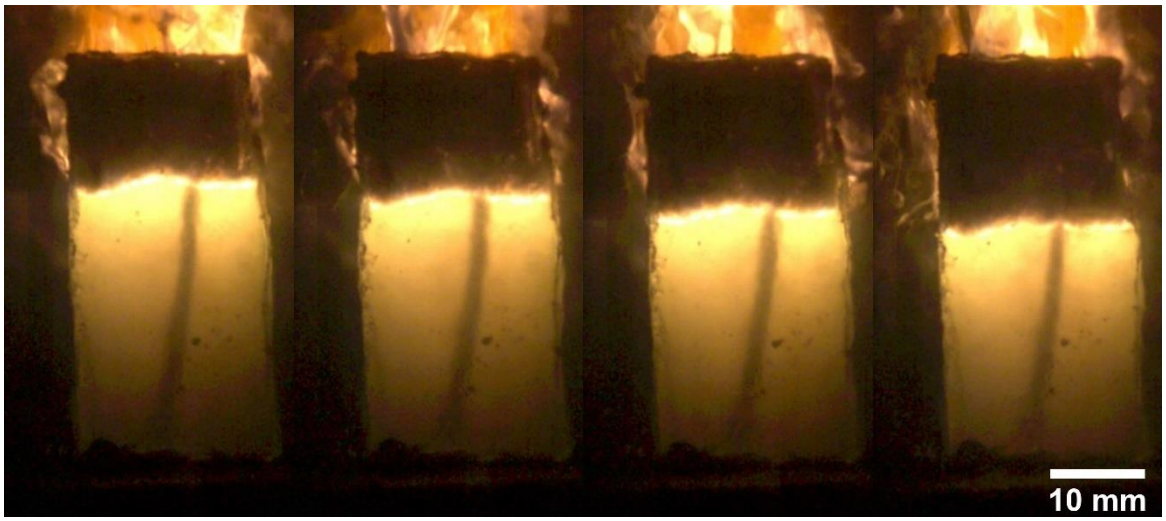

Figure G-5. Conductive burning of Al/PVDF wire embedded in AP/HTPB propellant at 3.45 MPa. There are 0.1 s between frames.

Figure G-6. Convective burning of Al/PVDF wire embedded in AP/HTPB propellant at 3.45 MPa. There are 0.1 s between frames.

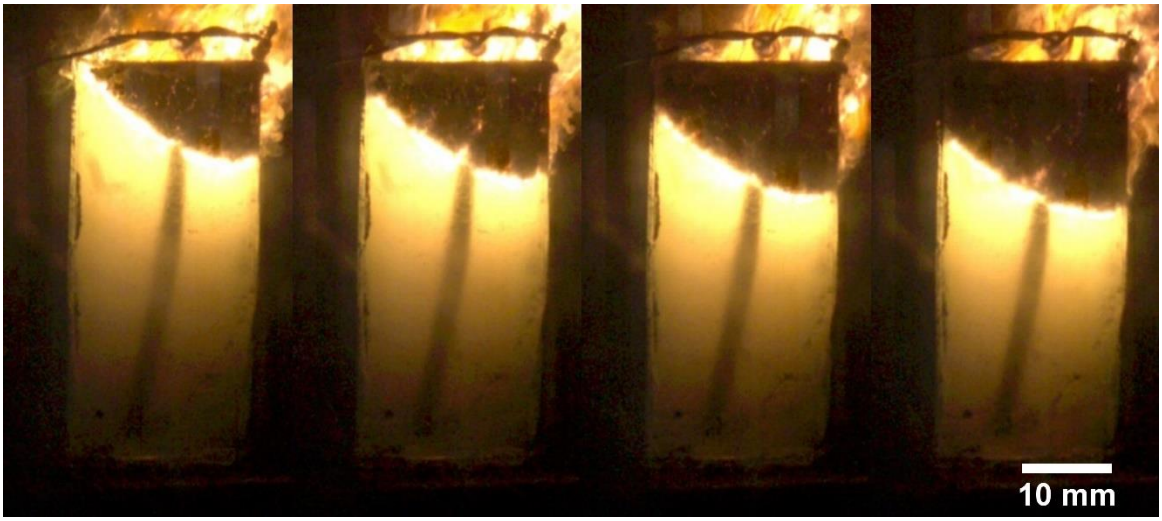

Figure G-7. Conductive burning of Al/PVDF wire embedded in AP/HTPB propellant at 6.89 MPa. There are 0.1 s between frames.

Figure G-8. Convective burning of Al/PVDF wire embedded in AP/HTPB propellant at 6.89 MPa. There are 0.1 s between frames.

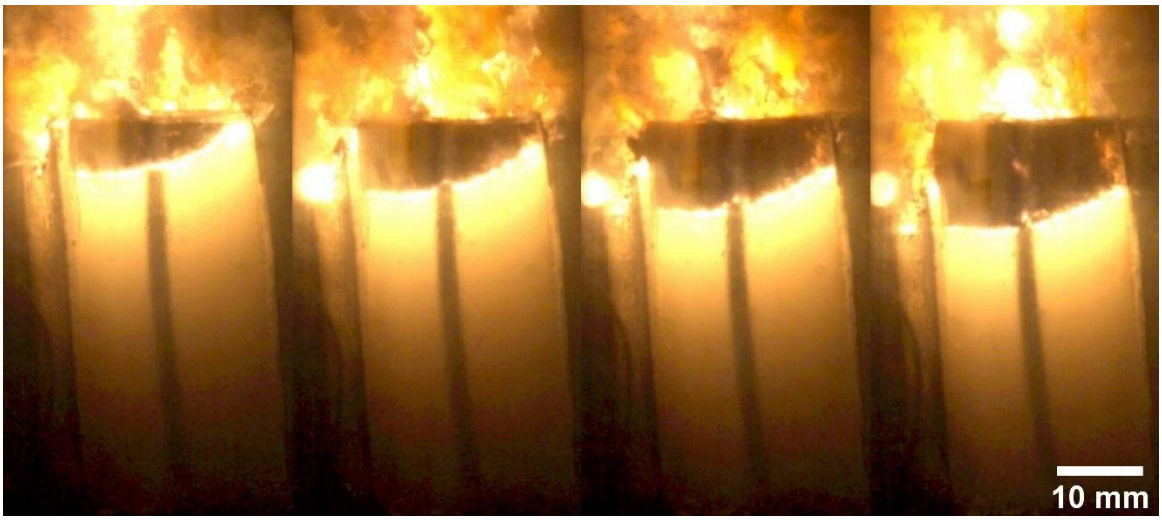

Figure G-9. Conductive burning of Al/PVDF wire embedded in AP/HTPB propellant at 10.34 MPa. There are 0.1 s between frames.

Figure G-10. Partial convective burning of Al/PVDF wire embedded in AP/HTPB propellant at 10.34 MPa. There are 0.1 s between frames.

Once the cause of the unrepeatable burning behavior was determined, further tests (in which the adhesion between the wire and the propellant was improved) showed that the Al/PVDF wire does not burn faster (in a conductive mode) than the surrounding propellant at pressure. However, if one intentionally adds a gap near the wire, convective burning can easily achieve the goal of quickly opening up burning surface area.

3D printed embedded components

The next step was to increase the cross-sectional area of the reactive wire since it was believed that the propellant was a heat sink for the wire during combustion. Therefore, the Al/PVDF filament was 3D printed (with the same process that was described in this Reference [85]) into strands of 2.4 x 2.4 x 20 mm. The 3D printed component and the new windowed propellant strands can be seen in Figure G-11.

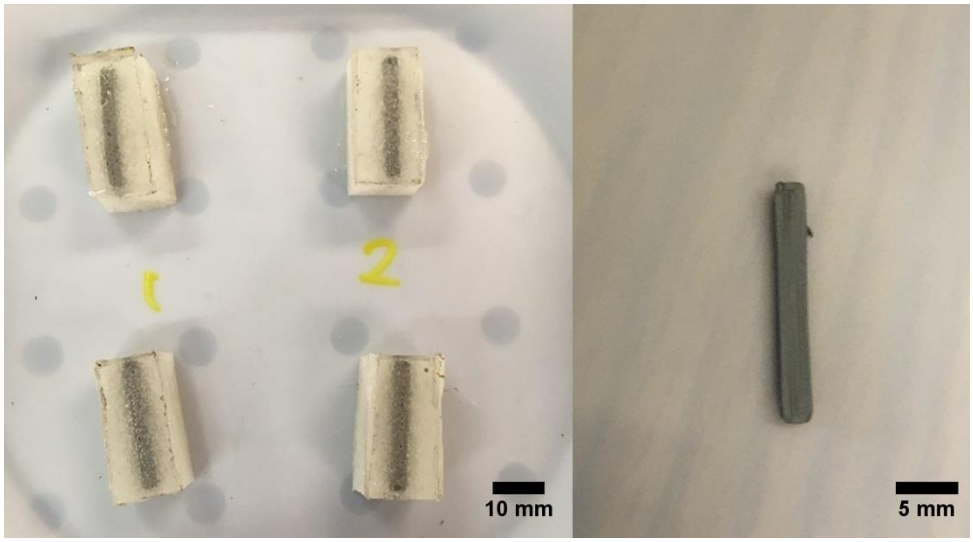

Figure G-11. (Left) Embedded additively manufactured 2.4 x 2.4 x 20 mm Al/PVDF structure in propellant that is pressed against the window and (right) additively manufactured Al/PVDF component.

Unfortunately, the 3D printed Al/PVDF components did not really achieve the desired result of faster combustion in a conductive mode. Figure G-12 shows an example of convective flame spread. It is unclear if there was a gap at the interface of the component and the propellant or if there was defect in the component itself. Other tests showed that when there was no gap, the Al/PVDF component still did not burn faster than the surrounding propellant.

Figure G-12. Convective burning of Al/PVDF printed component embedded in AP/HTPB propellant at 3.45 MPa. There are 0.1 s between frames.

Aluminized propellant with reactive wires

The next attempt was to embed reactive filaments into aluminized propellant (15 wt.% Al, 325 mesh) in order to reduce the degree of heat loss from the wire to the surrounding propellant. The strands can be seen in Figure G-13. Unfortunately, this was also an unsuccessful endeavor since the wires did not burn faster than the aluminized propellant at pressure.

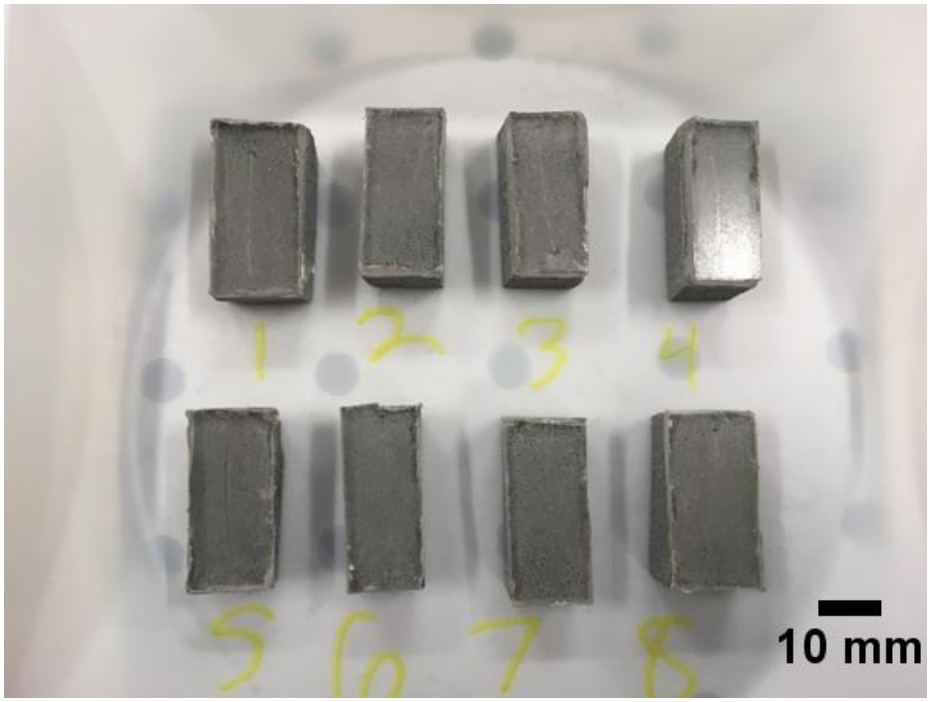

Figure G-13. Embedded additively manufactured Al/PVDF wire in aluminized (15 wt.% Al) propellant pressed against a window. The windows are approximately 11 x 24 mm.

Role of heat loss on wire combustion

It is believed that the embedded wires were not completely reacting in the propellant during conductive burning. This is based on a comparison of soot formation. When the wire is burning by itself in atmosphere, the is a 6 mm long reaction zone near the top that snakes downwards as seen in Figure G-14. The reaction zone produces a lot of flaky soot that breaks apart and is messy. When the wire burns in propellant, the soot is thinner and continuous, which is not a property of the fully combusted soot. Therefore, it is likely that the wire is just decomposing when it conductively burns in the propellant. When the wire convectively burns in the propellant, the fully combusted flaky soot is seen.

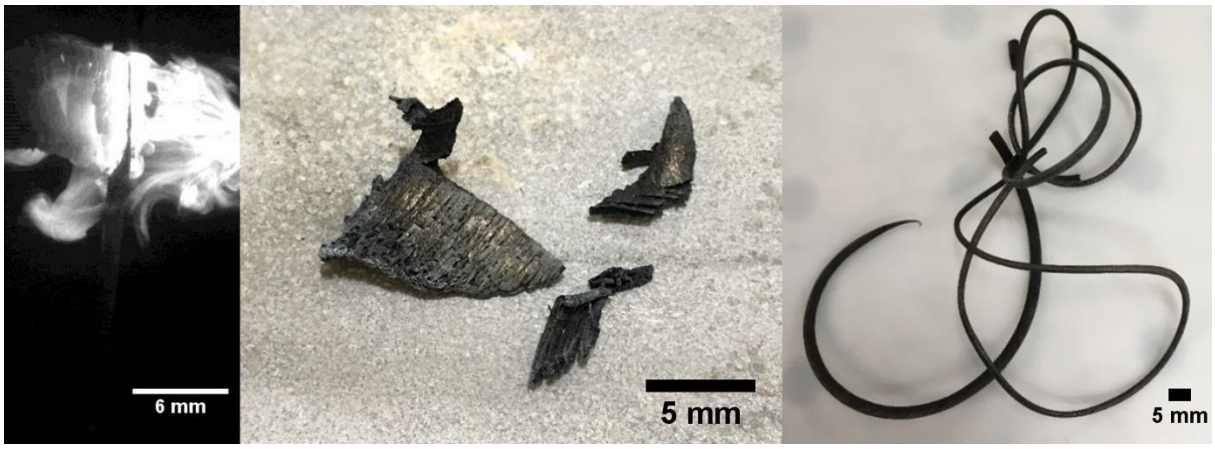

Figure G-14. (Left) Image of Al/PVDF filament combustion, (middle) soot formation after full combustion, and (right) soot formation after incomplete combustion.

To test the idea that the propellant is a heat sink to the wire, a windowed propellant was made with a longer wire that protruded well above the surface. The wire was ignited and in Figure G-15, it is clear that the wire burns fast when it is not surrounded by propellant and slows down considerably when it reaches the propellant surface. This test was conducted at atmospheric conditions.

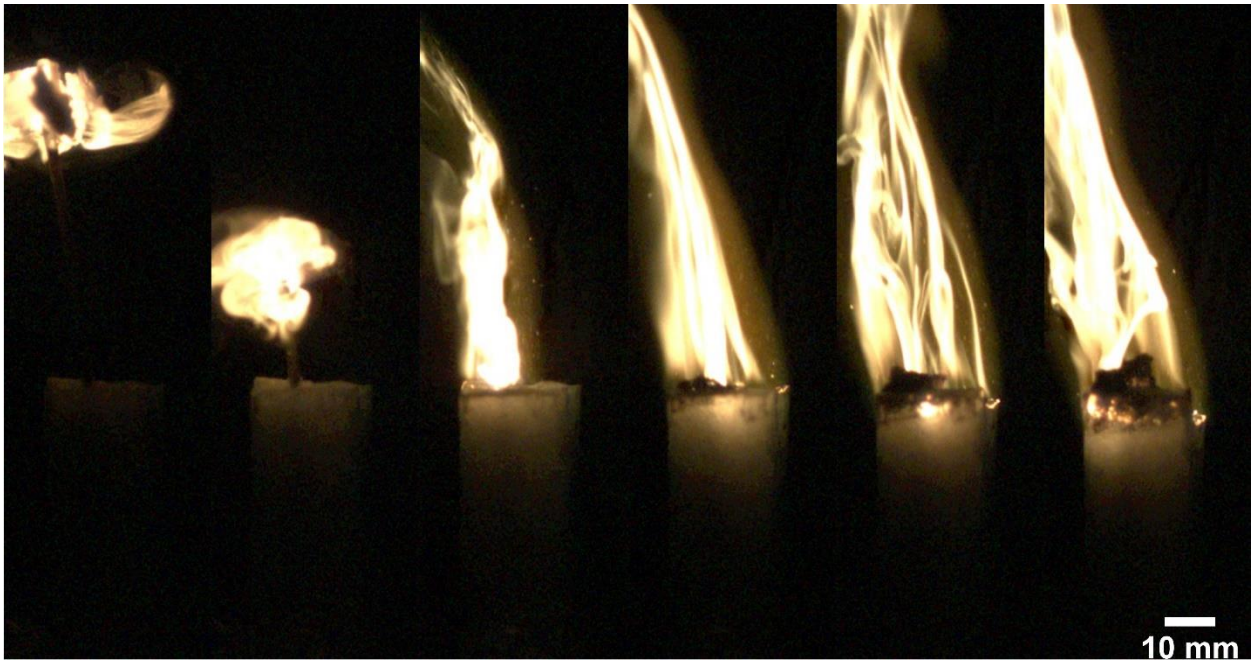

Figure G-15. Combustion sequence of a protruding Al/PVDF wire embedded into an AP/HTPB propellant strand at atmospheric conditions. The wire burns fast above the surface, but slows down when it ignites the propellant surface. There is 1 s between frames.

Although the combustion of Al/PVDF wires in windowed propellant was unreliable in this study, a lot was learned about how to successfully create reactive wires that would open up burning surface area at pressure. It was clear that the Al/PVDF would not burn fast enough conductively, but that led to a subsequent study on how to improve the reactivity of 3D printable reactive wires [84]. In addition, these faster burning filaments were 3D printed into various geometric shapes and were embedded into the center of propellant strands, which dramatically improved the adhesion of the wires to the propellant. By using an X-ray technique, the combustion of the reactive wires and 3D printed components that were embedded into the propellant was observed [84]. However, the preliminary work in this chapter shows the behavior of reactive Al/PVDF wires in windowed propellant at pressure, whereas the propellant with embedded components in Reference [84] was burned at atmospheric conditions. In the near future, it seems that my colleague will be able to integrate the X-ray technique into a pressure vessel so that the combustion of faster burning reactive wires and 3D printed structures in propellant can be properly investigated.

Future work

The next goal is to be able to additively manufacture reactive wires and propellant simultaneously within the same part. Adhesion between propellant and PVDF based reactive wires is challenging because of the chemically resistant nature of PVDF. However, an initial attempt was made to see if Al/PVDF could be 3D printed onto a slice of cured propellant. The Al/PVDF was printed into the slice as seen in Figure G-16. The temperature of the print bed was 120 °C and the print head was 230 °C. The propellant did not degrade and the small Al/PVDF square adhered to the propellant, likely because the heat of the deposited Al/PVDF melted the propellant binder locally. Although more work needs to be done to integrate VAP with FFF, those techniques have been recently incorporated into a modified printer [54]. In addition, a mini adhesion study on thermoplastic filaments with HTPB was conducted to identify a path towards additively manufacturing components made of dissimilar materials. Not only can this work be applied to reactive wires, it can also be applied to manufacturing propellants with thermoplastic casings to simplify the process of mounting grains into a SRM.

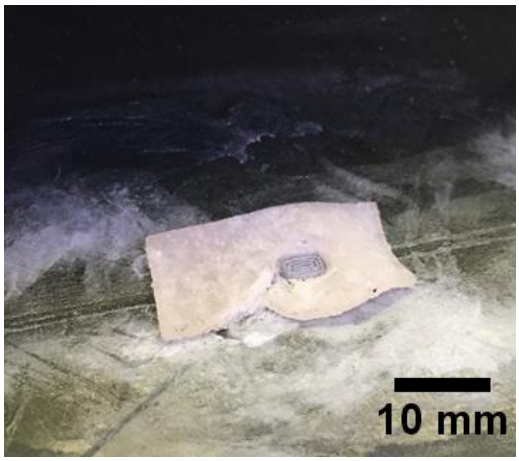

Figure G-16. Image of 3D printed Al/PVDF square on a slice of AP/HTPB propellant. The two materials stick together even when lightly pulled.

APPENDIX H. PROPELLANT FORMULATION AND PROCESSING PARAMETERS

Motivation

After a comparison between the microstructure of 3D printed HTPB and UV-curable propellants showed a large amount of porosity in the HTPB propellant (see Chapter 3), a reevaluation of the binder formulation was needed since Tepanol induced a significant amount of porosity [37]. Tepanol is a bonding agent that can improve the density of propellant with extremely high solids loadings. However, it is known to off gas ammonia, so propellant mixtures with this additive are typically mixed for hours under vacuum. Given that the propellant mixture in the additive study was not mixed under vacuum and was only degassed for 5 min after resonant acoustic mixing, it seemed that the mixing process was not able to sufficiently remove the chemically induced voids.

In addition, there is also an inherent challenge when trying to produce high density propellant that is made in small batches. It has been shown that the smaller the propellant batch, the lower the density, which ultimately affects the burning rate [87]. However, the purpose of this mini study was to improve the density of propellant made in small batches since it would be wasteful to make large batches when only a small amount of propellant is needed for the 3D printing process used in this dissertation.

Effect of formulation and mixing method on propellant microstructure

The solids loading and CFR of the AP used were the same as what were used in Chapter 3.2. The only variables that were changed were the binder formulation, degas time, and the mixing method. The density was estimated by quantifying the percentage of two dimensional voids seen in a micro-CT cross-sectional image using ImageJ. This percentage was then multiplied by the theoretical density to obtain an estimate of the actual density. This is not the ideal method to analyze volume since it reduces the dimension of the measurement. However, micro-CT analysis (the same type that was used in [37]) was helpful in characterizing the microstructure which can be seen in Figures H-1 and H-2. It is important to note that smaller, dispersed voids are far more desirable than interconnected porosity or large voids.

The propellant in Figure H-1 was mixed via resonant acoustic mixing and cast into pipets. The binder formulations can be found in Table H-1. The propellant with a R-45M and IPDI binder that was degassed for 5 min showed large, but few voids. The propellant with the R-45M, IDP, IPDI, and Tepanol binder that was degassed for 5 min (image taken from Figure 3-6 and from source [37]) had voids that were a similar size, but more of them. The propellant with the R-45M, IPDI, and IDP binder that was degassed for 5 min had more desirable properties since the voids were small and dispersed. The propellant that with the R-45M, IDP, IPDI, and Tepanol binder that was degassed for an hour also had desirable properties. However, adding an extra hour to a propellant printing routine was not economical when the similar results could be produced in less time with an alternate method. In addition, 3D printing propellant with a HTPB binder is a time sensitive process and it is important to print propellant within the optimal time frame or the viscosity will vary too much.

Table H-1. The binder formulations used in propellant microstructure analysis.

Binder Ingredient	**Formulation 1 wt.%**	**Formulation 2 wt.%**	**Formulation 3 wt.% (see Section 3.2)**
R-45M	91.96	77.04	75.25
IDP	0	15.05	15.05
IPDI	8.04	7.91	8.27
Tepanol	0	0	1.53

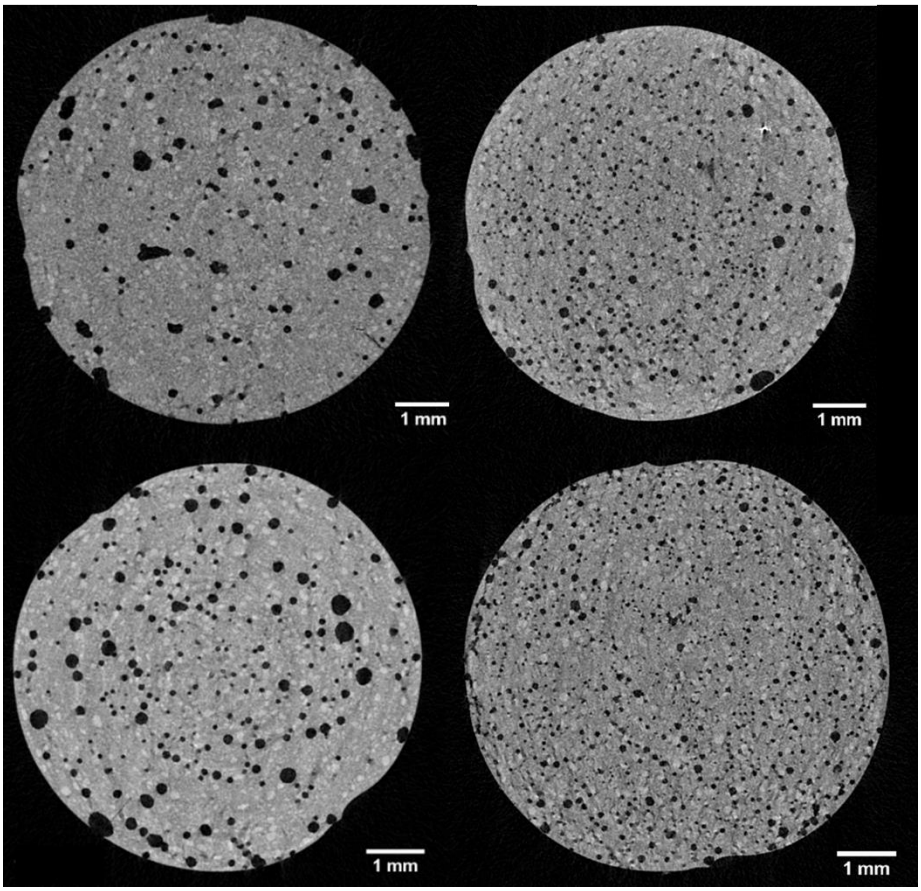

Figure H-1. (Top left) Micro-CT image of propellant with the R45M and IPDI binder mixed without vacuum with a density of 1.62 g/cc. (Top right) Micro-CT image of propellant with the R45M, IPDI, and IDP binder mixed without vacuum with a density of 1.62 g/cc. (Bottom left) Micro-CT image of propellant with the R45M, IPDI, IDP, and Tepanol binder that was degassed for 5 min after mixing with a density of 1.56 g/cc [37]. (Bottom right) Micro-CT image of propellant with the R45M, IPDI, IDP, and Tepanol binder that was degassed 1 hr after mixing with a density of 1.54 g/cc. The theoretical density is 1.68 g/cc and all of the propellants in this figure were mixed via resonant acoustic mixing.

Figure H-2 shows the micro-CT images of the propellant mixed in the Flacktek. The propellant binder used is R45M, IPDI, IDP and the mixture was not degassed. Although the microstructure was highly desireable, the Flacktek mixer was located in a different laboratory on the other side of campus. The biggest issue was that at least an extra hour was needed to transport and mix the propellant in this alternate location. Therefore, the easiest solution was to use the R45M, IPDI, IDP binder in the Resodyn to save time and to produce reasonable results. However, transitioning from a Resodyn to a Flacktek mixer at Zucrow is highly recommended to improve the microstructure of future propellant mixtures.

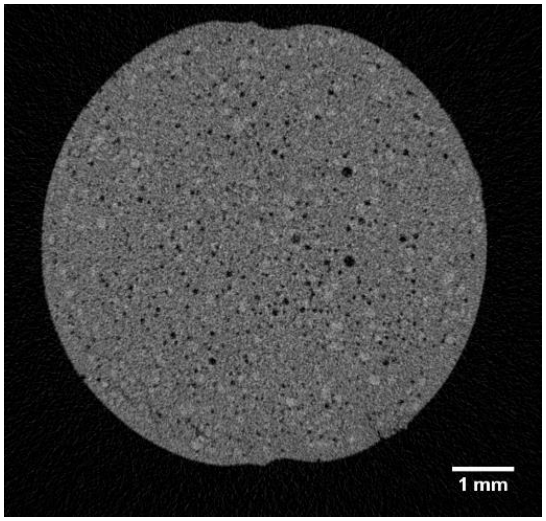

Figure H-2. Micro-CT image of propellant with the R45M, IPDI, IDP binder mixed with the Flacktek without degassing afterwards with a 1.62 g/cc density. The theoretical density of the propellant is 1.68 g/cc.

Figure H-3 shows the comparison of fresh propellant mixed with a Flacktek and a Resodyn. The Flacktek mixer involves dual asymmetric centrifugal mixing whereas resonant acoustic mixing (Resodyn) involves fast vibration up and down. The different processes produce very different propellant mixtures. The propellant that was mixed in the Flacktek was subject to multiple cycles of active mixing at 1500 RPM for 30 s and a rest period for 30 s. The Flacktek propellant mixture was softer to the touch than the Resodyn propellant. Fully mixed propellant made in a Resodyn forms into a ball unless there is not enough binder to fully wet the particles whereas the Flacktek creates an annulus shape.

Figure H-3. Comparison of fresh propellant mixtures made via (left) Flacktek and (right) Resodyn mixers.

Additional microstructure analysis

While the micro-CT in the CP-3 lab at Purdue University was widely available, a few propellant samples were inspected and the images of interest are included here. The microstructure of propellant that was cast in the open mold used in the reactive wire study and cut with a razor blade can be seen in Figure H-4. It is clear that there is a lot of interconnected porosity which naturally can lead to convective burning at high pressure. This porous structure could be a result of the open (unconstrained) top surface in the mold and/or the blade cutting the material.

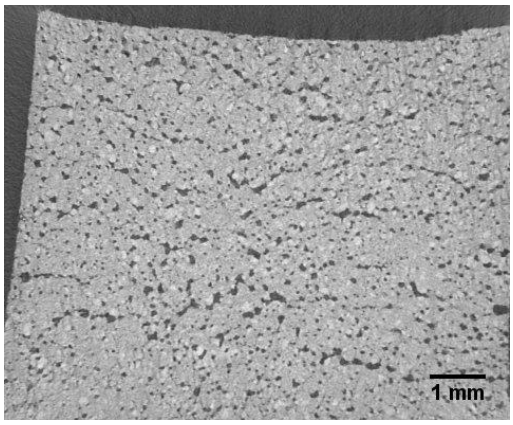

Figure H-4. Micro-CT image of a cast strand of AP/HTPB cured in an open mold (refer to Appendix G for details) that was cut with a razor blade.

Although most of the strands 3D printed in the Chapter 3 study were made successfully, not all strands were perfect. Figure H-5 shows the cross-section of a defective strand. It is clear that in the top layers, the propellant was overfilled and in the bottom layers, it was underfilled. The underfilling lead to connected porosity and cracking. The over and under extrusion was mostly a function of propellant viscosity which varied over time. The VAP parameters have to be adjusted over time to compensate.

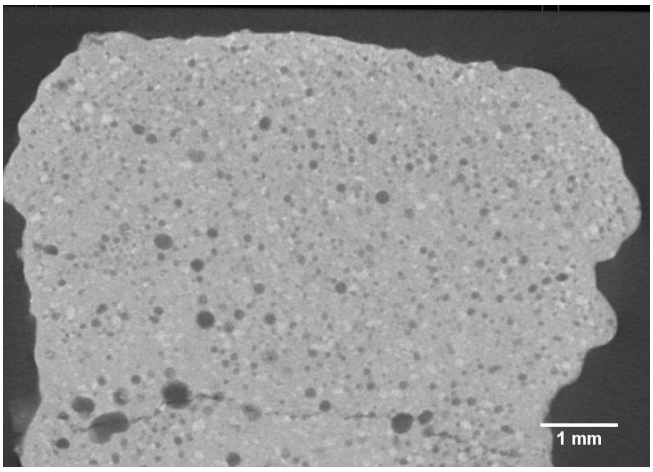

Figure H-5. Micro-CT image of 3D printed AP/HTPB strand with varying print quality (over extruded on top, under on the bottom).

Some micro-CT images were taken of old propellant from a prior study (see Reference [88]) in order to further understand the role of Tepanol in the formation of porosity. Those cross-sectional images can be seen in Figure H-6. The solids loading was 80 wt.% AP with varying CFR ratios of 400 μm and 20 μm AP. The binder formulation was 14.58 wt.% R45-M (Firefox Enterprises), 0.20 wt.% Tepanol HX-878 (3 M Corporation), 2.92 wt.% IDP (Rocket Motor Components), and 2.30 wt.% Desmodur E744 (Bayer Corporation). The propellant was handmixed and cured at room temperature for a week according to the study. Although the solids loading is lower, there is still a lot of porosity likely from the Tepanol or potentially from hand mixing. It is also interesting to see the distribution of the 400 μm AP with in the strand, which is not always uniform.

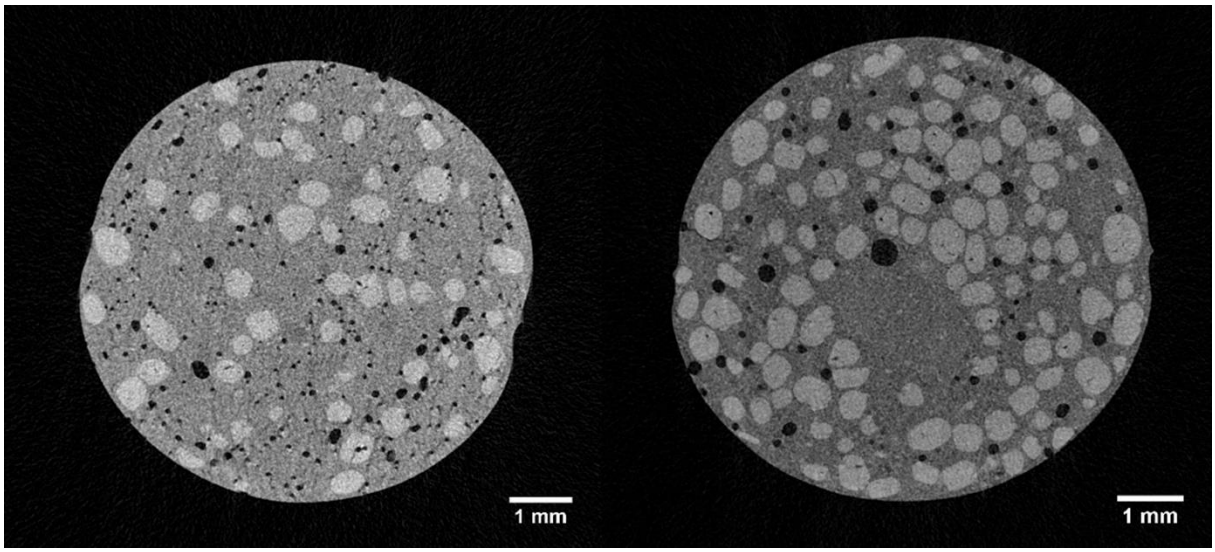

Figure H-6. Micro-CT images of propellant from a previous study [88] with 80 wt.% solids loading and (left) 1:4 CFR and (right) 1:1 CFR with 400 and 20 μm AP. The density of each strand is 1.56 g/cc compared to the theoretical value of 1.62 g/cc.

APPENDIX I. MICRO-EXPLOSIONS OF PROPELLANT WITH AN AL/ZR ADDITIVE

Motivation

In prior work, there have been extensive studies on the effect of an aluminum lithium alloy [89] and magnesium/zirconium additives [90] in solid propellants in order to induce microexplosions near the propellant surface to reduce the size of burning aluminum agglomerates. Following this vein of research, this section includes results on propellant with an aluminum zirconium additive (3Al:Zr) developed by the Weihs group from John Hopkins University [91].

Formulation

A propellant with a solids loading of 88 wt.% was made with the formulation seen in Table I-1. The binder formulation is in Table I-2. The propellant mixture was hand mixed before being mixed in the Resodyn for 5 minutes at 80 g's. The propellant was then degassed for 15 min, cast into pipets, and cured for 2 weeks at 60 °C.

Table I-1. 3Al:Zr propellant formulation by wt.%.

Propellant Ingredient	**Wt.%**
3Al:Zr	15%
200 μm AP	58.40%
20 μm AP	14.60%
Binder	12%

Table I-2. Binder formulation by wt.%.

Binder Ingredient	**Wt.%**
HTPB	75.25%
Tepanol	1.43%
IDP	15.05%
IDPI	8.27%

High pressure combustion

The burning rate of the propellant was tested at 1.38, 2.76, 4.14, 5.12, and 6.89 MPa in a Crawford bomb pressure vessel filled with nitrogen. Some examples of the combustion at various pressures can be seen in Figure I-1. The burning rate curve (with the pressure exponent and coefficient according to St. Robert's law) can be seen in Figure I-2.

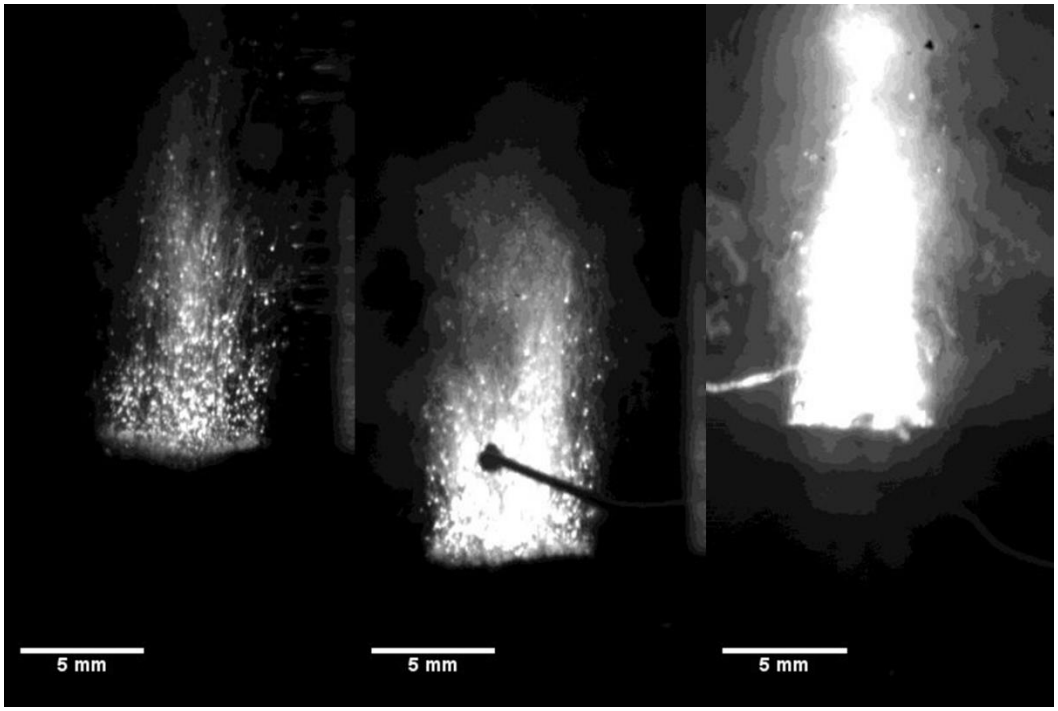

Figure I-1. Combustion of a propellant strand with 15 wt.% 3Al:Zr additive at (left) 1.38 MPa, (middle) 2.76 MPa, and (right) 6.89 MPa.

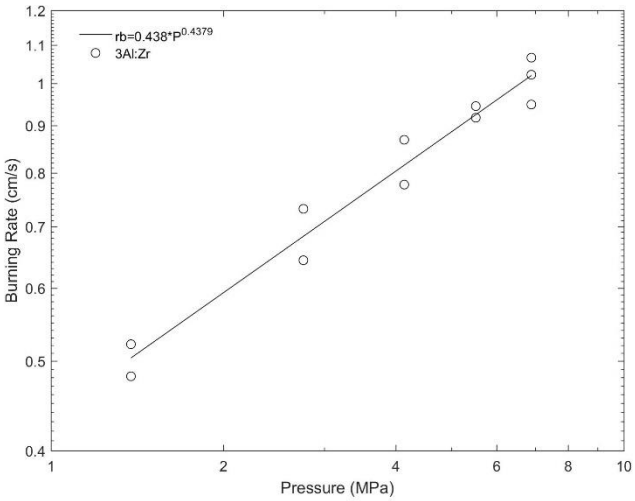

Figure I-2. Burning rate curve of propellant with 3Al:Zr additive.

In addition to obtaining the burning rate curve, combusting particles were quenched on a 1 in diameter glass disk (Etsy) using a particle capturing configuration inside of a pressure vessel (for details on the test configuration, see Reference [61]). The particles were captured at two pressures and can be seen in Figure I-3. Due to the presence of a lot of extremely fine particles, it was difficult to obtain a realistic distribution of quenched particles. However, the approximate size of the largest agglomerates is estimated to be about 50-100 μm based on visual inspection. The particle sizes seem similar at these two pressures.

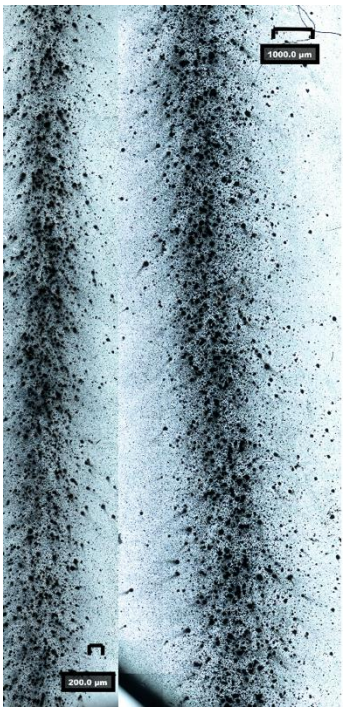

Figure I-3. Images of quenched particles from propellant with 3Al:Zr additive on glass disks at (left) 3.45 MPa and (right) 6.89 MPa.

Atmospheric combustion

In addition to high pressure tests, the microexplosions of the propellant were examined at the surface. Using a K2 lens configuration at atmospheric conditions [89], it was found that there were no microexplosions near the surface as seen in Figure I-4. However, when the burning propellant was imaged further away from the surface (without the K2 lens), microexplosions would occasionally occur far above the surface as seen in Figure I-5. The explosions happened about 24 mm above the surface (the diameter of the strand is 6 mm for scale). This work was not pursued further because it was decided that the microexplosions were occurring too far away from the surface.

Figure I-4. Near surface combustion of propellant with the 3Al:Zr additive at atmospheric conditions. There is 0.1 ms between the frames and no surface reactions are seen.

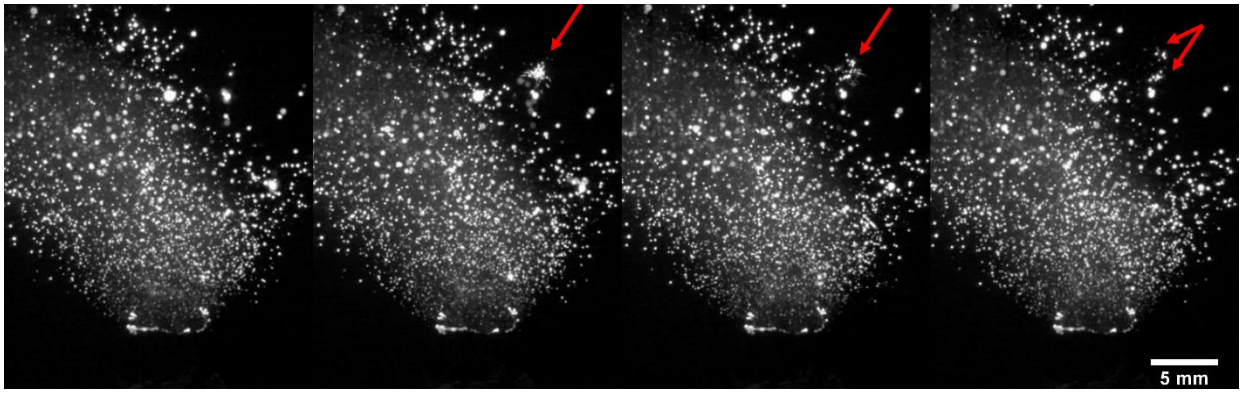

Figure I-5. Microexplosions occur about 24 mm above the surface of the propellant with the 3Al:Zr additive. There are 0.1 ms between the frames and the combustion occurs at atmospheric conditions.

REFERENCES

[1] C. W. Hull, "Apparatus for Production of Three-Dimensional Objects by Stereolithography," 3/11/1986.

[2] S. S. Crump, "Apparatus and Method for Creating Three-Dimensional Objects," 6/9/1992.

[3] "Solid Rocket Motors." https://engineering.purdue.edu/~propulsi/propulsion/rockets/solids.html (accessed 3/26, 2019).

[4] G. P. Sutton and O. Biblarz, "Rocket Propulsion Elements," John Wiley & Sons, 2001.

[5] R. Muthiah, V. N. Krishnamurthy, and B. R. Gupta, "Rheology of HTPB Propellant. I. Effect of Solid Loading, Oxidizer Particle Size, and Aluminum Content," *Journal of Applied Polymer Science*, vol. 44, no. 11, pp. 2043-2052, 1992, doi: 10.1002/app.1992.070441120.

[6] C. Erişken, A. Göçmez, Ü. Yilmazer, F. Pekel, and S. Özkar, "Modeling and Rheology of HTPB Based Composite Solid Propellants," *Polymer Composites*, vol. 19, no. 4, pp. 463-472, 1998, doi: 10.1002/pc.10121.

[7] C. P. R. Nair, C. H. D. V. Prasad, and K. N. Ninan, "Effect of Process Parameters on the Viscosity of AP/Al/HTPB Based Solid Propellant Slurry," *Journal of Energy and Chemical Engineering*, vol. 1, no. 1, pp. 1-9, 2013.

[8] K. K. Kuo and R. Acharya, *Applications of Turbulent and Multiphase Combustion*. 2012.

[9] A. Davenas, *Solid Rocket Propulsion Technology*. Newnes, 2012.

[10] C. L. Horine and E. W. Madison, *Solid Propellant Processing Factors in Rocket Motor Design*. National Aeronautics and Space Administration, 1971.

[11] C. M. Spadaccini, "LLNL-PRES-764604."

[12] A. K. Murray *et al.*, "Selectively-deposited Energetic Materials: A Feasibility Study of the Piezoelectric Inkjet Printing of Nanothermites," *Additive Manufacturing*, vol. 22, pp. 69-74, 2018, doi: 10.1016/j.addma.2018.05.003.

[13] C. Huang, G. Jian, J. B. DeLisio, H. Wang, and M. R. Zachariah, "Electrospray Deposition of Energetic Polymer Nanocomposites with High Mass Particle Loadings: A Prelude to 3D Printing of Rocket Motors," *Advanced Engineering Materials*, vol. 17, no. 1, pp. 95-101, 2015, doi: 10.1002/adem.201400151.

[14] X. Li, P. Guerieri, W. Zhou, C. Huang, and M. R Zachariah, "Direct Deposit Laminate Nanocomposites with Enhanced Propellent Properties", *ACS Applied Materials & Interfaces*, vol. 7, no. 17, pp. 9103-9109, 2015, doi: 10.1021/acsami.5b00891

[15] A. Sidambe, "Biocompatibility of Advanced Manufactured Titanium Implants—A Review", *Materials*, vol. 7, no. 12, pp. 8168-8188, 2014, doi: 10.3390/ma7128168.

[16] X. Tian, J. Jin, S. Yuan, C. Kai Chua, S. Tor, and K. Zhou, "Emerging 3D-Printed Electrochemical Energy Storage Devices: A Critical Review", *Advanced Energy Materials*, vol. 7, no. 17, pp. 1700127, 2017, doi: 10.1002/aenm.201700127.

[17] S. A. Whitmore, S. L. Merkley, L. Tonc, and S. D. Mathias, "Survey of Selected Additively Manufactured Propellants for Arc Ignition of Hybrid Rockets," *Journal of Propulsion and Power*, vol. 32, no. 6, pp. 1494-1504, 2016, doi: 10.2514/1.B36106.

[18] S. Whitmore, Z. Peterson, and S. Eilers, "Analytical and Experimental Comparisons of HTPB and ABS as Hybrid Rocket Fuels," in *47th AIAA/ASME/SAE/ASEE Joint*

Propulsion Conference & Exhibit, Joint Propulsion Conferences: American Institute of Aeronautics and Astronautics, 2011.

[19] S. Hwang, E. I. Reyes, K.-s. Moon, R. C. Rumpf, and N. S. Kim, "Thermo-mechanical Characterization of Metal/Polymer Composite Filaments and Printing Parameter Study for Fused Deposition Modeling in the 3D Printing Process," *Journal of Electronic Materials*, vol. 44, no. 3, pp. 771-777, 2015, doi: 10.1007/s11664-014-3425-6.

[20] C. Bauer *et al.*, "Application of Additive manufacturing in Solid and Hybrid Grain Design," in *52nd AIAA/SAE/ASEE Joint Propulsion Conference*, AIAA Propulsion and Energy Forum: American Institute of Aeronautics and Astronautics, 2016.

[21] D. Armold *et al.*, "Performance Characterization of Hybrid Rocket Fuel Grains with Complex Port Geometries Fabricated Using Rapid Prototyping Technology," *International Journal of Energetic Materials and Chemical Propulsion*, vol. 13, no. 4, pp. 287-307, 2014, doi: 10.1615/IntJEnergeticMaterialsChemProp.2014011169.

[22] T. S. Elliott *et al.*, "Additive Manufacturing of Small Scale Rocket Grain Cartridges with Uniformly Distributed Aluminum Particles," in *52nd AIAA/SAE/ASEE Joint Propulsion Conference*, AIAA Propulsion and Energy Forum: American Institute of Aeronautics and Astronautics, 2016.

[23] J. Fuller, D. Ehrlich, P. Lu, R. Jansen, and J. Hoffman, "Advantages of Rapid Prototyping for Hybrid Rocket Motor Fuel Grain Fabrication," in *47th AIAA/ASME/SAE/ASEE Joint Propulsion Conference & Exhibit*, Joint Propulsion Conferences: American Institute of Aeronautics and Astronautics, 2011.

[24] U. Scheithauer, E. Schwarzer, H.-J. Richter, and T. Moritz, "Thermoplastic 3D Printing—An Additive Manufacturing Method for Producing Dense Ceramics," *International Journal of Applied Ceramic Technology*, vol. 12, no. 1, pp. 26-31, 2015, doi: 10.1111/ijac.12306.

[25] A. Osgood, "Rheological characterization of non-Newtonian Propellants for Casting Optimization," in *5th Propulsion Joint Specialist*, Joint Propulsion Conferences: American Institute of Aeronautics and Astronautics, 1969.

[26] J. A. Lewis, J. E. Smay, J. Stuecker, and J. Cesarano, "Direct Ink Writing of Three-Dimensional Ceramic Structures," *Journal of the American Ceramic Society*, vol. 89, no. 12, pp. 3599-3609, 2006, doi: 10.1111/j.1551-2916.2006.01382.x.

[27] W. Li, A. Ghazanfari, M. C. Leu, and R. G. Landers, "Extrusion-on-demand Methods for High Solids Loading Ceramic Paste in Freeform Extrusion Fabrication," *Virtual and Physical Prototyping*, vol. 12, no. 3, pp. 193-205, 2017, doi: 10.1080/17452759.2017.1312735.

[28] S. Hong, C. Sanchez, H. Du, and N. Kim, "Fabrication of 3D Printed Metal Structures by Use of High-Viscosity Cu Paste and a Screw Extruder," *Journal of Electronic Materials*, vol. 44, no. 3, pp. 836-841, 2015, doi: 10.1007/s11664-014-3601-8.

[29] F. Ruz-Nuglo, L. Groven, and J. A. Puszynski, "Additive Manufacturing for Energetic Components and Materials," in *50th AIAA/ASME/SAE/ASEE Joint Propulsion Conference*, AIAA Propulsion and Energy Forum: American Institute of Aeronautics and Astronautics, 2014.

[30] A. C. R, N. Balasubramanian, V. Natarajan, C. Oommen, R. Bn, and V. R. Sanal Kumar, "Flame Spread Studies on Additive Manufactured Porous Propellant Grains," in *53rd AIAA/SAE/ASEE Joint Propulsion Conference*, AIAA Propulsion and Energy Forum: American Institute of Aeronautics and Astronautics, 2017.

[31] I. Gunduz, M. S. McClain, P. Cattani, G. Chiu, J. F. Rhoads, and S. Son, "3D Printing of Extremely Viscous Materials Using Ultrasonic Vibrations", *Additive Manufacturing*, vol. 22, pp. 98-103, 2018, doi : 10.1016/j.addma.2018.04.029.
[32] J. Brown, S. Thynell, and K. Kuo, "Regression Behavior of Composite-layered Gun Propellants," J. Brown, 1993, p. 9.
[33] T. Liang *et al.*, "Experimental Study on Thermal Expansion Coefficient of Composite Multi-layered Flaky Gun Propellants," *Composites Part B: Engineering*, vol. 166, pp. 428-435, 2019, doi: https://doi.org/10.1016/j.compositesb.2019.02.024.
[34] J. R. Luman *et al.*, "Development and Characterization of High Performance Solid Propellants Containing Nano-sized Energetic Ingredients," *Proceedings of the Combustion Institute*, vol. 31, no. 2, pp. 2089-2096, 2007, doi: 10.1016/j.proci.2006.07.024.
[35] T. G. Manning *et al.*, "Development and Performance of High Energy High Performance Co-Layered ETPE Gun Propellant for Future Large Caliber System," N. Army Armament Research Development And Engineering Center Picatinny Arsenal, 2006.
[36] W. Oberle, "Methodology for Determining Propelling Charge Dimensions for Layered Propellant Charges," M. D. Army Research Lab Aberdeen Proving Ground, 2001.
[37] M. S. McClain, I. E. Gunduz, and S. F. Son, "Additive Manufacturing of Ammonium Perchlorate Composite Propellant with High Solids Loadings," *Proceedings of the Combustion Institute*, vol. 37, no. 3, pp. 3135-3142, 2019, doi: https://doi.org/10.1016/j.proci.2018.05.052.
[38] T. L. Jackson and J. Buckmaster, "Heterogeneous Propellant Combustion," *AIAA Journal*, vol. 40, no. 6, pp. 1122-1130, 2002, doi: 10.2514/2.1761.
[39] L. Massa, T. L. Jackson, and J. Buckmaster, "New Kinetics for a Model of Heterogeneous Propellant Combustion," *Journal of Propulsion and Power*, vol. 21, no. 5, pp. 914-924, 2005, doi: 10.2514/1.2433.
[40] G. Amadio and T. L. Jackson, "A New Packing Code for Creating Mirostructures of Propellants and Explosives," in *51st AIAA/SAE/ASEE Joint Propulsion Conference*, AIAA Propulsion and Energy Forum: American Institute of Aeronautics and Astronautics, 2015.
[41] T. L. Jackson, "Modeling of Heterogeneous Propellant Combustion: A Survey," *AIAA Journal*, vol. 50, no. 5, pp. 993-1006, 2012, doi: 10.2514/1.J051585.
[42] R. Miller, "Effects of Particle Size on Reduced Smoke Propellant Ballistics," in *18th Joint Propulsion Conference*, Joint Propulsion Conferences: American Institute of Aeronautics and Astronautics, 1982.
[43] A. H. Yan, S. F. Son, T. L. Jackson, and P. Venugopal, "Validation of Numerical Simulations for Nano-Aluminum Composite Solid Propellants," *Journal of Propulsion and Power*, vol. 27, no. 6, pp. 1280-1287, 2011, doi: 10.2514/1.B34233.
[44] E. Price, "Effect of Multidimensional Flamelets in Composite Propellant Combustion," *Journal of Propulsion and Power*, vol. 11, no. 4, pp. 717-729, 1995, doi: 10.2514/3.23897.
[45] M. S. McClain, A. Afriat, J. F. Rhoads, I. E. Gunduz, and S. F. Son, "Development and Characterization of a Photopolymeric Binder for Additively Manufactured Composite Solid Propellant Using Vibration Assisted Printing," *Propellants, Explosives, Pyrotechnics*, vol. 45, no. 6, pp. 853-863, 2020, doi: 10.1002/prep.201900387.

[46] R. Pandey, "Photopolymers in 3d Printing Applications," Plastics Technology, Arcada, PhD dissertation, 2014.
[47] C. Decker, "The Use of UV-Irradiation in Polymerization," *Polymer International*, vol. 45, no. 2, pp. 133-141, 1998, doi: 10.1002/(SICI)1097-0126(199802)45:2<133::AID-PI969>3.0.CO;2-F.
[48] E. Andrzejewska, "Chapter 2 - Free Radical Photopolymerization of Multifunctional Monomers," in *Three-Dimensional Microfabrication Using Two-photon Polymerization*, T. Baldacchini. Oxford: William Andrew Publishing, 2016, pp. 62-81.
[49] J. W. Lee, I. H. Lee, and D.-W. Cho, "Development of Micro-stereolithography Technology Using Metal Powder," *Microelectronic Engineering*, vol. 83, no. 4, pp. 1253-1256, 2006, doi: 10.1016/j.mee.2006.01.192.
[50] P. J. Bartolo and J. Gaspar, "Metal Filled Resin for Stereolithography Metal Part," *CIRP Annals - Manufacturing Technology*, vol. 57, no. 1, pp. 235-238, 2008, doi: 10.1016/j.cirp.2008.03.124.
[51] S. Y. Hong *et al.*, "Experimental Investigation of Mechanical Properties of UV-Curable 3D Printing Materials," *Polymer*, vol. 145, pp. 88-94, 2018, doi: 10.1016/j.polymer.2018.04.067.
[52] V. Tomeckova and J. Halloran, "Cure Depth for Photopolymerization of Ceramic Suspensions", *Journal of the European Ceramic Society*, vol. 30, no. 15, pp. 3023-3033, 2010, doi: 10.1016/j.jeurceramsoc.2010.06.004.
[53] K. Landfester, J. Eisenblätter, and R. Rothe, "Preparation of Polymerizable Miniemulsions by Ultrasonication," *JCT Research*, vol. 1, no. 1, pp. 65-68, 2004, doi: 10.1007/s11998-004-0026-y.
[54] A. Afriat, McClain, M. S., McCaw, J. C., I.E. Gunduz, Rhoads, J. F., and S. F. & Son, "Development of a Dual Nozzle Vibration Assisted 3D Printer with Applications to Reactive Materials," Boston, MA: Materials Research Society, December 2019.
[55] M. L. Gross, T. D. Hedman, S. F. Son, T. L. Jackson, and M. W. Beckstead, "Coupling Micro and Meso-scale Combustion Models of AP/HTPB propellants," *Combustion and Flame*, vol. 160, no. 5, pp. 982-992, 2013, doi: https://doi.org/10.1016/j.combustflame.2013.01.016.
[56] K. C. Brown, V. Sankaran, and T. L. Jackson, "Mesoscale Modeling of Solid Propellant Burn Rates," in *AIAA Scitech 2019 Forum*, AIAA SciTech Forum: American Institute of Aeronautics and Astronautics, 2019.
[57] B. T. Bojko, M. Gross, and T. L. Jackson, "Investigating Dimensional Effects on Predicting Burning Rates of Heterogeneous Solid Propellants," in *AIAA Scitech 2019 Forum*, AIAA SciTech Forum: American Institute of Aeronautics and Astronautics, 2019.
[58] M. J. Ward, S. F. Son, and M. Q. Brewster, "Steady Deflagration of HMX With Simple Kinetics: A Gas Phase Chain Reaction Model," *Combustion and Flame*, vol. 114, no. 3, pp. 556-568, 1998, doi: https://doi.org/10.1016/S0010-2180(97)00332-5.
[59] M. McClain *et al.*, "Investigation of Additively Manufactured Layered Composite Solid Propellant," in *AIAA Scitech 2020 Forum*, AIAA SciTech Forum: American Institute of Aeronautics and Astronautics, 2020.
[60] T. D. Hedman, D. A. Reese, K. Y. Cho, L. J. Groven, R. P. Lucht, and S. F. Son, "An Experimental Study of the Effects of Catalysts on an Ammonium Perchlorate Based

Composite Propellant Using 5kHz PLIF," *Combustion and Flame*, vol. 159, no. 4, pp. 1748-1758, 2012, doi: 10.1016/j.combustflame.2011.11.014.
[61] T. R. Sippel, S. F. Son, and L. J. Groven, "Aluminum Agglomeration Reduction in a Composite Propellant Using Tailored Al/PTFE Particles," *Combustion and Flame*, vol. 161, no. 1, pp. 311-321, 2014, doi: 10.1016/j.combustflame.2013.08.009.
[62] A. Ishihara, M. Q. Brewster, T. A. Sheridan, and H. Krier, "The Influence of Radiative Heat Feedback on Burning Rate in Aluminized Propellants," *Combustion and Flame*, vol. 84, no. 1, pp. 141-153, 1991, doi: 10.1016/0010-2180(91)90043-B.
[63] N. Kubota, *Propellants and Explosives: Thermochemical Aspects of Combustion*. John Wiley & Sons, 2015.
[64] R. A. Yetter, G. A. Risha, and S. F. Son, "Metal Particle Combustion and Nanotechnology," *Proceedings of the Combustion Institute*, vol. 32, no. 2, pp. 1819-1838, 2009, doi: 10.1016/j.proci.2008.08.013.
[65] J. Kübler, G. Blugan, H. Jelitto, G. Schneider, and R. Dobedoe, "Structural Micro-Layered Ceramics with Surfaces Under Tension and Compression with Increasing Apparent Fracture Toughness," *Key Engineering Materials - KEY ENG MAT*, vol. 336-338, pp. 2564-2568, 2007, doi: 10.4028/www.scientific.net/KEM.336-338.2564.
[66] M. S. McClain, I. Gunduz, and S. Son, "Additive Manufacturing of Carbon Fiber Reinforced Silicon Carbide Solid Rocket Nozzles" in *AIAA Scitech 2019 Forum*, AIAA SciTech Forum: American Institute of Aeronautics and Astronautics, 2019.
[67] C. Yang, X. Tian, T. Liu, Y. Cao, and D. Li, "3D Printing for Continuous Fiber Reinforced Thermoplastic Composites: Mechanism and Performance," *Rapid Prototyping Journal*, vol. 23, no. 1, pp. 209-215, 2017, doi: 10.1108/RPJ-08-2015-0098.
[68] F. Ning, W. L. Cong, J. Qiu, J. Wei, and S. Wang, "Additive Manufacturing of Carbon Fiber Reinforced Thermoplastic Composites using Fused Deposition Modeling", *Composites Part B: Engineering*, vol. 80, pp. 369-378, 2015, doi: 10.1016/j.compositesb.2015.06.013.
[69] H. L. Tekinalp *et al.*, "Highly Oriented Carbon Fiber-polymer Composites via Additive Manufacturing," *Composites Science and Technology*, vol. 105, pp. 144-150, 2014, doi: 10.1016/j.compscitech.2014.10.009.
[70] Y. Wang, Z. Chen, and S. Yu, "Ablation Behavior and Mechanism Analysis of C/SiC Composites," *Journal of Materials Research and Technology*, vol. 5, no. 2, pp. 170-182, 2016, doi: 10.1016/j.jmrt.2015.10.004.
[71] S. Kumar *et al.*, "Fabrication and Erosion Studies of C–SiC Composite Jet Vanes in Solid Rocket Motor Exhaust," *Journal of the European Ceramic Society*, vol. 31, no. 13, pp. 2425-2431, 2011, doi: 10.1016/j.jeurceramsoc.2011.06.007.
[72] J. Henderson, L. Anderson, and G. Moore, "Comparison of Ablative Materials in a Solid Rocket Motor Flow Field," 1979.
[73] F. Breede, S. Hofmann, N. Jain, and R. Jemmali, "Design, Manufacture, and Characterization of a Carbon Fiber-Reinforced Silicon Carbide Nozzle Extension," *International Journal of Applied Ceramic Technology*, vol. 13, no. 1, pp. 3-16, 2016, doi: 10.1111/ijac.12496.
[74] S. Kumar, A. Kumar, R. B. Mala, and R. R. Mokhasunavisu, "Fabrication and Ablation Studies of 4D C/SiC Composite Nozzle Under Liquid Propulsion," *International Journal of Applied Ceramic Technology*, vol. 12, no. S3, pp. E176-E190, 2015, doi: 10.1111/ijac.12392.

[75] L. Mohan Kumar, K. M. Usha, E. N. Anandapadmanabhan, and P. Chakravarthy, "Effect of Fibre Orientation on the Properties and Functional Performance of Ablative Materials for Solid Rocket Motors," *Transactions of the Indian Institute of Metals,* vol. 70, no. 9, pp. 2407-2413, 2017, doi: 10.1007/s12666-017-1102-1.
[76] S. B. Cox, D. Lui, X. Wang, and J. Gou, "Processing and Characterization of Basalt Fiber Reinforced Ceramic Composites for High Temperature Applications Using Polymer Precursors," PhD dissertation, 2014.
[77] G. Franchin, L. Wahl, and P. Colombo, "Direct Ink Writing of Ceramic Matrix Composite Structures," *Journal of the American Ceramic Society,* vol. 100, no. 10, pp. 4397-4401, 2017, doi: 10.1111/jace.15045.
[78] S. Nambu and M. Enoki, "Strength and Toughness of Graphite Materials for Solid Rocket Motor," *Designing, Processing And Properties Of Advanced Engineering Materials,* vol. 449, pp. 709-712, 2004, doi: 10.4028/www.scientific.net/MSF.449-452.709.
[79] F. C. Campbell, *Structural Composite Materials*. Materials Park, Ohio: Materials Park, Ohio : ASM International, 2010.
[80] M. Černý, P. Glogar, Z. Sucharda, and V. MacHovič, "Properties and Performance of Polysiloxane-derived Ceramic Matrix in Heat Resistant Composites Reinforced with R-glass or Fine Ceramic Fibres," *Ceramics - Silikaty,* vol. 49, no. 3, pp. 145-152, 2005.
[81] S. Jenkins, "Handbook of Advanced Ceramics: Materials, Applications, Processing and Properties," *Chemical Engineering,* vol. 120, no. 3, p. 9, 2013.
[82] W. W. Pultz and W. Hertl, "SiO 2 +SiC Reaction at Elevated Temperatures. Part 1.—Kinetics and Mechanism," *Transactions of the Faraday Society,* vol. 62, no. 0, pp. 2499-2504, 1966, doi: 10.1039/TF9666202499.
[83] T. L. Boggs, "Deflagration Rate, Surface Structure, and Subsurface Profile of Self-Deflagrating Single Crystals of Ammonium Perchlorate," *AIAA Journal,* vol. 8, no. 5, pp. 867-873, 1970, doi: 10.2514/3.5780.
[84] D. N. Collard *et al.*, "Solid Propellant with Embedded Additively Manufactured Reactive Components," in *AIAA Joint Propulsion & Energy 2019 Forum*, AIAA JP&E Forum: American Institute of Aeronautics and Astronautics, 2019
[85] T. J. Fleck, A. Murray, I. Gunduz, S. Son, G. Chiu, and J. Rhoads, "Additive Manufacturing of Multifunctional Reactive Materials", *Additive Manufacturing*, vol. 17, pp. 176-182, 2017, doi: 10.1016/j.addma.2017.08.008.
[86] S. Isert, C. D. Lane, I. E. Gunduz, and S. F. Son, "Tailoring Burning Rates Using Reactive Wires in Composite Solid Rocket Propellants," *Proceedings of the Combustion Institute,* vol. 36, no. 2, pp. 2283-2290, 2017, doi: 10.1016/j.proci.2016.06.141.
[87] S. Verma and P. A. Ramakrishna, "Dependence of Density and Burning Rate of Composite Solid Propellant on Mixer Size," *Acta Astronautica,* vol. 93, pp. 130-137, 2014, doi: 10.1016/j.actaastro.2013.07.016.
[88] S. Isert, T. D. Hedman, R. P. Lucht, and S. F. Son, "Oxidizer Coarse-to-fine Ratio Effect on Microscale Flame Structure in a Bimodal Composite Propellant," *Combustion and Flame,* vol. 163, pp. 406-413, 2016, doi: 10.1016/j.combustflame.2015.10.015.
[89] B. C. Terry, I. E. Gunduz, M. A. Pfeil, T. R. Sippel, and S. F. Son, "A Mechanism for Shattering Microexplosions and Dispersive Boiling Phenomena in Aluminum–lithium Alloy Based Solid Propellant," *Proceedings of the Combustion Institute,* vol. 36, no. 2, pp. 2309-2316, 2017, doi: https://doi.org/10.1016/j.proci.2016.06.099.

[90] H. M. Belal, "Modifying Burning Rate and Agglomeration Size in Aluminized Composite Solid Propellants Using Mechanically Activated Metals," PhD Dissertation, Mechanical Engineering, Purdue University, West Lafayette, IN, USA, 2016. [Online]. Available: https://docs.lib.purdue.edu/open_access_dissertations/975

[91] S. Vummidi Lakshman, J. D. Gibbins, E. R. Wainwright, and T. P. Weihs, "The Effect of Chemical Composition and Milling Conditions on Composite Microstructure and Ignition Thresholds of AlZr Ball Milled Powders," *Powder Technology*, vol. 343, pp. 87-94, 2019, doi: 10.1016/j.powtec.2018.11.012.

VITA

MONIQUE MCCLAIN

LinkedIn: https://www.linkedin.com/pub/monique-mcclain/62/2b8/646

Education

Purdue University
- DOCTOR OF PHILOSOPHY — June 2020
- MASTER OF SCIENCE, AERONAUTICS & ASTRONAUTICS — August 2018

University of California, San Diego
- BACHELOR OF SCIENCE, AEROSPACE ENGINEERING — June 2016

Skills

COMPUTER: MATLAB, CHEMKIN, CAD software (Inventor, SolidWorks, Fusion), LABVIEW, ANSYS Fluent, RPA, COSILAB, C/C++, Linux, LaTeX, Rocfire
EXPERIMENT: Micro-CT, high pressure combustion experiments, solid rocket static fire experiments, flexural strength testing, friction testing, viscosity testing (rotational viscometer and capillary rheometer), DSC/TGA, opposed flow burner
OTHER: Fused filament fabrication (FFF), direct ink write (DiW), and vibration assisted printing (VAP) additive manufacturing methods

Work Experience

GRADUATE RESEARCH ASSISTANT – Purdue University – August 2016 – Present

- Investigate effect of catalysts on the combustion of additively manufactured layered solid propellant
- Compare layered solid propellant models to high pressure experiments of additively manufactured layered propellant
- Analyze effects of photopolymers on ammonium perchlorate composite propellant
- Additively manufacture ablative nozzle materials (carbon fiber reinforced silicon carbide)
- Additively manufacture ammonium perchlorate composite propellant (85% solids loading and 6.9 million cP viscosity)
- Fabricate ammonium perchlorate composite propellant with metal additives and characterize performance
- Measure burning rate and conduct particle capturing experiments of propellants in windowed pressure vessels
- Design and build modifications to commercially available FFF printers to equip them for 3D printing custom viscous materials (VAP)
- Peer reviewed papers for *Combustion Science and Technology*, *Journal of Hazardous Materials, AIAA Journal of Propulsion and Power,* and *Journal of Aerospace Technology and Management*
- Manage VAP resources in the lab and mentor 3 students whose research involves VAP and multi-material printing

GRADUATE RESEARCH INTERN – NAWCWD China Lake – May 2019 – August 2019

- Modeled layered ammonium perchlorate composite propellant with Rocfire code
- Characterize the melt layer of ammonium perchlorate single crystals in-situ at high pressure

CHARACTERIZATION OF SOLID-LIQUID HYBRID ROCKET FUEL GRAIN– Purdue University – August 2018 – December 2018

- Designed solid fuel matrix capable of storing liquid fuel to create a novel solid-liquid hybrid fuel grain
- Tested absorption of liquid fuel into a solid fuel matrix and temperature dependent qualities of constructed grains
- Successfully burned and analyzed the combustion of ~75 wt.% RP-2/25 wt.% HTPB strands in ambient air and in opposed flow burner
- Paper presented at AIAA Propulsion and Energy Forum (2019)

GRADUATE RESEARCH INTERN – NASA Marshall Space Flight Center – June 2018 – August 2018

- Additively manufactured advanced ceramic composite materials for solid rocket nozzle applications
- Designed experiments to test material properties of additively manufactured ceramic composite parts

MULTI-ELEMENT COMBUSTOR WITH SELF-EXCITED INSTABILITIES IN THE TRANSVERSE DIRECTION– Purdue University – January 2018 – May 2018

- Part of team that designed, built, and tested a 7-element combustor that operated with natural gas/air and displayed self-excited combustion instabilities
- Performed simulations in ANSYS Fluent on conditions upstream the combustor and helped with test stand assembly

SUMMER INTERN LEAD, THRUSTER ENGINEER LEAD - Additive Rocket Corporation – April 2015 – August 2016

- Summer Intern Lead: Lead 2 intern teams (~4 students each) to design an additively manufactured tank and valve for satellites. Used CAD software to make designs and ANSYS for structural and fluid simulations. 3D printed models of preliminary designs for testing. Coordinated design reviews between company founders and interns
- Thruster Engineer Lead: Independently designed a 3D printed monopropellant thruster for satellite applications

SMART INTERN – University of Colorado, Boulder – June 2015 – August 2015

- Independently researched the turbulent combustion of hydrogen and air using DNS data and MATLAB analysis. Calculated the distance between two adjacent particles as a function of time and temperature

CAMP INTERN – University of California, San Diego – June 2014 – August 2014

- Independently researched the autoignition temperatures of dimethyl ether and heptane fuel mixtures using CHEMKIN. Compared the CHEMKIN predictions to experimental results

Teaching Experience

GUEST LECTURER – Purdue University – March 2019

- Volunteered to deliver 3 lectures on rocket propulsion in Professor Karen Marais' AAE 251 Aerospace Systems class in two different sections (~130 and ~30 students each).

UNDERGRADUATE RESEARCH ASSISTANT MENTOR – Purdue University – June 2017 – July 2017 and January 2019 – May 2019

- Mentored an undergraduate research assistant in the summer of 2017 as part of a summer research program. Oversaw their project of characterizing the viscosity of propellant and clay with a Brookfield viscometer. Assisted with paper, poster, and presentation revisions. The student (Daniel Inman) became a graduate research assistant at Zucrow in fall of 2018
- Mentored an undergraduate research assistant on developing python scripts to allow customization of GCODE for 3D printing. Assisted with paper, poster, and presentation revisions. The student (Aaron Afriat) became a graduate research assistant in summer of 2019 in my research group. I am currently mentoring him on the development of a dual nozzle 3D printer that can additively manufacture two types of energetic materials (i.e. propellants and reactive filaments)
- Mentoring an undergraduate research assistant tasked with developing a customized 3D printer (VAP) and investigating adhesion between dissimilar materials (i.e. aluminum/polyvinylidene fluoride and composite propellant) that will be 3D printed together

EFFECTIVE COLLEGE TEACHING WORKSHOP – Purdue University – October 2019

- Attended a workshop for 1.5 days hosted by Drs. Richard Felder and Rebecca Brent to learn how to teach classes more effectively

Future Faculty Conferences

NEXTPROF NEXUS – Georgia Tech – October 2019

- Competitively applied and was accepted to this program (~30% acceptance rate). The goal was to prepare graduate students and postdocs from diverse backgrounds to apply for tenure-track positions and to successfully achieve tenure in engineering. Hosted by Georgia Tech, University of California Berkeley, and University of Michigan

RISING STARS IN MECHANICAL ENGINEERING – Stanford University – October 2019

- Competitively applied and was accepted to this program (~50% acceptance rate). The goal was to prepare women graduate students and postdocs to apply for tenure-track positions and to successfully achieve tenure in Mechanical Engineering. Hosted by Stanford University, University of California Berkeley, and MIT

Extracurricular Experience

PRESIDENT, SOCIAL CHAIR – Zucrow Student Association – May 2017 – May 2019

- President: Organized social/professional events and represented the student body of Zucrow (180 students). Helped with ME an AAE department interviews, attended college of engineering meetings, facilitated Zucrow Student Council meetings, and coordinated with human resources and the director of Zucrow Laboratories to improve the work environment
- Social Chair: Promoted communication between research groups at Zucrow by coordinating social events. Created the Zucrow Student Council which allows student representatives from each research group to make suggestions on how to improve the workplace to the director of Zucrow Laboratories

UNDERGRADUATE OUTREACH CHAIR – Black Graduate Student Association – May 2017 – May 2018

- Organized GRAD 101, an event that encourages minority undergraduate students to consider graduate/professional school and prepares them for the application process. Coordinated graduate student and administrative volunteers from different departments. Developed a workshop on writing personal statements

PRESIDENT, SRETARY, PROPULSION DEPUTY, PROPULSION ENGINEER – Triton Rocket Club – September 2012 – June 2016

- President: Led the effort to become the first university team to send a rocket to space. Guided project teams to finish goals in a timely and efficient manner while maintaining the safety of all members. Organized club activities and secured funding from corporate sponsors. Hosted a resume workshop that serviced hundreds of students. Began an outreach program to local high schools to increase interest in STEM. Static fired a P motor and launched a rocket with an O-8000 motor
- Secretary: Wrote detailed reports for funding and organized club recruitment activities
- Propulsion Deputy: Led and organized the mixing of ammonium perchlorate composite propellant. Test fired solid rocket engines
- Propulsion Engineer: Worked in a group to build, test, and launch a K-motor rocket fueled by potassium nitrate. Fiberglassed the rocket body, prepared the propellant, and constructed rocket engines

LABVIEW ENGINEER – University of California, San Diego – March 2016 – June 2016

- Worked in a team for a senior design project to successfully test a kerosene emulsion of 9% water in an LR-101 K motor
- Developed LABVIEW code to control a liquid rocket test stand. Programmed it to successfully fire a kerosene rocket motor and acquire thrust, pressure, temperature, and specific impulse data. Included abort safety feature to stop fuel and LOX feeds and vent the stand in the case of an emergency. Analyzed the data. Contributing author on resulting conference paper (JANNAF December, 2016)

SENSORS ENGINEER – Students for the Exploration and Development of Space – August 2014 – April 2015

- Calibrated and tested an Infrared camera to record the temperature of a rocket engine during a static fire test

Presentations

INVESTIGATION OF ADDITIVELY MANUFACTURED COMPOSITE SOLID PROPELLANT

- AIAA SciTech Forum. January 8, 2020. Oral presentation. Orlando, Fl. (Paper #: AIAA 2019-1427)

SWEATING HYBRID ROCKET FUELS; INCLUSION AND TEMPERATURE ACTIVATED RELEASE OF LIQUID FUELS IN SOLID BINDERS

- AIAA Joint Propulsion & Energy Conference. August 21, 2019. Oral presentation. Indianapolis, IN. (Paper #: AIAA 2019-4190)

ADDITIVE MANUFACTURING OF COMPOSITE SOLID PROPELLANT INTO COMPLEX GEOMETRIES

- 50th International Annual Conference of the Fraunhofer ICT. June 25-28, 2019. Poster presentation. Karlsruhe, Germany. ***1st prize in poster competition***

ADDITIVE MANUFACTURING OF CARBON FIBER REINFORCED SILICON CARBIDE ROCKET NOZZLES

- AIAA SciTech Forum. January 7, 2019. Oral presentation. San Diego, CA. (Paper #: AIAA 2019-0408)

ADDITIVE MANUFACTURING OF AMMONIUM PERHCLORATE COMPOSITE PROPELLANT WITH HIGH SOLIDS LOADINGS

- 37th International Combustion Symposium. August 3, 2018. Oral presentation. Dublin, Ireland
- 45th International Conference on Metallurgical Coatings and Thin Films. April 25, 2018. Oral presentation. San Diego, CA
- Material Research Society. November 27, 2017. Oral presentation. Boston, MA

LAGRANGIAN COHERENT STRUCTURES OF PREMIXED-TURBULENT REACTING FLAMES

- LSAMP Symposium. February 22-24, 2016. Poster presentation
- Rocky Mountain Fluid Mechanics Symposium. August 4, 2015. Poster Presentation
- Leadership Alliance National Symposium 2015. July 24-26, 2015. Oral presentation

ANALYSIS OF DIMETHYL ETHER/HEPTANE MIXTURES

- Twenty-Eighth Annual UC San Diego Undergraduate Research Conference. April 25, 2015. Oral Presentation. Faculty nomination required for participation
- CAMP Statewide Symposium. February 6-7, 2015. Poster Presentation. Honorable Mention
- UCSD Summer Research Conference. August 14, 2014. Oral Presentation

Publications

1) **M.S. McClain**, B. Bojko, S.F. Son, "Modeling of Layered Ammonium Perchlorate Composite Propellant with Different Burning Rates", (In preparation for submission in August 2020)
2) **M.S. McClain**, M.D. Ruesch, R.J. Tancin, C. Dennis, C.S. Goldenstein, S.F. Son, "Characterization and Measurement of the Melt Layer of Ammonium Perchlorate Single Crystals and Pellets at High Pressures", (In preparation for submission in July 2020)
3) **M.S. McClain**, A. Afriat, B. Montano, S. Ray, J.F. Rhoads, I.E. Gunduz, S.F. Son, "Experimentation of Layered Ammonium Perchlorate Composite Propellant Fabricated with Vibration Assisted Printing", (In preparation for submission in July 2020)
4) D.N. Collard, **M.S. McClain**, N.H. Dorcy, N.A. Rahman, T.R. Meyer, S.F. Son, "Dynamic X-ray Imaging of Perforation Development and Volume Consumption in Solid Propellants with Additively Manufactured Reactive Components", (Under review at the *AIAA Journal of Propulsion and Power* in May 2020)
5) **M.S. McClain**, A. Afriat, J.F. Rhoads, I.E. Gunduz, S.F. Son, "Development and Characterization of a Photopolymeric Binder for Additively Manufactured Composite Solid Propellant Using Vibration Assisted

Printing". *Propellants, Explosives, and Pyrotechnics* 45 (2019), pp. 853. https://doi.org/10.1002/prep.201900387

6) **M.S. McClain**, A. Afriat, J.F. Rhoads, I.E. Gunduz, S.F. Son, "Development and Characterization of a Photopolymeric Binder for Additively Manufactured Composite Solid Propellant Using Vibration Assisted Printing". *Propellants, Explosives, and Pyrotechnics* 45 (2019), pp. 846 (inside cover). https://doi.org/10.1002/prep.202080602
7) **M.S. McClain**, I.E. Gunduz, S.F. Son, "Additive Manufacturing of Ammonium Perchlorate Composite Propellant with High Solids Loadings". *Proceedings of the Combustion Institute* 37 (2019), pp. 3135-3142. https://doi.org/10.1016/j.proci.2018.05.052
8) I.E. Gunduz, **M. McClain**, P. Cattani, G. T.-C. Chiu, J.F. Rhoads, S.F. Son, "3D Printing of Extremely Viscous Materials Using Ultrasonic Vibrations". *Additive Manufacturing* 22 (2018), pp. 98-103. https://doi.org/10.1016/j.addma.2018.04.029

Conference Proceedings

1) **M.S. McClain**, M.D. Ruesch, R.J. Tancin, C. Dennis, C.S. Goldenstein, S.F.Son, "Characterization of the Melt Layer of Ammonium Perchlorate Single Crystals", (In preparation for AIAA JP&E in August 2020).
2) **M.S. McClain**, A. Afriat, B.J. Montano, S. Ray, J.F. Rhoads, I.E. Gunduz, S.F. Son, "Investigation of Additively Manufactured Layered Composite Solid Propellant", AIAA SciTech, (2020-1427).
3) **M.S. McClain**, M. Paik, C. Farrell, J.P Youngblood, T.L. Pourpoint, "Sweating Hybrid Rocket Fuels; Inclusion and Temperature Activated Release of Liquid Fuels in Solid Binders", AIAA Propulsion & Energy Forum, (2019-4190).
4) D. N. Collard, **M.S. McClain**, T.J. Fleck, N.A. Rahman, J.F. Rhoads, T.R. Meyer, S.S. Son, "Solid Propellant with Embedded Additively Manufactured Reactive Components", AIAA Joint Propulsion & Energy Forum, (2019-4443).
5) **M.S. McClain**, A. Afriat, J.F. Rhoads, I.E. Gunduz, S.F. Son, "Additive Manufacturing of Composite Solid Propellant into Complex Geometries", 50th International Annual Conference of the Fraunhofer ICT, Conference Proceedings, 2019, Paper #86.
6) D.N. Collard, **M.S. McClain**, T.J. Fleck, N.A. Rahman, J.F. Rhoads, T.R. Meyer, S.F. Son, "Additively Manufactured Solid Propellant and Embedded Reactive Components", 50th International Annual Conference of the Fraunhofer ICT, Conference Proceedings, 2019, Paper #28.
7) **M.S. McClain**, I.E. Gunduz, S.F. Son, "Additive Manufacturing of Carbon Fiber Reinforced Silicon Carbide Solid Rocket Nozzles", AIAA SciTech (2019-0408).
8) D. Acosta, A. Batista, R. Bertino, A. Kasses, M. Knight, M. Koizumi, **M. McClain**, N. Montoya, C. Pfeiffer, J. Tang, S. Harrington, "Static Fire Testing of Emulsified RP-1 Utilizing a Bipropellant LR-101 Rocket Engine". JANNAF PIB /11th MSS/9th LPS/8th SPS Joint Subcommittee Meeting. 5–9 December 2016.

Invited Seminars

1) "How to 3D Print a Solid Rocket Motor and Why You Might Want To", **University of Arizona**, Aerospace & Mechanical Engineering department, February 28, 2019.
2) "Additive Manufacturing of Viscous Materials: Development and Characterization of 3D Printed Energetic and Composite Structures", **Penn State University**, Aerospace Engineering department, November 13, 2019.
3) "Additive Manufacturing of Viscous Materials: Development and Characterization of 3D Printed Energetic and Composite Structures", **Purdue University**, Mechanical Engineering department, January 16, 2020.
4) "Additive Manufacturing of Viscous Materials: Development and Characterization of 3D Printed Energetic and Composite Structures", **Notre Dame University**, Aerospace and Mechanical Engineering department, January 21, 2020.
5) "Additive Manufacturing of Viscous Materials: Development and Characterization of 3D Printed Energetic and Composite Structures", **University of Illinois Urbana Champaign**, Aerospace Engineering department, January 30, 2020.
6) "Additive Manufacturing of Viscous Materials: Development and Characterization of 3D Printed Energetic

and Composite Structures", **University of Colorado Boulder**, Aerospace Engineering department, February 14, 2020.

7) "Additive Manufacturing of Viscous Materials: Development and Characterization of 3D Printed Energetic and Composite Structures", **Georgia Institute of Technology**, Aerospace Engineering department, March 3, 2020.

Awards

NASA Space Technology Research Fellowship	August 2017-August 2020
Purdue Doctoral Fellowship	August 2016-August 2020
GEM Associate Fellow	August 2016-August 2020
NACME Scholar	January 2016-June 2016
Ellen and Roger Revelle Scholarship	September 2012-June 2016